UNIVERSITY OF CALIFORNIA
RIVERSIDE

Interstitial Carbon Assisted Growth of Hexagonal Boron Nitride for Van der Waals Material Based Electronics

A Dissertation submitted in partial satisfaction
of the requirements for the degree of

Doctor of Philosophy

in

Electrical Engineering

by

Hao Tian

December 2019

Dissertation Committee:
Dr. Jianlin Liu, Chairperson
Dr. Roger Lake
Dr. Yongtao Cui

‘

’

The Dissertation of Hao Tian is approved:

_____

_____

_____

Committee Chairperson

University of California, Riverside

ACKNOWLEDGEMENTS

I would like to express my appreciation to my advisor Prof. Jianlin Liu. I am sincerely grateful for the opportunity to study in his group since I was a senior undergraduate student at UCR. I want to thank him for his guidance along the way. I have been constantly inspired by his diligent working ethic and his passion toward scientific research. I also have to thank the members of my PhD committee, Prof. Roger Lake and Prof. Yongtao Cui for their time and their helpful advice and suggestions.

I want to specially thank the past lab alumni Dr. Zhongguang Xu, Dr. Renjing Zheng, Dr. Alireza Khanaki, Dr. William Zuo for your mentorship. I would like to acknowledge current member of the lab Mr. Yanwei He, Mr. Wenhao Shi, Ms. Zhenjun Cui, Prof. Long Xu and Prof. Caixia Xu for their continuous support and help throughout the journey. In addition, I would like to thank Dr. Protik Das for his support of my project on the simulation studies. I am grateful to the university staff for their help: Mr. Jun Wang, Mrs. Kim Underhill, Mr. Jun Dizon, Mr. Bill Bingham. I would like to thank my coworkers at KLA and SK Hynix for supporting me during my internship.

Finally, I especially thank my parents. They have provided me unconditional love and care. They are hardworking parents who have sacrificed their lives to support me and give me the best education possible, and I would not have made any of this without them. Special thanks to my best friend and soul-mate Ms. Li Chen. Li has been a true supporter and cheer leader for me during all my ups and downs in the past years.

Previously Published Material Acknowledgement

1. The results in Chapter 2 were published in:

   A. Khanaki, **H. Tian**, Z. Xu, R. Zheng, Y. He, Z. Cui, J. Yang, and J. Liu, Nanotechnology **29,** 035602 (2017).

2. The results in Chapter 3 were published in:

   H. Tian, A. Khanaki, P. Das, R. Zheng, Z. Cui, Y. He, W. Shi, Z. Xu, R. Lake, and J. Liu, Nano letters **18,** 3352 (2018).

3. The results in Chapter 4 were published in:

   H. Tian, Y. He, P. Das, Z. Cui, W. Shi, A. Khanaki, R. K. Lake, and J. Liu, Advanced Materials Interfaces**,** 1901198 (2019).

4. The results in Chapter 5 were published in:

   Y. He, **H. Tian**, A. Khanaki, W. Shi, J. Tran, Z. Cui, P. Wei, and J. Liu, Applied Surface Science**,** 143851 (2019).

I dedicate this thesis to

my parents

for their constant support and unconditional love.

I love you all dearly.

ABSTRACT OF THE DISSERTATION

Carbon Interstitial Assisted Growth of Hexagonal Boron Nitride
for Van der Waals Materials Based Electronics
by

Hao Tian

Doctor of Philosophy, Graduate Program in Electrical Engineering
University of California, Riverside, December 2019
Dr. Jianlin Liu, Chairperson

Two dimensional (2D) hexagonal boron nitride (h-BN) continues to attract tremendous research interest across the globe thanks to their unique optical, electronic, and mechanical properties. However, the controllable synthesis of large size single crystal h-BN is still challenging to realize the technological potential. In this thesis, we focus on growth and characterization of h-BN by molecular beam epitaxy (MBE). By exploring the role of interstitial carbon in transition metal substrate, we have achieved a big step forward toward controllable synthesis of large-size single crystal h-BN.

In the first project, i.e., Chapter 2, we carried out a systematic study of hexagonal boron nitride/graphene (h-BN/G) heterostructure growth by introducing high incorporation of carbon (C) source on a heated cobalt (Co) foil substrate followed by boron and nitrogen sources in a molecular beam epitaxy system. With the increase of C incorporation in Co, three distinct regions of h-BN/G heterostructures were observed from region (1) where the C saturation is not attained at the growth temperature (900 °C) and G is grown only by precipitation during cooling process to form a “G network” underneath the h-BN film; to

region (2) where the Co substrate is just saturated by C atoms at the growth temperature and a part of G growth occurs isothermally to form G islands and another part by precipitation, resulting in a non-uniform h-BN/G film; and to region (3) where a continuous layered G structure is formed at the growth temperature and precipitated C atoms add additional G layers to the system, leading to a uniform h-BN/G film. We realized that the top h-BN film has the largest effect on the growth of underneath G layers in region 1. It is also found that in all three h-BN/G heterostructure growth regions, a 3-hrs h-BN growth at 900 ºC leads to h-BN film with a thickness of 1~2 nm, regardless of the underneath G layers' thickness or morphology. Growth time and growth temperature effects have been also studied.

In the second project, i.e., Chapter 3, we demonstrate that the dissolution of carbon into cobalt (Co) and nickel (Ni) substrates can facilitate the growth of h-BN and attain large-area 2D homogeneity. The morphology of the h-BN film can be controlled from 2D layer-plus-3D islands to homogeneous 2D few-layers by tuning the carbon interstitial concentration in the Co substrate through a carburization process prior to the h-BN growth step. Comprehensive characterizations were performed to evaluate structural, electrical, optical, and dielectric properties of these samples. Single-crystal h-BN flakes with an edge length of ~600 μm were demonstrated on carburized Ni. An average breakdown electric field of 9 MV/cm was achieved for an as-grown continuous 3-layer h-BN on carburized Co. Density functional theory calculations reveal that the interstitial carbon atoms can increase the adsorption energy of B and N atoms on the Co(111) surface and decrease the diffusion activation energy and, in turn, promote the nucleation and growth of 2D h-BN.

In the third project, i.e., Chapter 4, we designed a synthetic approach, in which secondary recrystallized Ni (100) substrates underwent a carburization process, followed by the growth of h-BN in a molecular beam epitaxy system. The h-BN growth dynamics were studied by tuning different growth parameters including the substrate temperature, and the boron and nitrogen source flux ratio. With assistance from density functional theory calculations, we rationalized the role of interstitial C atoms in promoting h-BN growth by enhancing the catalytic effect of the transition metal, which lowers the nucleation activation energy barrier. Through the control of the growth parameters, a single-crystal h-BN monolayer domain as large as 1.4 mm in edge length was achieved. In addition, a high-quality, continuous, large-area h-BN single-layer film with a breakdown electric field of 9.75 MV/cm was demonstrated. The high value of the breakdown electric field suggests that single-layer h-BN has extraordinary dielectric strength for high-performance 2D electronics applications.

In the fourth project, i.e., Chapter 5, we present a study of h-BN adlayer growth and provide a strategy towards eliminating these adlayers for the precise control of the number of 2D layers. By varying the growth parameters such as substrate property, nitrogen source composition, and substrate carburization time, we found that the adlayer growth can be controlled by controlling the nucleation and intercalation processes, which is achieved by engineering the defects and impurities on substrate and the activeness of the h-BN edges. While crystallographic defects and impurities stimulate the multilayer nucleation process, activated edge tends to turn off the intercalation process by reducing the probability of

precursors penetrating into the interface. We have achieved the growth of a large-area adlayer-free single-layer h-BN film.

Table of Contents

List of Figures

List of Tables:

Chapter 1 Introduction

1.1. Van der Waals materials

Two dimensional (2D) van der Walls (vdW) materials are materials consisting of a single or few layers of atoms, bonded by strong chemical bonds in in-plane direction and weakly by van der Walls force in out-of-plane direction. Their layered structure makes electrons in these materials free to move in the 2D plane, but restricted in the out-of-plane direction governed by quantum mechanics. The name of 2D materials came about with the exciting discover of graphene, which is a single-layer of carbon (C) atoms. This material conducts electricity better than copper, and heat better than anything else. [1] The list of amazing properties of this material can go on and on. Although this Nobel Prize winning discovery has made a huge promise for the potential of replacing Si, people soon realized the weakness of graphene—zero bandgap. It is the bandgap that makes traditional semiconductor material like Si semiconducting, allowing a transistor to switch on and off, which serves as the foundation of modern integrated circuits. To offer alternative solutions to compensate for graphene's weaknesses, researchers start to pivot their efforts on other 2D materials beyond graphene.[2] Dozens of 2D materials emerged soon after, such as Transition Metals Dichalcogenides (TMDs) and Hexagonal Boron Nitride (h-BN). It was soon realized that 2D materials are much more than a replacement for Si. For thousands of papers published in last 15 years, the research interest of 2D materials has expended from originally mainly as a solutions for future electronics and optoelectronic to much wider range of application with potential to enhance and prolong human life [3-6]

1.2. **Graphene and hexagonal boron nitride**

Graphene, the first discovered two-dimensional (2D) material consisting of one layer sp^2 hybridized carbon atoms, has attracted great amount of attention since its first demonstration through micromechanical exfoliation in 2004 [7]. Graphene has variety of exciting properties, such as remarkably high electron carrier mobility at room temperature [8], superior thermal [9] and mechanical properties [10].

Hexagonal boron nitride (h-BN), a structure analogue of graphene, is composed of alternating B and N atoms in a honeycomb lattice, with a lattice constant of 0.25nm and a bandgap of ~6 eV. As a dielectric, h-BN has very similar properties (ε~3-4 and breakdown electric field ~0.7 V/nm) to that of SiO_2 [11]. Thanks to the wide bandgap and close lattice matching with graphene, h-BN is extensively used as a building block for constructing 2D vdW heterostructures[12, 13]. Regarding its optical properties, the observation of UV lasing characteristics in an h-BN single crystal [14] brought about significant research attention on this material as a possible candidate for light-emitting devices. Since then, several photo- and cathode- luminescence studies [15] have been published in an effort to understand the electronic and optical properties of h-BN.

1.3. **Molecular beam epitaxy (MBE)**

With all the fascinating properties of 2D materials, it is crucial to develop a controllable and scalable synthetic process before the realization of any technological potentials. Traditionally, graphene and h-BN have been synthesized by chemical vapor deposition (CVD).[16-22] Although great progress has been made, the CVD process is still not optimal. Alternatively, MBE is promising for 2D material growth for its ability to

precisely control solid, gas, and plasma sources and the growth parameters, instant introduction, ease of doping and in-situ characterization capability, thanks to its ultra-high vacuum(UHV) environment.

In the Quantum Structures Laboratory (QSL), a Perkin Elmer 425B MBE system is equipped with a B_2O_3 Knudsen effusion cell as a Boron source, a ECR/ RF N_2 plasma source and a NH_3 gas source as N source, a C_2H_2 gas source with a gas cracker as the C source, a H_2 gas source for annealing purpose. Figure 1.1 shows a picture of the system. A graphite heater is used as the substrate heater with maximum substrate temperature of ~1000 ° C. The UHV condition is maintained by an ion sublimation pump and a turbomolecular pump backed by a mechanical scroll pump. The growth details will be introduced in experimental details section in each chapter.

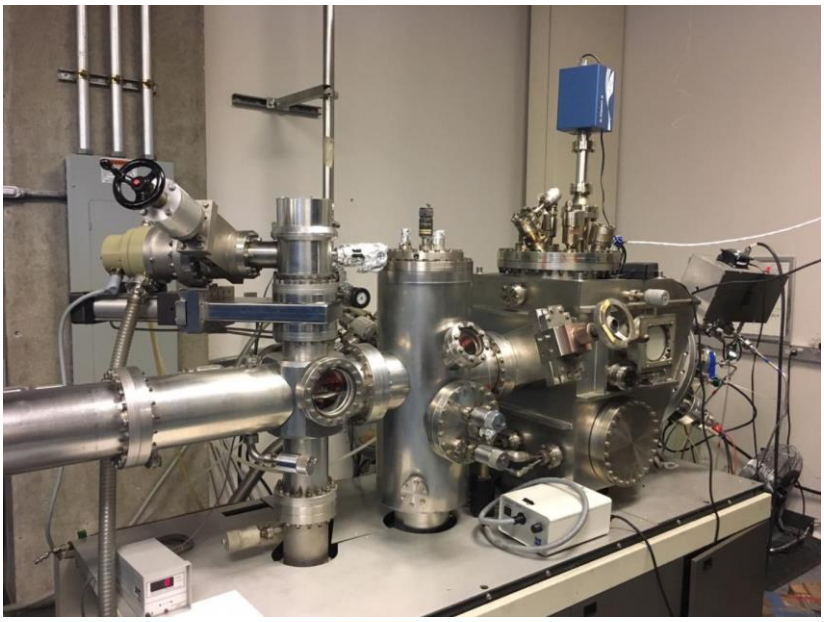

Figure 1.1 A modified Perkin Elmer 425B MBE system in Quantum Structures Laboratory (QSL) at University of California, Riverside (UCR).

1.4. **Organization**

The rest of the dissertation is organized as follows. First, Chapter 2 discusses the epitaxial growth of hexagonal boron nitride/graphene heterostructures (h-BN/G) with high incorporation of C atoms in Co substrate. We show that the structure and quality of h-BN/G heterostructure can be directly altered by the amount of dissolved C atoms in C, which is categorized as 4 growth regions. The effect that individual G or h-BN layers have on the growth, morphology of each other is unfold.

By going to the extreme case with very small amount of carbon introduced into the transition metal substrate, we further realized growth of h-BN layers enhanced by interstitial C atoms. In Chapter 3 we discuss that the tuning of interstitial C concentration in transition metal substrates can bring a new dimension of control of the growth and morphology/thickness control of 2D h-BN in addition to other regular growth parameters. Also, for better understanding of our new growth mechanism, we provide DFT calculations on changes in adsorption energies of B and N atoms when the Co (111) substrate is carburized.

With continuous effort to explore the interstitial C assisted approach, we further designed a synthetic approach, in which secondary recrystallized Ni (100) substrates underwent a carburization process. The h-BN growth dynamics were studied by tuning different growth parameters including the substrate temperature, and the boron and nitrogen source flux ratio. With assistance from density functional theory calculations, we rationalized the role of interstitial C atoms in promoting h-BN growth by enhancing the catalytic effect of the transition metal, which lowers the nucleation activation energy

barrier. Through the control of the growth parameters, a single-crystal h-BN monolayer domain as large as 1.4 mm in edge length was achieved. In addition, a high-quality, continuous, large-area h-BN single-layer film with a breakdown electric field of 9.75 MV/cm was demonstrated. The high value of the breakdown electric field suggests that single-layer h-BN has extraordinary dielectric strength for high-performance 2D electronics applications. These results are presented in Chapter 4.

The adlayer formation has always been a fascinating phenomenon that haunting us. In Chapter 5, we further study mechanism attributing for the adlayer formation and provide a strategy towards eliminating these adlayers for the precise control of the number of 2D layers. We further present the result of the growth of a large-area adlayer-free single-layer h-BN film.

1.5. **References**

[1]Geim, A. K., Graphene: status and prospects. *Science* 2009, 324, 1530-1534.

[2]Geim, A. K.; Grigorieva, I. V., Van der Waals heterostructures. *Nature* 2013, 499, 419-425.

[3]Lee, H.; Choi, T. K.; Lee, Y. B.; Cho, H. R.; Ghaffari, R.; Wang, L.; Choi, H. J.; Chung, T. D.; Lu, N.; Hyeon, T., A graphene-based electrochemical device with thermoresponsive microneedles for diabetes monitoring and therapy. *Nat. Nanotech.* 2016, 11, 566.

[4]Mannoor, M. S.; Tao, H.; Clayton, J. D.; Sengupta, A.; Kaplan, D. L.; Naik, R. R.; Verma, N.; Omenetto, F. G.; McAlpine, M. C., Graphene-based wireless bacteria detection on tooth enamel. *Nat. Commun.* 2012, 3, 763.

[5]Yao, S.; Swetha, P.; Zhu, Y., Nanomaterial-Enabled wearable sensors for healthcare. *Advanced healthcare materials* 2018, 7.

[6]Barua, S.; Dutta, H. S.; Gogoi, S.; Devi, R.; Khan, R., Nanostructured MoS2-based advanced biosensors: a review. *ACS Applied Nano Materials* 2017, 1, 2-25.

[7]Novoselov, K. S.; Geim, A. K.; Morozov, S. V.; Jiang, D.; Zhang, Y.; Dubonos, S. V.; Grigorieva, I. V.; Firsov, A. A., Electric field effect in atomically thin carbon films. *Science* 2004, 306, 666-669.

[8]Bolotin, K. I.; Sikes, K. J.; Jiang, Z.; Klima, M.; Fudenberg, G.; Hone, J.; Kim, P.; Stormer, H., Ultrahigh electron mobility in suspended graphene. *Solid State Commun.* 2008, 146, 351-355.

[9]Balandin, A. A.; Ghosh, S.; Bao, W.; Calizo, I.; Teweldebrhan, D.; Miao, F.; Lau, C. N., Superior thermal conductivity of single-layer graphene. *Nano Lett.* 2008, 8, 902-907.

[10]Lee, C.; Wei, X.; Kysar, J. W.; Hone, J., Measurement of the elastic properties and intrinsic strength of monolayer graphene. *Science* 2008, 321, 385-388.

[11]Haubner, R.; Wilhelm, M.; Weissenbacher, R.; Lux, B., Boron nitrides—properties, synthesis and applications. In *High Performance Non-Oxide Ceramics II*, Springer: 2002; pp 1-45.

[12]Dean, C. R.; Young, A. F.; Meric, I.; Lee, C.; Wang, L.; Sorgenfrei, S.; Watanabe, K.; Taniguchi, T.; Kim, P.; Shepard, K. L., Boron nitride substrates for high-quality graphene electronics. *Nat. Nanotech.* 2010, 5, 722.

[13]Liu, Y.; Huang, Y.; Duan, X., Van der Waals integration before and beyond two-dimensional materials. *Nature* 2019, 567, 323.

[14]Watanabe, K.; Taniguchi, T.; Kanda, H., Direct-bandgap properties and evidence for ultraviolet lasing of hexagonal boron nitride single crystal. *Nat. Mater.* 2004, 3, 404.

[15]Caretti, I.; Jiménez, I., Point defects in hexagonal BN, BC3 and BCxN compounds studied by x-ray absorption near-edge structure. *J. Appl. Phys.* 2011, 110, 023511.

[16]Kim, K. K.; Hsu, A.; Jia, X.; Kim, S. M.; Shi, Y.; Hofmann, M.; Nezich, D.; Rodriguez-Nieva, J. F.; Dresselhaus, M.; Palacios, T., Synthesis of monolayer hexagonal boron nitride on Cu foil using chemical vapor deposition. *Nano letters* 2011, 12, 161-166.

[17]Shi, Y.; Hamsen, C.; Jia, X.; Kim, K. K.; Reina, A.; Hofmann, M.; Hsu, A. L.; Zhang, K.; Li, H.; Juang, Z.-Y., Synthesis of few-layer hexagonal boron nitride thin film by chemical vapor deposition. *Nano Lett.* 2010, 10, 4134-4139.

[18]Song, L.; Ci, L.; Lu, H.; Sorokin, P. B.; Jin, C.; Ni, J.; Kvashnin, A. G.; Kvashnin, D. G.; Lou, J.; Yakobson, B. I., Large scale growth and characterization of atomic hexagonal boron nitride layers. *Nano Lett.* 2010, 10, 3209-3215.

[19]Caneva, S.; Weatherup, R. S.; Bayer, B. C.; Blume, R.; Cabrero-Vilatela, A.; Braeuninger-Weimer, P.; Martin, M.-B.; Wang, R.; Baehtz, C.; Schloegl, R., Controlling

catalyst bulk reservoir effects for monolayer hexagonal boron nitride CVD. *Nano Lett.* 2016, 16, 1250-1261.

[20]Ismach, A.; Mende, P.; Dolocan, A.; Addou, R.; Aloni, S.; Wallace, R.; Feenstra, R.; Ruoff, R.; Colombo, L., Carbon-Assisted Chemical Vapor Deposition of Hexagonal Boron Nitride. *2D Mater.* 2017.

[21]Petrović, M.; Horn-von Hoegen, M.; zu Heringdorf, F.-J. M., Lateral heterostructures of hexagonal boron nitride and graphene: BCN alloy formation and microstructuring mechanism. *Applied Surface Science* 2018, 455, 1086-1094.

[22]Song, Y.; Zhang, C.; Li, B.; Jiang, D.; Ding, G.; Wang, H.; Xie, X., Triggering the atomic layers control of hexagonal boron nitride films. *Applied Surface Science* 2014, 313, 647-653.

Chapter 2 Effect of high carbon incorporation in Co substrates on the epitaxy of hexagonal boron nitride/graphene heterostructures

2.1. Introduction

As a two-dimensional (2D) material, hexagonal boron nitride (h-BN) possesses excellent properties including high band gap energy (~5.9 eV), extremely flat surface (root mean square (RMS) roughness < 0.2 nm) and free of dangling bond or surface charge trap, excellent dielectric properties ($\varepsilon \approx 3–4$ and $V_{breakdown} \approx$ 12 MV/cm) and high chemical resistivity [1-5]. In addition, its complementary electronic properties and similar hexagonal lattice structure to graphene (G) and other 2D systems such as transition metal dichalcogenides (TMDs) have made h-BN an ideal candidate for all electronic devices where nanoscale supporting, insulating, capping, or gating layers are needed [6-8]. In particular, h-BN/G stacked layers have recently attracted much attention since such heterostructure system can be used not only to study fundamental physics of G, e.g., Hofstadter butterfly effect, but also to develop next-generation nanoelectronic devices with superior performances, e.g. tunneling devices [9-15].

So far, h-BN/G heterostructures have been mostly prepared by assembling G and h-BN layers exfoliated from highly ordered pyrolytic graphite (HOPG) and h-BN bulk crystals, respectively [16,17]. Although these high-quality structures made by mechanical exfoliation are the best to showcase the material characteristic and/or device performance, all epitaxial vertical heterostructures with controllable thickness, size and well-defined orientation are indispensable toward practical applications. On this matter, both chemical vapor deposition (CVD) and molecular beam epitaxy (MBE) have been used widely for

the growth of h-BN/G heterostructures on different substrates, especially, transition metals such as Cu [18-28]. For example, Liu et al demonstrated the CVD growth of h-BN/G stacks on Cu foil via a two-step process [18]. Gao et al also reported the CVD growth of vertically stacked h-BN/G heterostructures on Cu foil using temperature-triggered (>900 ºC) chemical switching approach [19].

Among all transition metal substrates, Co benefits from having a high melting point temperature (1495 ºC in 1 atm) which minimizes the amount of substrate evaporation during annealing step and high-temperature growth process. This is very crucial when a thin transition metal (foil or thin film) is aimed to use as a substrate, in particular, when a long growth duration is required for the 2D material growth, as this is often the case for h-BN and h-BN/G heterostructures. Also, metal substrates with a higher carbon (C) solubility such as Co (~1.5% at 900 ºC) allow one to work with a wider range of C concentration and within a wider range of growth temperatures. For instance, in our group, we grew h-BN/G heterostructures with few-layer h-BN flakes and single-layer G with less than 1° miss-match angle [27] as well as continuous large-area few-layer h-BN and thick graphitic structure [28] based on Co substrates with different substrate surface conditions, growth temperature, growth time, and other growth parameters.

Because many parameters such as source, substrate, growth pressure, growth temperature and substrate cooling rate play roles in the growth of these h-BN/G heterostructures, two major growth mechanisms, namely, precipitation growth and direct layer-by-layer epitaxy, have been observed. Nevertheless, to date, it is still challenging to precisely and reliably control the thickness, morphology and quality of h-BN and G layers,

and their alignment across the wafer scale due to the complicated growth processes. In addition, the effect of G and h-BN layers on each other's growth mode, morphology, thickness and quality in h-BN/G heterostructures have not been well understood. Therefore, to further elucidate the growth conditions for precise control of different types of h-BN/G heterostructures, in this paper, we systematically study the effect of high C incorporations in Co on the growth mode/morphology of the epitaxial h-BN/G heterostructures. Three different growth regions of h-BN/G heterostructures are identified based on the concentration of dissolved C atoms in Co and G growth mode. The unique features of Co substrate in conjunction with designing careful experiments and extensive characterizations enabled us to study the effect of top h-BN film on bottom G layers (and vice versa) in h-BN/G heterostructures.

2.2. **Experimental details**

Commercial Co foil (Alfa Aesar, 0.1 mm thick, 99.95% purity) was used as the substrate. As-received Co foils were polished by an SBT 920 Lapping and Polishing workstation. Then, Co foils were cut into 1 cm×1 cm pieces, degreased with acetone and IPA, etched by diluted HCl solution (10%) for 2 minutes to remove the native oxides, and rinsed with deionized water. After blown-dry using a nitrogen gun, the fresh substrates were immediately loaded onto substrate holders and transferred to the growth chamber.

A plasma-assisted MBE (Perkin-Elmer) system was used for the sample growth. A Knudsen effusion cell filled with B_2O_3 powder (Alfa Aesar, 99.999% purity) was used as boron (B) source. Nitrogen plasma (Airgas, 99.9999% purity) generated by an electron cyclotron resonance (ECR) system and high-purity ammonia (American Gas Group, 99.9995% purity) were used as nitrogen (N) sources. Acetylene gas (C_2H_2, Airgas, 99.999% purity) was used as C source. The substrates were heated to 800~950 ºC and annealed at the growth temperature under a 10-sccm (standard cubic centimeters per minute) flow of hydrogen gas for 15 minutes. Then, at the same substrate temperature, 3-sccm acetylene gas was introduced into the chamber for a duration of 5 seconds~3 minutes for different samples, and immediately after that, h-BN growth was started. During the growth, B cell

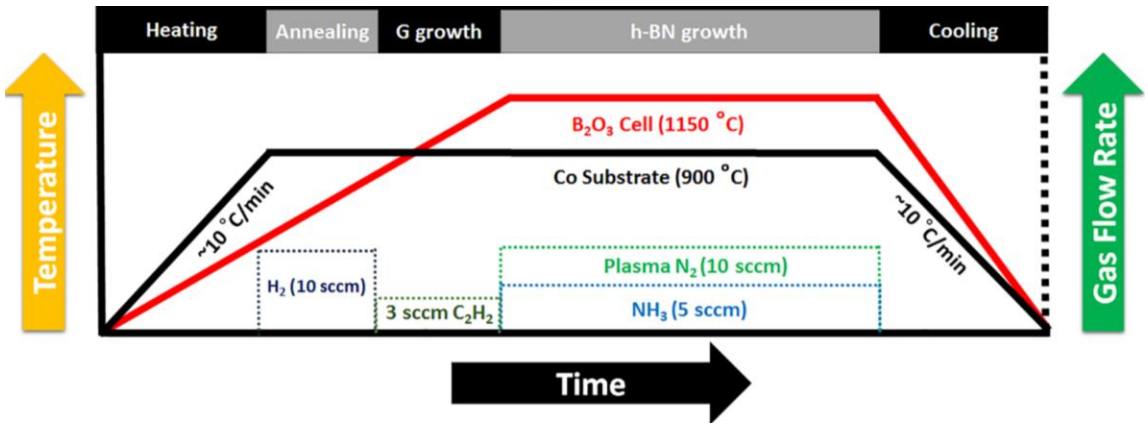

Figure 2.1 Typical growth conditions of h-BN/G heterostructure samples in regions 1-3. To carry out the growth of h-BN/G heterostructure samples, Co substrate was first heated up to 850~950 ºC and annealed for 15 minutes with 10 sccm H_2 gas. Then, the substrate was treated with C (3-sccm C_2H_2 gas) for a duration of 5 sec~3 min for different samples, and immediately after that, h-BN growth was started. During the h-BN growth, B cell temperature was maintained at 1150 ºC. A mixture of N sources consisting of N_2 gas flowed at 10 sccm through an ECR plasma generator and NH_3 gas leaked at a flow rate of 5 sccm through a needle valve was introduced into the chamber. The h-BN growth lasted from 15 min to 3 hrs for different samples. The substrate heating/cooling rate was ~10 ºC/min for all samples.

temperature was maintained at 1150 ºC; a mixture of nitrogen source consisting of N_2 gas flowed at 10 sccm through an ECR plasma generator and NH_3 gas leaked at a flow rate of 5 sccm through a needle valve was introduced into the chamber. The ECR current was set at 60 mA. The growth lasted from 15 minutes to 3 hours for different samples. The substrate heating/cooling rate was ~10 ºC/min for all samples. A schematic of the typical growth process is provided in Figure 2.1.

Raman characterizations were performed using a HORIBA LabRam system equipped with a 60-mW, 532-nm green laser. Scanning electron microscopy (SEM) images were acquired using an FEI NNS450 SEM system in secondary electron mode. X-ray photoelectron spectroscopy (XPS) characterization was conducted using a Kratos AXIS ULTRA XPS system equipped with an Al Kα monochromatic X-ray source and a 165-mm mean radius electron energy hemispherical analyzer. The depth-profile XPS characterization was performed on a 3×3 mm^2 area of the sample using a 2-keV Ar ion beam sputter with an etching rate of 1 nm per minute. Atomic force microscopy (AFM) images were obtained using a Veeco D5000 AFM system in tapping mode. TEM images and selected area electron diffraction (SAED) patterns were acquired using a FEI Tecnai12 system. TEM sample was prepared by picking a transferred h-BN/G film using a 200 mesh Cu grid covered with Quantifoil carbon film with Orthogonal Array of 1.2 μm diameter holes.

For AFM and TEM measurements, samples were transferred using a typical wet transferring method. The as-grown samples were spin-coated first with PMMA (495 A4). Then, we put the samples directly into $FeCl_3$/HCl solution to etch the Co foil substrate for

approximately a day. Thereafter, the stacked PMMA/h-BN/G was transferred into 10% HCl and DI water to rinse out the residual etchant. Then, the floating PMMA/h-BN/G was taken out by desired substrates (SiO_2/Si or sapphire) and left to dry in air for at least 12 hours. Then, a few drops of PMMA were deposited again on the transferred film and soaked for another two hours. These additional drops of PMMA soften the previous PMMA layer and enhance the attachment of h-BN/G on the substrate. PMMA was removed by dipping the sample into acetone bath. Finally, the sample was dried at 40 °C on a hot plate for a couple of hours.

Co(contact)/h-BN/G/Co(foil) two-terminal devices were fabricated by a standard photolithography and lift-off process. A Co layer of 50 nm was patterned as top square contacts with an edge length of 25 μm on the surface of as-grown h-BN/G film. Current-voltage (I-V) characteristics were obtained by an Agilent 4155C semiconductor parameter analyzer equipped with probing tips having a diameter of 5μm (Signatone, SE-TL).

2.3. **Results and discussion**

Figure 2.2 summarizes the growth of h-BN/G heterostructure system on Co foil substrate when the C treatment time changes and h-BN growth conditions are the same (3 hours at 900 °C). Note that C starts to dissolve in Co at around 600 °C and the solubility increases up to ~1.5% at 900 °C [29], i.e. a designated growth temperature in the schematic (Figure 2.2(a)). The temperature-dependent growth of h-BN/G heterostructures indicated that the substrate temperature is an important growth parameter to influence the morphology and coverage of h-BN. With the same other growth conditions, a growth temperature window, which covers 900 °C, was identified for the formation of continuous high-quality h-BN films in the heterostructures as shown in Figure 2.3. Thermodynamically, G growth on Co can start at temperatures above ~700 °C [30, 31].

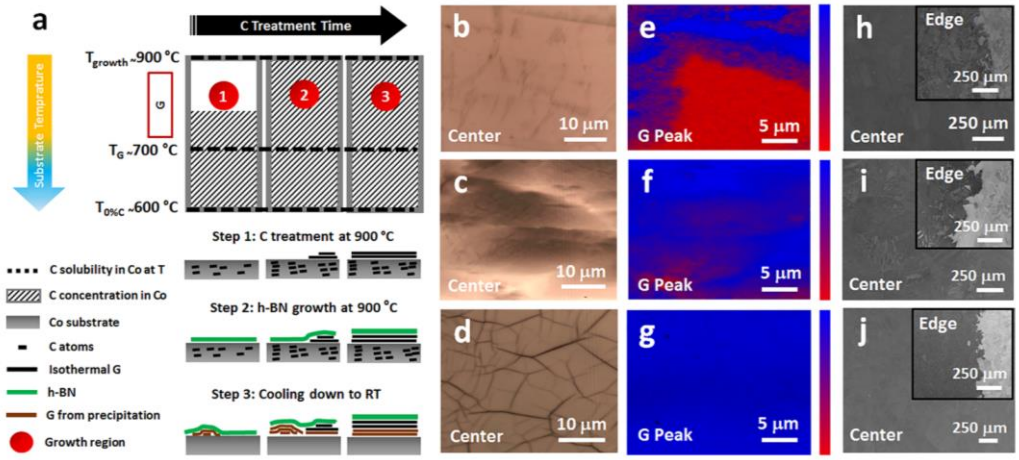

Figure 2.2 H-BN\G heterostructure growth regions on Co substrate. (a) Schematic of h-BN/G growth steps on Co substrate with different C treatment time and same h-BN growth conditions (3 hrs at 900 °C). Three growth regions are identified based on the C treatment time and G growth mode/morphology in h-BN/G samples. (b-d) OM images, (e-g) graphene G-peak intensity mapping, and (h-j) SEM images of the samples with 30-sec, 1.5-min, and 3-min C treatment time, which are representative samples in regions 1, 2, and 3 respectively.

The black hatching areas in Figure 2.2(a) show the C concentration in Co substrate at different growth regions (i.e., 1, 2, and 3), and the black dashed lines display the C solubility levels in Co substrate at designated temperatures (i.e., $T_{0\%C}$, T_G and T_{growth}). The growth regions in Figure 2.2(a) are identified based on the C treatment time, and subsequently, G growth mode/morphology in the h-BN/G samples. Samples with 30-sec, 1.5-min, and 3-min C treatment time are selected as representative samples for regions 1, 2, and 3, respectively, and their optical microscopy (OM), graphene G-peak Raman intensity mapping, and SEM images are shown in Figure 2.2(b-j).

Region 1 is where C solubility or saturation of Co is not reached at the growth temperature of 900 °C, hence, G is formed only by precipitation during substrate cooling

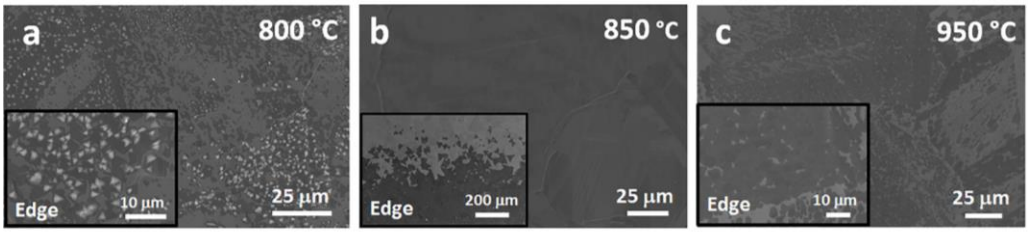

Figure 2.3 H-BN/G temperature-dependent growth with the same 30-sec C treatment time. SEM images of as-grown h-BN/G samples from center and edge areas at (a) 800 °C, (b) 850 °C, and (c) 950 °C. Therefore, together with the 900 °C sample discussed in the main text (Figures 2.2 and 2.7), we have four samples to study the growth temperature dependence. As it appears in the Figure 2.3 and Figures 2.2 and 2.7, the proper substrate temperature to grow a continuous h-BN/G film is 850~900 °C. Below this temperature, for example 800 °C, the h-BN/G film is not continuous and consists of many thick h-BN ad-layers (bright features, as shown in Figure 2.3(a)). The diffusion length of B and N atoms is relatively low (i.e., high activation/barrier energy) due to the lack of thermal energy and, therefore, B and N atoms tend to bond locally and grow more vertically rather laterally [13-15]. On the other hand, as the growth temperature exceeds 900 °C, for example, 950 °C, high desorption rate of B and N atoms from Co substrate surface can become the dominant phenomenon and fails the growth of continuous h-BN/G film [16,17]. Thus, the growth temperature of 850~900 °C with 30-sec C treatment time seems to be the conditions to grow continuous and uniform h-BN/G films.

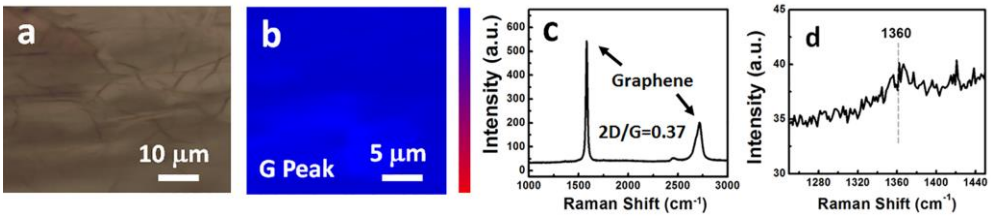

Figure 2.4 G reference sample in region 2. To obtain this sample, the Co substrate was heated up to 900 °C and treated by 1.5-min C (3 sccm), and then the substrate was cooled to room temperature. (a) OM image, (b) graphene G-peak Raman intensity mapping, (c) typical Raman spectrum of the G reference sample in region 2 with a 2D/G ratio of ~0.37 and (d) a shorter-range Raman spectrum between 1250-1450 cm^{-1} showing a negligible graphene D-peak in the reference sample.

process, leading to a "G network" underneath the h-BN film. The dark regions in the OM image of Figure 2.2(b) for a 30-sec C sample and corresponding Raman intensity mapping of graphene G-peak in Figure 2.2(e) display the nature of the G network. Because of this specific morphology, G does not cover a big portion of the Co substrate surface in region 1 samples. This is related to the local accumulation of precipitated C atoms around edge areas of the h-BN flakes (grain boundaries) which is discussed in detail later. This morphology was observed when the C treatment time changed between 5 to 45 seconds.

Region 2 is where the Co substrate is just saturated by C atoms at the growth temperature and, therefore, a part of G growth now occurs isothermally via C saturation-precipitation mechanism [32-34]. Similar to region 1, another part of G growth in this region occurs later by precipitation when reducing the substrate temperature. Since in region 2 the isothermal G growth is limited only to the formation of a few G flakes/islands, a non-uniform G growth underneath h-BN film is obtained, as seen in the OM image of Figure 2.2(c) for 1.5-min C treatment time sample and corresponding Raman intensity mapping of graphene G-peak in Figure 2.2(f). Despite the non-uniform morphology in

region 2 samples, based on the Raman mapping results in Figure 2.2(f), the G almost fully covers the Co surface. This was further verified by G reference sample where 1.5-min C treatment time was used to grow only G at 900 °C, as shown in Figure 2.4. This morphology was observed when the C treatment time changed between 45 seconds and 2 minutes.

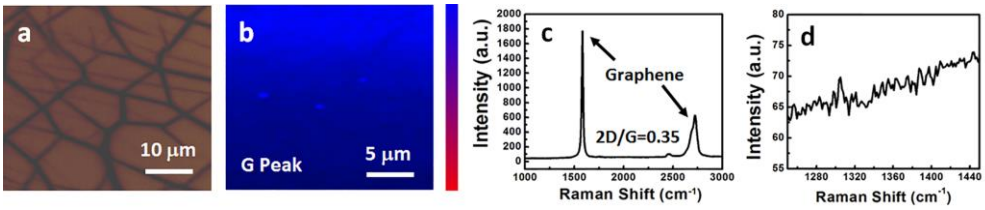

Figure 2.5 G reference sample in region 3. To obtain this sample, the Co substrate was heated up to 900 °C and treated by 3-min C (3 sccm), and then the substrate was cooled to room temperature. (a) OM image, (b) graphene G-peak Raman intensity mapping, (c) typical Raman spectrum of the G reference sample in region 3 with a 2D/G intensity ratio of ~0.35 and (d) a shorter-range Raman spectrum between 1250-1450 cm^{-1} showing no apparent graphene D-peak in the reference sample.

Further introduction of excess C at the growth temperature with the C treatment time exceeding 2 minutes leads the growth mode into region 3. In this region, isothermally grown G has already covered the entire substrate surface at the growth temperature, and after the formation of continuous h-BN on the isothermally grown continuous G layer, additional G layers are formed under the structure during the cooling process, resulting in a uniform heterostructure consisting of thick G and thin h-BN (Figure 2.2(d,g,j) of the sample with 3-min C treatment time). Figure 2.5 shows OM image, graphene G-peak Raman intensity mapping and typical Raman spectrum of the G reference sample with 3-min C treatment time. A 2D/G intensity ratio of ~0.35 was calculated and no graphene D-peak was observed in the spectrum (Figure 2.5(d)), suggesting the high-quality growth of thick G layers. Figure 2.6 shows additional OM images of the h-BN/G samples to further illustrate the evolution of the G morphology in these three regions. Finally, in all three

regions, h-BN is solely deposited at the growth temperature (a condition we referred as isothermally grown or epitaxial), i.e., it is not formed by precipitation mechanism during substrate cooling period. This is because the solubility of both B and N in Co are extremely low [35].

Figure 2.7 shows detailed characterization results of typical region 1 samples. In the SEM images of h-BN/G samples with 5-, 30- and 45-sec C treatment time (Figure 2.7(a-c)), distinct G network morphology appears with a darker color compared to the surrounding area as G produces less secondary electrons compared to the Co metal substrate [36]. The width of G network changes from 5~10 μm for 5-sec C treatment time sample, to 11~13 μm for 30 -sec C treatment time sample, and to 12~16 μm for 45-sec C treatment time sample. It seems that the width of G network increases notably from 5-sec to 30-sec C treatment time and then remains about the same values from 30-sec to 45-sec

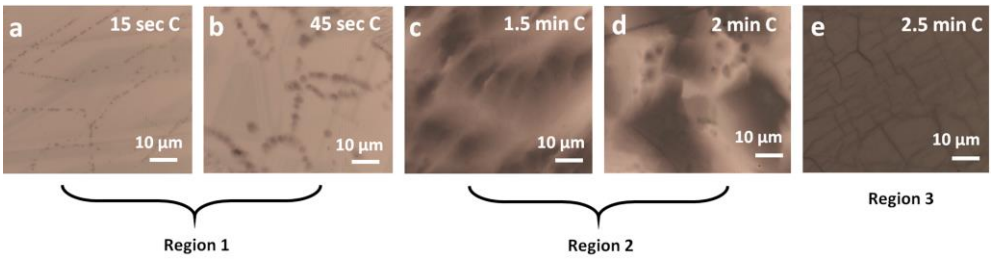

Figure 2.6 Additional OM images of h-BN/G samples with different C treatment time. OM images of h-BN/G samples with (a) 15-sec and (b) 45-sec C treatment time showing the enlargement of G network morphology in typical region 1 samples. By increasing the C treatment time to 1.5 min (c), a mixture of G network morphology and G islands (initially formed at the growth temperature) can be seen. The G morphology evolves towards the formation of more G islands by using 2-min C treatment time (d). This mixture morphology is typical of region 2 samples. By further increasing the C treatment time to 2.5 min (e), the formation of G layers at the growth temperature leads to a thick uniform G film underneath h-BN in region 3 samples.

treatment time, which can be an indication of Co saturation by dissolved C atoms within 45 seconds of C treatment at the growth temperature of 900 °C.

To better understand the h-BN/G network morphology, we transferred the sample with 30-sec C treatment time onto SiO_2/Si substrate and performed AFM measurement (Figure 2.7(d)). The measured AFM line profile reveals that the h-BN film thickness is ~ 2.1 nm and h-BN/G network is ~12.4 nm, suggesting a G network thickness of ~10.3 nm. Figure

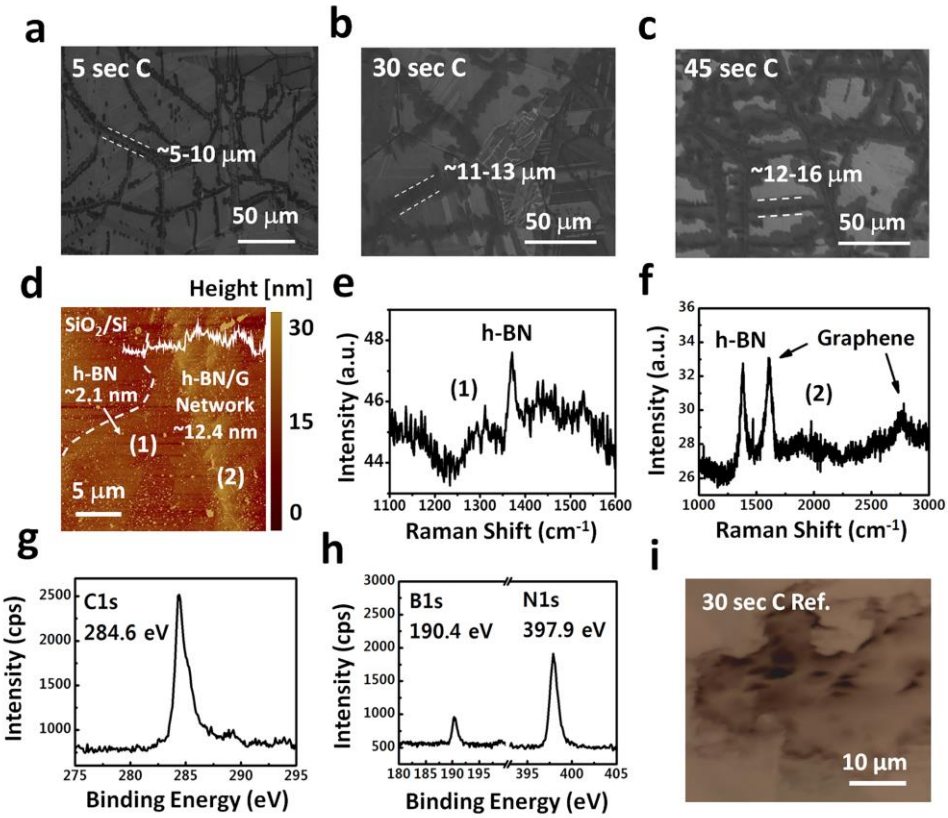

Figure 2.7 Characterizations of h-BN/G samples in region 1. Magnified SEM images of the h-BN/G samples with (a) 5-sec, (b) 30-sec, and (c) 45-sec C treatment time showing the G network morphology. (d) AFM image of h-BN/G sample with 30-sec C treatment time transferred onto SiO_2/Si substrate. (e) and (f) Raman spectra of the points (1) and (2) of (d), respectively. XPS signals of (g) C1s, and (h) B1s and N1s for as-grown h-BN/G sample with 30-sec C treatment time. (i) OM image of the G reference sample with 30-sec C time.

2.7(e) and (f) show Raman spectra of h-BN and h-BN/G network areas (1) and (2), respectively, marked in the AFM image in Figure 2.7(d). It can be clearly seen that the point (1) only shows the h-BN E_{2g} vibrational mode at ~1367 cm^{-1} (Figure 2.7(e)), while point 2 shows the co-existence of h-BN and multilayer G peaks (Figure 2.7(f)) [25-28]. Raman results suggest that h-BN is continuous although G is not in the region 1 samples. Figure 2.7(g) and (h) show C1s, and B1s and N1s XPS spectra of a 30-sec C treatment sample, respectively. C1s peak occurs at 284.6 eV indicating the existence of C sp^2 bonding of G layers [37,38]. B1s and N1s exhibit energy positions at 190.4 eV and 397.7 eV, respectively, which is consistent with the reported values for XPS signals of h-BN [39,40]. By using sensitivity factors from the instrument manufacturer and calculating the atomic % of each atom, the B/N ratio is 1.03, suggesting an almost equal composition of B and N elements.

Figure 2.7(i) shows an OM image of a C-only reference sample. To grow this sample, the Co foil substrate was heated up to 900 ºC, treated with 30-sec C exposure and then cooled to room temperature. As it can be seen in Figure 2.7(i), the G morphology in the C reference sample is quite different with G morphology of h-BN/G sample with the same amount of C treatment time (Figure 2.2(b)). This difference in G morphology is believed to be caused by the top h-BN film rather than the Co substrate because the density of the Co substrate grain boundaries and imperfection sites in both h-BN/G and G reference samples should be about the same and uniformly distributed across the substrate's surface. The fact that the G in region 1 samples is only formed by precipitation during the cooling process, that is after h-BN film growth, makes the G morphology affected by the h-BN

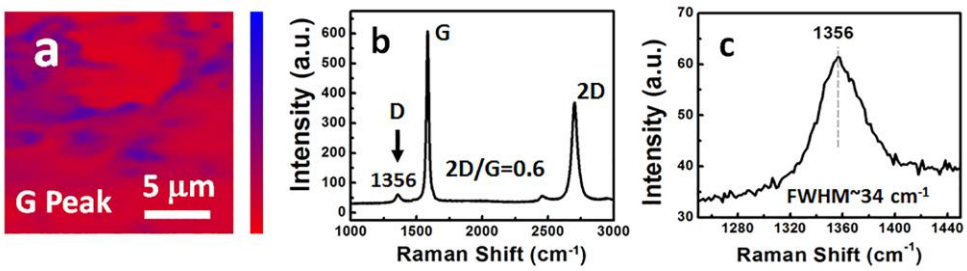

Figure 2.8 G reference sample in region 1. To obtain this sample, the Co substrate was heated up to 900 °C and treated by 30-sec C (3 sccm), and then the substrate was cooled to room temperature. (a) graphene G-peak Raman intensity mapping, (b) typical Raman spectrum of the G reference sample in region 3 with a 2D/G intensity ratio of ~0.6 and (c) a shorter-range Raman spectrum between 1250-1450 showing a D peak at ~1356 cm^{-1} with a FWHM of ~34 cm^{-1}.

film. The G network morphology is the outcome of preferential C atom precipitation in the vicinity of h-BN grain boundaries, which have a random distribution within the h-BN film. Figure 2.8 shows characterization results of the G reference sample in region 1 with 30-sec C treatment time. Graphene G-peak intensity mapping of the reference sample (Figure 2.8(a)) shows a more uniform distribution of less intense G-peak compared to that of h-BN/G sample with the same G growth conditions (Figure 2.2(e)). This suggests that when there is no h-BN on top, precipitated C atoms tend to form larger and thinner domains. Also, a D-peak at ~1356 cm^{-1} with a FWHM of ~34 cm^{-1} was observed (Figure 2.8(b,c)), indicating a low quality G growth in this region. Overall, it appears that h-BN growth has the largest effect on the G growth (quality/morphology/thickness) in region 1 samples since the G is formed after h-BN growth. As the G growth mode gradually changes from precipitation during cooling process to isothermal growth at high temperatures (i.e., regions 2 and 3), the effect of top h-BN film on the growth and morphology of underneath G layers becomes less evident.

Figure 2.9 shows characterization results of h-BN/G samples with the same 30-sec C treatment time and different h-BN growth time. It can be seen in the SEM images of Figure 2.9(a-d) that the coverage and size of the triangular h-BN flakes increases as the increase of h-BN growth time and the whole Co substrate surface is almost covered with h-BN as the growth time reaches ~1 hr. Figure 2.9(e) shows h-BN lateral growth speed as a function of growth time. The area of h-BN coverage is obtained by ImageJ software, as illustrated in Figure 2.10 and the growth speed is defined as the area of coverage divided by the growth time. As seen from Figure 2.9(e), the h-BN lateral growth rate is relatively high in the short h-BN growth period (~ 2.5 %/min at 15 minutes), and then gradually decreases to lower values as the growth progresses (~ 1 %/min at 1 hr). This further justifies the continuous

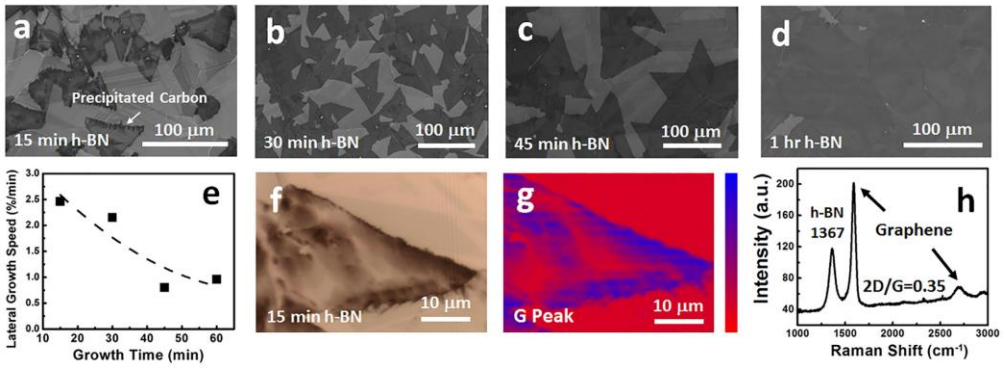

Figure 2.9 H-BN time-dependent growth of region 1 h-BN/G samples with 30-sec C treatment time. (a-d) SEM images of h-BN/G samples with 15-min, 30-min, 45-min and 1-hr h-BN growth duration. (e) h-BN lateral growth speed and triangle edge length for samples in (a-d). (f) OM image and corresponding (g) graphene G-peak Raman intensity mapping and (h) Raman spectrum of (g) at its strongest signal point. H-BN E_{2g} Raman peak at ~1365 cm^{-1} has a FWHM of ~65 cm^{-1} and graphene 2D/G intensity ratio is ~0.35.

morphology of the h-BN films for all samples grown for 3 hours. It should be noted that the SEM image in Figure 2.9(a) and OM image in Figure 2.9(f) of the 15-min h-BN growth sample show the accumulation of C atoms (dark color) around triangular h-BN flakes.

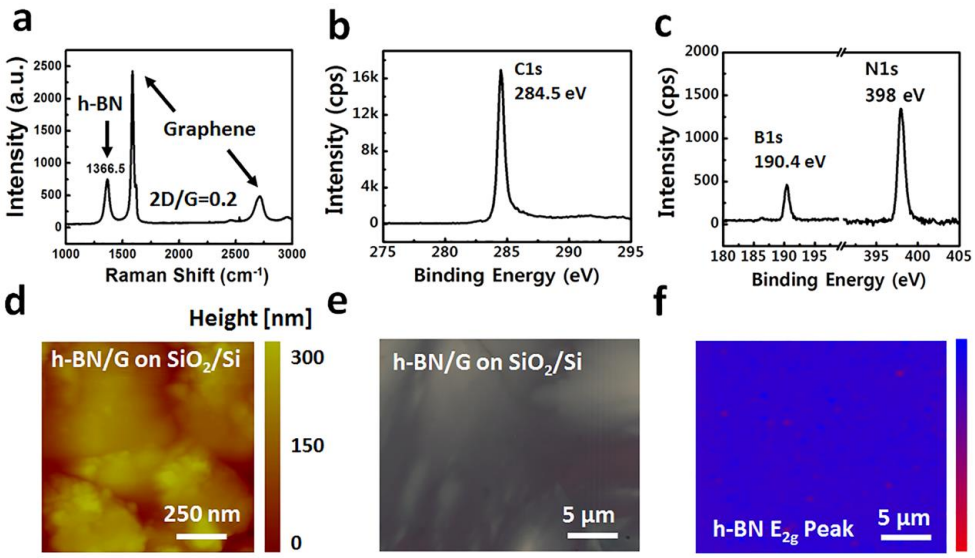

Figure 2.10 Characterization of h-BN/G sample in region 2. (a) Representative Raman spectrum of the as-grown sample. The h-BN E_{2g} Raman peak is centered at ~1366.5 cm^{-1} with the FWHM of ~44 cm^{-1}. These values are very close to the reported values for h-BN [18-20]. A much narrower peak at ~1366.5 cm^{-1} compared to that of Figure 2.9(h) can be partially due to the growth of high-quality G flakes/layers underneath the h-BN film via isothermal growth mode (region 2). The graphene 2D/G intensity ratio is ~0.2 indicating the multilayer nature of G layers in the sample. (b) C1s and (c) B1s and N1s XPS signals of the same sample. (d) AFM image of transferred h-BN/G sample with 1.5-min C treatment time onto SiO_2/Si substrate. (e) OM image of the transferred sample and (f) h-BN E_{2g} phonon peak intensity mapping of (e).

Figure 2.9(g) and (h) show graphene G-peak Raman intensity mapping of Figure 2.9(f) and corresponding Raman spectra from the point of the strongest Raman signal in Figure 2.9(g), respectively. The Raman scattering results clearly support the findings from the microscopy studies in Figure 2.9(a) and (f). This behavior, i.e., C preferential precipitation along h-BN triangle edges and/or grain boundaries during the cooling process, is also consistent with the formation mechanism for the G network underneath the h-BN film of h-BN/G samples in region 1 (Figures 2.2 and 2.7). The graphene 2D/G intensity ratio of the as-grown sample was calculated ~0.35 (Figure 2.9(h)) which is much lower than that of G reference sample in region 1, that is ~0.6 (Figure 2.8(b)). This further shows the effect

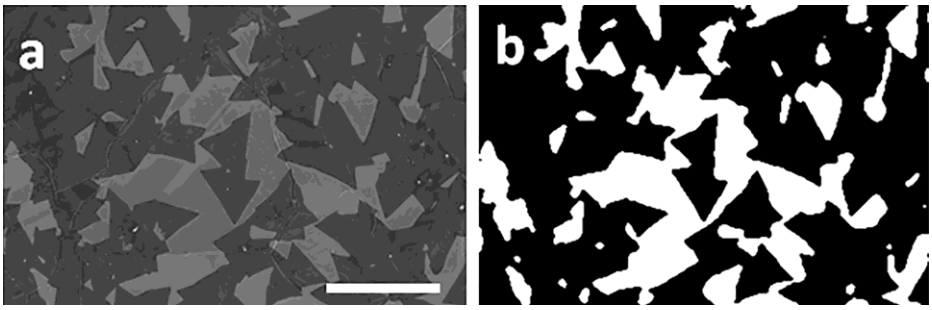

Figure 2.11 An example of h-BN/G coverage calculation for h-BN time-dependent growth samples using ImageJ software. First, an area of ~1 mm^2 from an SEM image was selected for each sample. (a) shows the SEM selected area for the h-BN/G sample grown with 30-sec C treatment time and 30-min h-BN growth time at 900 ºC. (b) By applying a black/white contrast threshold, h-BN flakes are identified with black color. Subsequently, the software measured the black area and divided it by the total area (~1 mm^2) to calculate the h-BN/G coverage for each sample. The scale bar in (a) is 100 μm.

of top h-BN film on the thickness of underneath G layers in region 1 samples. A wide FWHM of h-BN E_{2g} peak (~65 cm^{-1}) in Figure 2.9(h) can be due to the incorporation of intrinsic graphene D-peak in the sample (Figure 2.8(c)).

Figure 2.11 shows Raman spectrum and C1s, B1s and N1s XPS signals of a representative region 2 sample with a 1.5-min C treatment time, and AFM and OM images of the same sample after the h-BN/G structure was transferred onto a SiO_2/Si substrate and its corresponding h-BN E_{2g} phonon mode intensity mapping. Since the isothermal G growth in this region is limited only to the formation of a few G flakes/islands, the final G morphology in h-BN/G sample is a mixture of isothermal G growth and precipitation during the cooling process, resulting in a non-uniform G film. According to Figure 2.11(f) ,

despite the non-uniform morphology of G growth in this region, the h-BN has been formed continuously and fully covered the sample's surface.

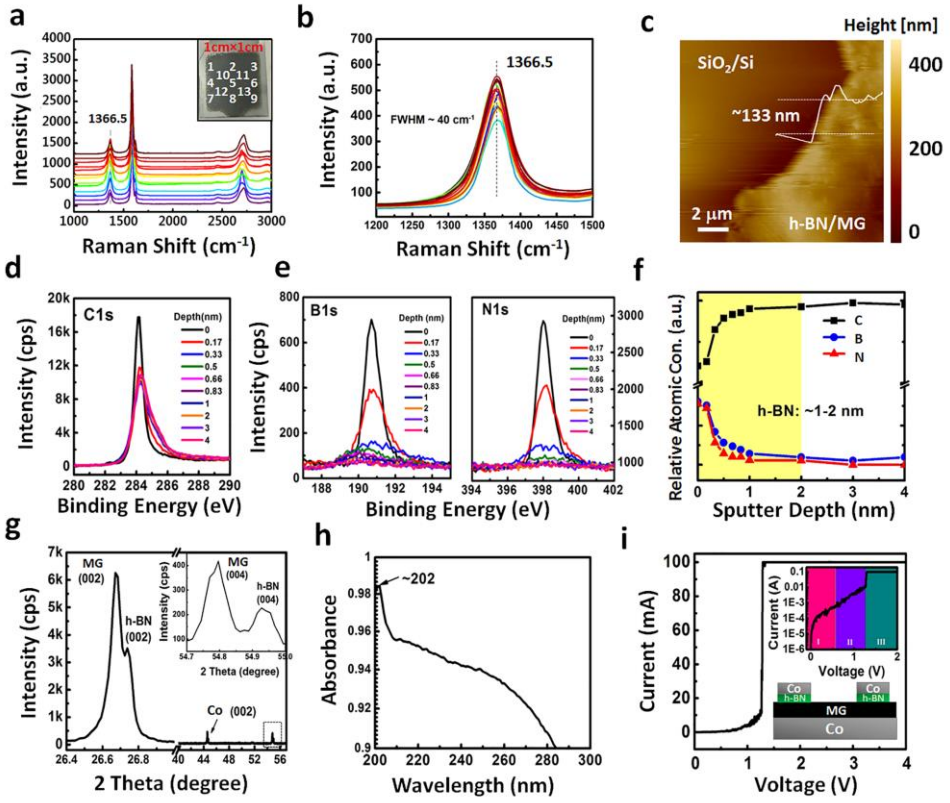

Figure 2.12 Characterization of h-BN/MG samples in region 3. (a) 13-points Raman spectra of the as-grown h-BN/MG sample with 3-min C treatment time and inset shows the sample photograph. The 2D/G ratio of G in this sample was calculated ~0.18. (b) Zoom-in Raman spectra of (a) showing the h-BN E_{2g} phonon mode at ~1366.5 cm^{-1} with a uniform FWHM of ~40 cm^{-1} across these 13 points of measurement. (c) AFM image of the same sample transferred onto SiO_2/Si substrate with the total thickness of ~133 nm. (d) C1s and (e) B1s and N1s as a function of sputtering depth in the depth-profile XPS characterization and (f) relative atomic concentration of C, B, and N versus sputtering depth. (g) XRD spectrum of the same sample. Inset is the magnified spectrum with 2theta from 54.7 to 55°. (h) UV absorption spectrum of the h-BN/MG sample transferred onto a sapphire substrate. (i) I-V characteristic of Co(contact)/h-BN/MG/Co(foil) two-terminal device structure with the contact size of 25μm×25μm. The inset displays the log-scale current versus voltage behavior of the device with 3 distinct regions.

Figure 2.12 shows characterization results of typical h-BN/G samples in region 3. Figure 2.12(a) shows Raman spectra of an as-grown h-BN/G sample with 3-min C treatment time at 13 locations across the 1cm×1cm h-BN/G sample (indicated in a photo image in the inset of Figure 2.12(a)). The existence of both multilayer G (MG or thin graphite) and h-BN Raman peaks is evident. The 2D/G ratio of MG in this sample was calculated ~0.18. Figure 2.12(b) is the zoom-in spectra of Figure 2.12(a) between 1200 and 1500 cm^{-1}, showing excellent uniformity of h-BN E_{2g} phonon mode's position (~1366.5 cm^{-1}), intensity and full width at half maximum (FWHM~40 cm^{-1}) over these 13 points of measurement [41]. A portion of the sample was transferred onto SiO_2/Si substrate for the AFM measurement. The AFM image reveals that the h-BN/G film has a total thickness of ~133 nm (Figure 2.12(c)).

To reveal the individual thickness of h-BN and MG layers, we performed XPS sputtering depth profile measurement. Figure 2.12(d) and (e) show the evolution of C1s, and B1s and N1s XPS signals as a function of sputtering depth within 4 nm of the top surface of h-BN/G sample. As seen in Figure 2.12(d), C1s peak is strongest when the sample was not sputtered, which is due to the inclusion of signals from absorbed C species on the surface or adventitious C [42]. After removing the top 0.17 nm material, the intensity of C1s peak drops significantly compared with the signal before sputtering and then remains about the same with further sputtering while the width of the C1s peak increases as the sputtering depth increases (down to ~1-2 nm) due to Ar^+ beam induced damage. On the other hand, B1s and N1s XPS signals in Figure 2.12(e) decrease proportionally and gradually by removing the top layers and become negligible when the sputtering depth

reaches ~2 nm (i.e., h-BN thickness). Figure 2.12(f) shows the calculated relative atomic concentration for B, N, and C as a function of the sputtering depth. As the sputtering depth increases, both N and B concentrations decrease gradually and reach an insignificant percentage at a sputtering depth of 1~2 nm, while the C concentration gradually levels up and then becomes steady as the etching depth extends from 2 to 4 nm. Considering the AFM (Figure 2.12(c)) and XPS depth-profile (Figure 2.12 (f)) measurement results, it can be concluded that the h-BN/MG structure has a top h-BN layer of 1~2 nm and a bottom MG layer of 131~132 nm. Such a large thickness of MG is believed to be caused mainly by precipitation of dissolved C atoms during cooling process. Much higher substrate cooling rates could significantly reduce the total G thickness, although thermal strained induced wrinkles could compromise the quality of the precipitated G in those cases [43]. Alternatively, other transition metals with much less C solubilities can be used to control the number of G layers down to a few layers [44,45]. Owing to the fact that these C atoms precipitate underneath the isothermally grown MG buffer, the morphological and structural uniformity of h-BN/G samples is well preserved, as inferred from Figure 2.2(c) and (g). Moreover, similar h-BN thickness in region 1 (~2.1 nm) and region 3 (1~2 nm) samples indicates that the h-BN vertical growth is not affected by the G growth mechanism, morphology or thickness (Figures 2.7 and 2.12). The seemly self-limited growth of h-BN on G with different morphology under the present growth condition is intriguing and needs further investigation. Similar self-limited growth of h-BN on metal substrates was also reported [46-50].

Figure 2.12(g) shows XRD pattern of the h-BN/G sample. The evident peaks at 26.64° and 54.79°, and 27.1° and 54.94° are assigned to (002) and (004) crystal plane diffractions of MG and h-BN films according to JCPDS card numbers 41-1487 and 34-0421, respectively [51,52]. The small peak at 51.5° is from (002) crystal plane diffraction of hcp Co (JCPDS# 01-071-4239) [53,54]. Such intense XRD peaks indicate the high-quality of MG and h-BN films in the sample. It can be also realized that h-BN and MG have grown on the same crystal planes, suggesting the epitaxial relation between the stacked layers. To further confirm the relation between h-BN and MG, we transferred a piece of the same sample and performed TEM measurement (Figure 2.13). Figure 2.13(a) shows the bright-field top-view image of the transferred film on the TEM grid and Figure 2.13(b) shows the SAED pattern obtained from the area in Figure 2.13(a). A single hexagonal pattern is

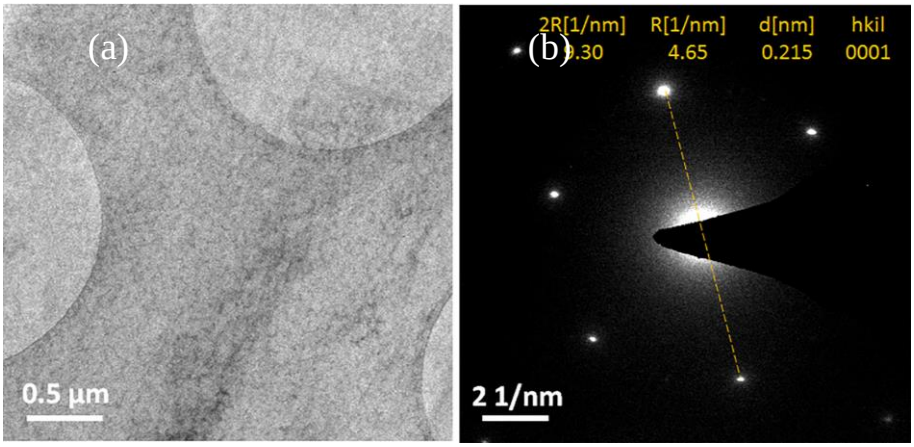

Figure 2.13 TEM measurement on the h-BN/G sample in region 3. (a) Bright-field top-view image of the transferred h-BN/G on the TEM grid and (b) corresponding SAED pattern of (a). A single hexagonal pattern can be observed in (b), however, the dots are slightly elongated, suggesting overlapping hexagonal patterns of h-BN and MG films with possibly a little miss-orientation. This proves the epitaxial relation of h-BN and MG stacked layers.

observed (Figure 2.13(b)); however, the dots are slightly elongated, suggesting overlapped hexagonal patterns of h-BN and MG films with possibly a little miss-orientation. Figure

2.12(h) shows an absorption spectrum of the sample after a portion of the h-BN/MG film was transferred to a sapphire substrate. As can be seen in Figure 2.12(h), the clear absorption edge at ~202 nm originates from the band gap of h-BN film [55]. A big portion of UV light spectrum has been also absorbed by the thick MG film [56]. Figure 2.12(i) shows cross-plane I-V characteristic of a Co(contact)/h-BN/G/Co (substrate) two-terminal device. The bottom inset shows a schematic of the device, which was fabricated using a process described in the Experimental section. The top inset displays the log-scale current versus voltage behavior of the device, showing 3 distinct regions: I) current linearly increases as the increase of voltage, which represents direct-tunneling related conduction ($V<\sim0.6$) [57,58], II) current nonlinearly/exponentially increases with the voltage under moderate biases ($\sim0.6<V<\sim1.25$) due to the Fowler-Nordheim tunneling mode [59,60], and III) current sharply increases due to the dielectric breakdown at a bias of 1.25 V [61]. The calculated breakdown electric field based on an h-BN thickness of 1~2 nm is 6.25-12.5 MV/cm, which is comparable with the observed values from other epitaxial h-BN films [61-63].

2.4. **Conclusion**

We performed a systematic study of the in-situ growth of h-BN/G films on Co substrate by sequentially introducing C source with a high C incorporation, and B and N sources in an MBE system. It is found that the continuous h-BN/G heterostructures can be formed at a substrate temperature of 850~900 ºC. By changing the C amount incorporation, the h-BN/G structure alters from region 1 where G network is formed only by precipitation during cooling process underneath the h-BN film; to region 2 where isothermal G growth

occurs to form G islands partially covering the substrate, followed by further precipitation G growth, leading to a non-uniform h-BN/G structure, and to region 3 where a uniform h-BN/G heterostructure with a thin continuous h-BN and a thick continuous MG are formed from both isothermal G growth and precipitation. It is found out that the top h-BN film has the largest effect on the morphology, thickness and quality of underneath G layers in h-BN/G samples of region 1. In addition, the h-BN growth is self-limited to a 1~2 nm thick film in all three regions, regardless of the underneath G thickness or morphology.

2.5. **References**

[1]Nag A., Raidongia K., Hembram K. P. S. S., Datta R., Waghmare U. V. and Rao C. N. R. 2010 *ACS Nano* **4** 1539

[2] Liu L., Feng Y. P. and Shen Z. X. 2002 *Phys. Rev. B* **68** 104102

[3] Watanabe K., Taniguchi T. and Kanda H. 2004 *Nat. Mat.* **3** 404

[4] Hattori Y., Taniguchi T., Watanabe K. and Nagashio K. 2015 *ACS Nano* **9** 916

[5] Kim S. M *et al* 2015 *Nat. Commun.* **6** 8662

[6] Novoselov K. S. A., Mishchenko A., Carvalho A. and Castro Neto A. H. 2016 *Science* **353** 9439

[7] Xia W., Dai L., Yu P., Tong X., Song W., Zhang G. and Wang Z. 2017 *Nanoscale* **9** 4324

[8] Schulman D.S., Arnold A.J., Razavieh A., Nasr J. and Das S. 2017. *IEEE Nanotechnol. Mag*. **11** 6

[9] Yankowitz M., Xue J., Cormode D., Sanchez-yamagishi J. D., Watanabe K., Taniguchi T., Jarillo-Herrero P., Jacquod P. and LeRoy B. J. 2012 *Nat. Phys.* **8** 382

[10] Aggoune W., Cocchi C., Nabok D., Rezouali K., Belkhir M. A. and Draxl C. 2017 *J. Phys. Chem. Lett.* **8** 1464

[11] Dean C. R. *et al* 2013 *Nature* **497** 598

[12] Cheng R. *et al* 2017 *Appl. Phys. Lett.* **110** 173507

[13] C. R. Dean *et al* 2010 *Nat. Nanotechnol*. **5** 722

[14] Amet F., Williams J. R., Garcia A. G. F., Yankowitz M., Watanabe K., Taniguchi T. and Goldhaber-Gordon D. 2012. *Phys. Rev. B* **85** 073405

[15] Britnell L. *et al* 2012 *Science* **335** 947

[16] Novoselov K. S., Jiang D., Schedin F., Booth T. J., Khotkevich V. V., Morozov S. V. and Geim A. K. 2005 *Proc. Natl. Acad. Sci. U.S.A.* **102** 10451

[17] Pacile D., Meyer J. C., Girit C. O. and Zettl A. 2008 *Appl. Phys. Lett.* **92** 133107

[18] Liu Z., Song L., Zhao S., Huang J., Ma L., Zhang J., Lou J. and Ajayan P. M. 2011 *Nano. Lett.* **11** 2032

[19] Gao T., Song X., Du H., Nie Y., Chen Y., Ji Q., Sun J., Yang Y., Zhang Y. and Liu Z. 2015 *Nat. Commun.* **6** 6835

[20] Wu Q., Jang S. K., Park S., Jung S. J., Suh H., Lee Y. H., Lee S. and Song Y. J. 2015 *Nanoscale* **7** 7574

[21]Summerfield A. *et al* 2016 *Sci. Rep.* **6** 22440

[22] Wofford J. M., Nakhaie S., Krause T., Liu X., Ramsteiner M., Hanke M., Riechert H. and Lopes J. M. 2017 *Sci. Rep*. **7** 43644

[23] Plaut A. S. *et al* 2017 *Carbon* **114** 579

[24] Driver M. S., Beatty J. D., Olanipekun O., Reid K., Rath A., Voyles P. M. and Kelber J. A. 2016 *Langmuir* **32** 2601

[25]Zheng R., Khanaki A., Tian H., He Y., Cui Y., Xu Z. and Liu J 2107 *Appl. Phys. Lett.* **111** 011903

[26]Xu Z., Zheng R., Khanaki A., Zuo Z. and Liu J. 2015 *Appl. Phys. Lett.* **107** 213103

[27]Zuo Z., Xu Z., Zheng R., Khanaki A., Zheng J.-G and Liu J. 2015 *Sci. Rep.* **5** 14760

[28]Xu Z., Khanaki A., Tian H., Zheng R., Suja M., Zheng J.-G. and Liu J. 2016 *Appl. Phys. Lett.* **109** 043110

[29]Ishida K. and Nishizawa T. 1991 *J. Phase Equilib.* **12** 417

[30] Zheng M. *et al* 2010 *Appl. Phys. Lett.* **96** 063110

[31] Kassab L. R. P., Martinelli J. R., dos Santos A. D., Ribeiro S. J. L. and dos Santos M. V. 2016 *Mater. Res.* **19** 669

[32] McCarty K. F., Feibelman P. J., Loginova E. and Bartelt N. C. 2009 *Carbon* **47** 1806

[33] Baraton L., He Z. B., Lee C. S., Cojocaru C. S., Châtelet M., Maurice J-L., Lee Y. H. and Pribat D. 2011 *Europhys. Lett.* **96** 46003

[34] Hamilton J. C. and Blakely J. M. 1980 *Surf. Sci.* **91** 199

[35] Hu X., Björkman T., Lipsanen H., Sun L. and Krasheninnikov A. V. 2015 *J. Phys. Chem. Lett.* **6** 3263

[36] Luo J., Tian P., Pan C.-T., Robertson A. W., Warner J. H., Hill E. W. and Briggs G. A. D. 2011 *ACS Nano* **5** 1047

[37] Ci L. *et al* 2010 *Nat. Mat.* **9** 430

[38]Zheng R., Xu Z., Khanaki A., Tian H., Zuo Z., Zheng J.-G. and Liu J. 2017 *Thin Solid Films* **627** 39

[39] Xu Z., Tian H., Khanaki A., Zheng R., Suja M. and Liu J. 2017 *Sci. Rep.* **7** 43100

[40] Tonkikh A. A, Voloshina E. N., Werner P., Blumtritt H., Senkovskiy B., Güntherodt G., Parkin S. S. P. and Dedkov Y. S. 2016 *Sci. Rep*. **6** 23547

[41] Gorbachev R. V. *et al* 2011 *Small* **7** 465

[42] Barr T. L. and Seal S. 1995 *J. Vac. Sci. Technol., A* **13.3** 1239.

[43] Choi D. S., Kim K. S., Kim H., Kim Y., Kim T. Y., Rhy S.-H., Yang C.-M., Yoon D. H. and Yang W. S. 2014 *ACS Appl. Mater. Interfaces* **6** 9574

[44]Zhao P., Kumamoto A., Kim S., Chen X., Hou B., Chiashi S., Einarsson E., Ikuhara Y. and Maruyama S. 2013 *J. Phys. Chem. C* **117** 10755

[45] Takesaki Y., Kawahara K., Hibino H., Okada S., Tsuji M. and Ago H. 2016 *Chem. Mat.* **28** 4583

[46] Orofeo C. M., Suzuki S., Kageshima H. and Hibino H. 2013 *Nano Res.* **6** 335.

[47] Shi Y. *et al* 2010. *Nano Lett.* **10** 4134.

[48] Jang S. K., Youn J., Song Y.J. and Lee S. 2016 *Sci. Rep*. **6** 30449.

[49] Preobrajenski A. B., Vinogradov A. S. and Mårtensson N. 2005 *Surf. Sci.* **582** 21.

[50] Morscher M., Corso M., Greber T. and Osterwalder J. 2006 *Surf. Sci.* **600** 3280.

[51] Stobinski L., Lesiak B., Malolepszy A., Mazurkiewicz M., Mierzwa B., Zemek J., Jiricek P. and Bieloshapka I. 2014 *J. Electron. Spectrosc. Relat. Phenom*. **195** 145

[52] Bhimanapati G. R., Kozuch D. and Robinson J. A. 2014 *Nanoscale* **6** 11671

[53] Chioncel F. M. and Haycock W. P. 2005 *Chem. Vap. Deposition* **11** 235

[54] Khanaki A., Xu Z., Tian H., Zheng R., Zuo Z., Zheng J.-G. and Liu J. 2017 *Sci. Rep*. **7** 4087

[55] Zhang C., Zhao S., Jin C., Koh A. L., Zhou Y., Xu W., Li Q., Xiong Q., Peng H. and Liu Z. 2015 *Nat. Commun*. **6** 6519

[56] Meng J. H., Zhang X. W., Wang H. L., Ren X. B., Jin C. H., Yin Z. G., Liu X. and Liu H. 2015 *Nanoscale* **7** 16046

[57] J. G. Simmons 1963 *J. Appl. Phys*. **34** 2581

[58] Lee G. H., Yu Y. J., Lee C., Dean C., Shepard K. L., Kim P. and Hone J. 2011 *Appl. Phys. Lett.* **99** 243114

[59] Pandey S. *et al* 2014 *Nanoscale* **6** 3410

[60] Ji Y. et al 2016 *Appl. Phys. Lett*. **108** 012905

[61] Britnell L. *et al* 2012 *Nano Lett.* **12** 1707

[62] Hui F., Pan C., Shi Y., Ji Y., Grustan-Gutierrez E. and Lanza M. 2016 *Microelectron. Eng.* **163** 119

[63] Hattori Y., Taniguchi T., Watanabe K. and Nagashio K. 2016 *Appl. Phys. Lett.* **109** 253111

Chapter 3 The Role of Carbon Interstitials in Transition Metal Substrates on Controllable Synthesis of High-Quality Large-Area Two-Dimensional Hexagonal Boron Nitride Layers

3.1. Introduction

Hexagonal boron nitride (h-BN), a two-dimensional (2D) isostructure of graphene, has gained significant attention for its remarkable properties,[1-3] as well as its potential applications as a 2D dielectric[4-7]and a wide bandgap semiconductor material.[3,8,9] To realize the technological potential of h-BN, the key is reliable and controllable synthesis of large-area h-BN. Toward this direction, tremendous effort has been made on chemical vapor deposition (CVD) of h-BN on various catalytic transition metal substrates, including Cu,[2,10,11] Co,[12] Ni,[13-16] Fe,[17-19] Ru[20] and Pt.[21] Experiments have proven that transition metals can provide a favorable chemical environment for the synthesis of high-quality graphene and h-BN. In addition, rational engineering of catalytic effects of the transition metal substrates by alloying or incorporating additional species has been utilized in the growth of both h-BN and graphene to enhance the control over layer number, nucleation density, and domain size. [17,19,22] Recently, CVD growth of graphene and h-BN assisted by carbon in the form of α-C or hydrocarbon gas has been reported by pre-depositing PMMA[23] or simultaneously introducing methane,[24] respectively. Nevertheless, the growth of h-BN on transition metal substrates incorporated with carbon as interstitial atoms has not been studied. Transition metals with high carbon solubility are commonly thought to be detrimental for graphene growth, due to the precipitation of low-quality graphitic structure during substrate cooling, resulting in poor layer number controllability.[25] However, from a completely different perspective, the high carbon

solubility of metals ensures the presence of a substantial amount of dissolved carbon atoms as interstitials. As a result, the tuning of carbon concentration in a wide range within the carbon solubility's limit can bring a new dimension of control for the growth of h-BN in addition to other regular growth parameters such as substrate temperature, growth pressure, surface roughness, and so on. Thus, to elucidate the effect of interstitial carbon on the growth of h-BN, it is essential to control the carbon concentration precisely at a trace level so that the carbon atoms do not end up precipitating onto the metal surface. From this standpoint, molecular beam epitaxy (MBE), an alternative to CVD, has the ability to precisely control solid, gas, and plasma sources and tune the growth parameters. Some general comparison of MBE and CVD for 2D material synthesis can be found elsewhere, [26-35] and MBE has been demonstrated to be a reliable method to grow 2D h-BN and h-BN/graphene heterostructures.[26-35]

In this work, we carefully prepared Co and Ni substrates with different carburization time using acetylene gas prior to the growth of h-BN in a plasma-assisted MBE system. The dissolution of carbon atoms in Co enabled and enhanced the direct growth of h-BN on the Co surface. A scanning electron microscopy (SEM) study of h-BN grown on Co with different carburization levels shows that the morphology as well as the lateral growth speed of the h-BN domains can be readily controlled by carbon concentration. The morphology varies from 2D layer-plus-3D islands to homogeneous 2D layers. Comprehensive characterizations including transmission electron microscopy (TEM), Raman spectroscopy, atomic force microscope (AFM), UV-Vis absorption spectroscopy and X-ray photoelectron spectroscopy (XPS) were carried out to study the structural and

compositional properties of the samples. H-BN dielectric properties were characterized based on Co(foil)/h-BN/Co(contact) devices. Density functional theory (DFT) studies show enhanced adsorption and diffusion of both B and N atoms on the Co metal surface as a result of embedded carbon interstitials, which shed light on the role of carbon interstitials in transition metal substrates for reliable and controllable growth of large-area 2D h-BN.

3.2. **Experimental details**

Table 3.1 Summary of samples.

Step	Parameters	Sample A	Sample B1-B5	Sample C1-C4	Sample D1-D7	Sample E1, E2
Hydrogen Annealing	Substrate	Co	Co	Co	Co	Ni
	Temperature (°C)	900	900	900	900	900
	Hydrogen gas flow (sccm)	10	10	10	10	10
	Duration (mins)	10	10	10	10	10
Carburization	Temperature (°C)	--	900	900	900	900
	Acetylene gas flow (sccm)	--	0.5	0.5	0.5	0.5
	Duration (s)	--	60	***60, 120, 180, 240***	***15, 30, 45, 60, 120, 180, 240***	***180, 300***
H-BN Growth	Substrate temperature (°C)	900	900°	900	900	900
	Boron cell temperature (°C)	1150	1150	1150	1150	1150
	Ammonia gas flow (sccm)	5	5	5	5	5
	Nitrogen gas flow (sccm)	10	10	10	10	10
	Nitrogen ECR current (mA)	60	60	60	60	60
	Duration (mins)	180	***15, 30, 60, 90, 180***	60	180	360

Substrate preparation Co and Ni foils with a thickness of 0.1 mm and a purity of 99.995% from Alfa Aesar were polished on a SBT 920 Lapping and Polishing workstation and cut into 1 cm × 1 cm pieces as substrates. These pieces were degreased and deoxidized with acetone, IPA and dilu1ted hydrochloric acid (10%), rinsed in deionized (DI) water, blown dry and finally loaded into an MBE chamber. A negligible amount of carbon impurities existed in as-received Co foils (0-6 ppm according to Alfa Aesar' glow discharge mass spectrometry report). Co substrates without the carburization process are referred to as pristine Co.

Hydrogen annealing and carburization A re-designed Perkin-Elmer MBE system with a background pressure of ~10^{-9} Torr was used for the sample growth. The substrate was heated to 900 ºC and annealed at this temperature under a 10-sccm flow of hydrogen gas for 10 minutes. Then, 0.5-sccm C_2H_2 gas was introduced into chamber with a pressure of 5×10^{-5} Torr for 15 to 240 s to enrich Co with carbon prior to h-BN growth. H-BN growth step started after the carburization process.

H-BN growth A Knudsen effusion cell filled with B_2O_3 powder (Alfa Aesar, 99.999% purity) was used as boron (B) source. Nitrogen plasma (Airgas, 99.9999% purity) generated by an electron cyclotron resonance (ECR) system and high-purity ammonia (American Gas Group, 99.9995% purity) were used as nitrogen (N) sources. The h-BN growth was conducted by simultaneous introduction of B and N sources onto the Co substrate at 900 ºC. B cell temperature was maintained at 1150 ºC. N sources consisting of 10-sccm N_2 gas through an ECR plasma source and NH_3 gas at a flow rate of 5 sccm through a shut-off valve were introduced to the chamber. The ECR current was set at 60 mA with a power of 228 W. The growth pressure was on the order of 6×10^{-4} Torr. After the growth, the samples were cooled to room temperature at a rate of 10 ºC/min. Detailed growth conditions are summarized in Table 3.1.

Transferring of h-BN samples The Co and Ni substrates were etched by $FeCl_3$/HCl solution after spin-coating PMMA (495 A4) on as-grown samples. The PMMA/h-BN stack was then transferred into 10% HCl, 5% HCl and DI water successively to rinse out the residual etchant. The floating h-BN film was taken out by a desired substrate and left to dry for at least 12 hours. After that, a few drops of PMMA were deposited again on the

transferred film and soaked for another two hours. The additional PMMA is used to soften the previous PMMA layer and enhance the attachment of h-BN on the substrate. PMMA was removed by dipping the sample into acetone bath. Finally, the sample was annealed at 400 °C inside a CVD furnace for 3 hours in Ar/O_2 flow of 300 sccm to remove any remaining organic residue.

Characterizations SEM images were acquired using an FEI NNS450 system in secondary electron (SE) imaging mode with a beam voltage of 10 kV. Raman characterizations were performed using a HORIBA LabRam system equipped with a 60-mW, 532-nm green laser. XPS characterization was conducted using a Kratos AXIS ULTRA XPS system equipped with an Al Kα monochromatic X-ray source and a 165-mm mean radius electron energy hemispherical analyzer. The fitting of XPS data was performed using CasaXPS software. As-measured XPS data was first calibrated by using Co $2p_{3/2}$ peak at 778.1 eV (Lorentzian Asymmetric line shape). B 1s, N 1s and C 1s peaks were convoluted with Gaussian/Lorentzian line shape after background-corrected by Shirley type background. AFM images were obtained using a Veeco D5000 AFM system. TEM images and selected area electron diffraction (SAED) patterns were acquired using a FEI Tecnai12 system. TEM sample was prepared by picking a transferred h-BN film using a 200-mesh Cu grid covered with holey carbon film with orthogonal array of 1.2-μm diameter holes.

Device fabrication and electrical measurement Co(foil)/h-BN/Co(contact) two-terminal devices were fabricated by a standard photolithography and lift-off process. A Co layer of 100 nm was patterned as top square contacts with an edge length of 200 μm on the

surface of as-grown h-BN film. Reactive ion etching (RIE) was performed with a 50-sccm SF_6 plasma, under a power of 50 W, and for 15 seconds to etch the h-BN film between devices, which ensured isolation of different devices on the same substrate. Current-voltage (I-V) characteristics were obtained by an Agilent 4155C semiconductor parameter analyzer equipped with probing tips having a diameter of about 5 μm (Signatone, SE-TL).

DFT calculations First-principles density functional theory (DFT) calculations used the projector augmented wave method and the Perdew-Burke-Ernzerhof (PBE) type generalized gradient approximation[36,37]as implemented in the software package VASP.[74] Spin polarization was included self-consistently in all calculations. For the unit cell calculations, a Monkhorst-Pack scheme was adopted to integrate over the Brillouin zone with a k-mesh of 9×9×1. A plane-wave basis cutoff of 550 eV was used. All structures were optimized until the largest force on the atoms was less than 0.01 eV/Å. To model the adsorption energies of B and N atoms on the Co (111) surface, a single B or N atom was placed on specific sites of the surface of a supercell consisting of four atomic layers of 4×4 Co atoms in the (111) plane. These sites include the top of the Co atoms, hexagonal closely packed (HCP), and face centered cubic (FCC) sites of the Co (111) surface, on which the adsorption of B or N atoms would enable an epitaxial relationship between h-BN and the Co (111) substrate. A vacuum gap of 15 Å was introduced to avoid interactions between the periodically repeated surfaces. To simulate the diffusion activation energies, we adopted the climbing image nudged elastic band (CI-NEB) method[38]. The spring force between adjacent images was set to 5.0 eV/Å. The migration energies, namely diffusion activation energies were obtained for the different adsorbates between the different sites of

the Co (111) surface. The initial and final positions of the adsorbed atoms were set at two HCP sites of the surface. 8 images were considered to calculate the activation energies between the initial and final states.

3.3. **Results and discussion**

As-received Co and Ni foils were polished, cleaned, and transferred to the MBE for growth, using a growth procedure illustrated in Figure 3.1. The Co surfaces are dominated with (111) orientation, as can be seen from an x-ray diffraction pattern of as-grown samples (Figure 3.2). Table 3.1 summarizes the growth conditions of all h-BN samples on pristine

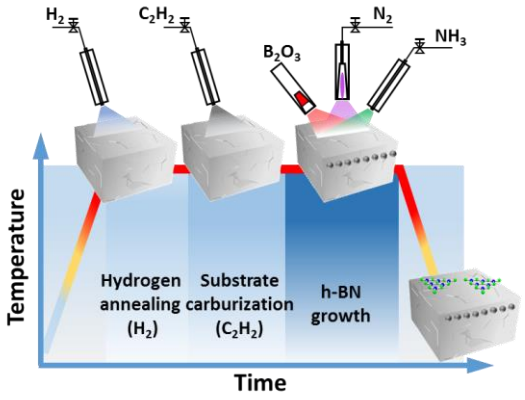

Figure 3.1 Schematic of MBE growth steps. Five colored regions indicate five growth steps including temperature ramping, hydrogen annealing, substrate carburization, h-BN growth and cooling.

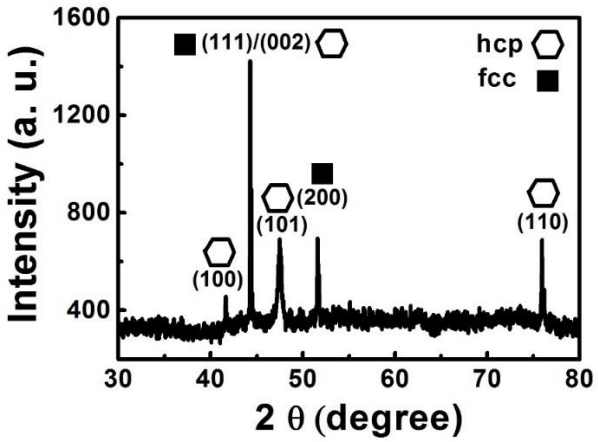

Figure 3.2 XRD pattern of 180-min h-BN sample with 240-s carburization time (Sample D6). Peak assignment shows the co-existence of Co hcp and fcc phases, according to JCPDS cards# 01-071-4239 and 01-071-4651, respectively.

Co (Sample A), carburized Co substrates (Samples B1-B5, C1-C4, and D1-D7), and carburized Ni substrates (Samples E1-E2) that are described here. Direct growth of h-BN on pristine Co was reported previously, however, those h-BN films were grown at a relatively low temperature of 850 ºC; thus the quality of the films was good but not excellent, which is inferred from a breakdown electric field of only 3 MV/cm.[31] In this work, all samples were grown at a higher substrate temperature of 900 ºC in order to enhance the quality of the films. Surprisingly, with all other growth conditions the same as or similar to that used in Ref. 31, the attempt towards the growth of h-BN onto pristine Co substrate at 900 ºC led to no growth of any material on the surface (for example, Sample A), as verified by characterizations such as SEM, optical microscopy, Raman and XPS (Figure 3.3). The main reason is associated with high desorption of B on the metal surface, which is later confirmed by the theoretical calculation of adsorption energy. On the other hand, h-BN has been reliably grown onto all carburized Co substrates at 900 ºC (Samples B1-B5, C1-C4, D1-D7). Vacuum carburization has been widely used for synthesis of

carbon steel by exposing iron in a hydrocarbon environment.[39] Here, carburization of Co substrates was performed by introducing C_2H_2 gas with various flux rates and time at the growth temperature to attain different amounts of carbon incorporation in the substrates, as detailed in the Experimental details section.

Figure 3.4a shows an SEM image of a typical sample (Sample B5) taken at its center region. Growth conditions of this sample are shown in Table 3.1. The brighter regions correspond to prism-shaped multilayer h-BN islands ("prisms" in short) due to the charging effect, and darker regions indicate the presence of an h-BN film. Thus, the h-BN film consists of high-density prisms atop of a continuous thin film. The edge length of a typical

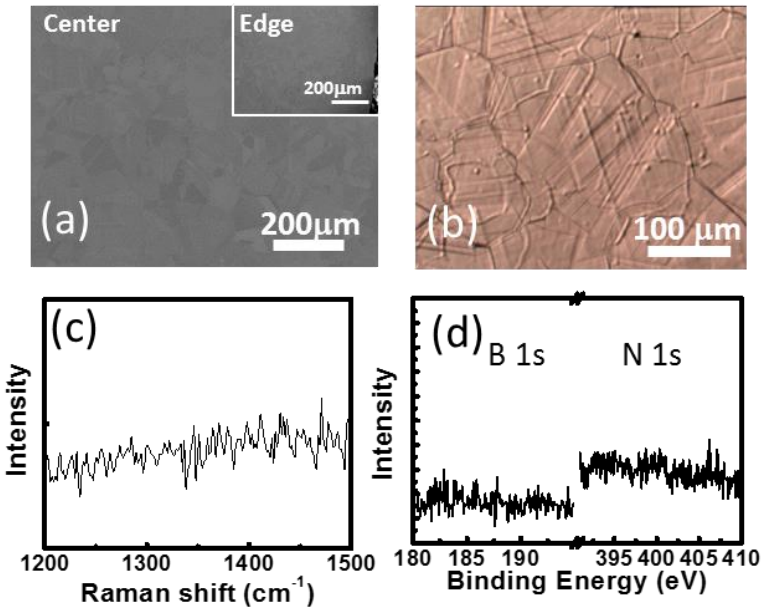

Figure 3.3 Characterization of reference sample: h-BN growth on pristine Co foil (Sample A). (a) SEM image in the center and edge (inset). (b) OM image of sample surface. (c) Raman spectrum. (d) XPS spectrum at B 1s and N 1s.

prism is around 10 μm (Figure 3.4a inset). To show the contrast between the thin h-BN film and Co substrate, An SEM image was also taken at the edge of the sample where the density of the "prisms" is much lower (Figure 3.4b). The part covered by h-BN shows

darker color due to the less secondary electrons generated from h-BN than from Co.[40] The film is further transferred onto a Si substrate covered with a 300-nm SiO_2. Compared with the SEM image of the area on the as-grown sample, the transferred film looks continuous and intact. Figure 3.4c shows a typical Raman spectrum of a prism on the as-grown sample, showing a characteristic E_{2g} phonon mode at 1366 cm^{-1} with a full width at half maximum (FWHM) of 16 cm^{-1}.[41] No graphite related Raman peaks are observed between 1250 and 3000 cm^{-1}, indicating no carbon-related film growth. A simple partial etching experiment is designed to visualize the trace of carbon in Co substrate (Section 8). From Raman spectra, the interface between Co and h-BN is confirmed to be free of C-

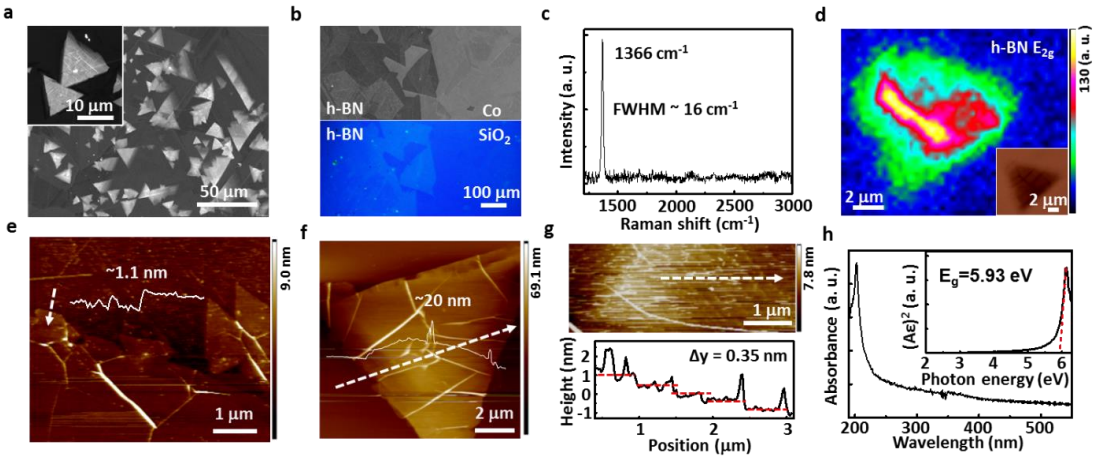

Figure 3.4 Characterization of an h-BN sample grown with 60-s carburization and for 180 minutes. (a) SEM image of the sample, showing 2D layer-plus-3D islands morphology. The inset is an image with higher magnification, indicating the size of a typical prism-shaped h-BN island. (b) SEM and optical microscope images of as-grown (top) and transferred (bottom) sample on the sample edge. (c) Raman spectrum measured at the center of a prism-shaped island. (d) Raman mapping on an as-grown prism-shaped island with corresponding optical micropscopy image shown in inset at the right bottom corner. (e) AFM image and its scan profile on the few-layer region of a transferred h-BN sample on SiO_2/Si. (f) AFM image and its scan profile across a prism-shaped island. (g) AFM image and scan profile on the side wall of a prism-shaped island. The height profile was obtained along the white arrow direction illustrated in the image. (h) UV-Vis absorption spectrum of a transferred h-BN sample on sapphire. Inset is $(A\varepsilon)^2$ versus ε curve.

related structure, while α-C network structure is embedded in Co grain boundaries (Figure 3.5), which can be explained by insufficient carbon concentration, high carbon solubility and low carbon diffusion coefficient in Co.[42]

Figure 3.4d shows an h-BN E_{2g} peak Raman mapping image around a prism-shaped island area (the inset is an optical microscopy image of the feature). The Raman signal is strongest in the center and becomes weaker as the mapping is away from the center, which is due to the prism shape morphology. The h-BN signal is essentially zero in the region off the prism where 2D few-layer h-BN is located. Two reasons account for this phenomenon.

First, unlike other 2D materials such as graphene and transition metal dichalcogenides (TMDs), the Raman signal in the h-BN is relatively weak due to the non-resonant character of Raman scattering in h-BN.[43] Second, a laser beam incident normal to a flat metal surface would form a standing wave with a node near the metal surface, namely the transverse electric field is zero according to the boundary conditions. As a result, there is a much weaker Raman scattering in the epitaxial few-layer h-BN film on the proximity of metal surface.[44] Graphene G peak mapping in the same area (Figure 3.6) displays negligible signal, which verifies that carbon atoms have not precipitated at the h-BN/Co interface to form any graphitic structure. The thickness of the thin film is ~1.1 nm, while the height of a prism is measured as ~20 nm by AFM, as shown in Figure 3.4e and 3.4f, respectively. Layered structure is clearly observed from the AFM scan profile across the side wall of a prism. The interlayer distance is measured as 0.35 nm (Figure 3.4g), which agrees with the theoretical interlayer distance of h-BN.[45] A strong peak at 203 nm with a sharp absorption edge can be observed in the absorption spectrum (Figure 3.4h), corresponding to a band gap of 5.93 eV for h-BN extracted from Tauc equation.[30]

Figure 3.5a shows an OM image of Sample B5 transferred onto SiO_2/Si under an incomplete etching condition. The etched sample consists of two regions separated by the dashed line. The Co substrate in region A is completely etched as it is close to the sample edge where the etching speed is higher. Therefore, the contrast is solely from the h-BN film, which is confirmed by the Raman spectrum shown in Figure 3.5b. On the other hand, region B is not etched completely due to a slower etching of the part, which is farther away from the edge. Network-like residue can be observed. Raman spectrum acquired from this region is shown in Figure 3.5b as red curve. Two broad peaks located at ~1400 cm^{-1} and ~1590 cm^{-1} can be assigned to the D, and G peak of amorphous carbon (α-C), respectively.[45] This can be rationalized by the precipitation of carbon atoms on Co grain boundaries to form α-C during substrate cooling. During the carburization process at high temperature, carbon atoms first dissolve into Co following the dehydrogenation of acetylene, and appear as interstitial atoms. During the slow cooling process (10 °C/min)

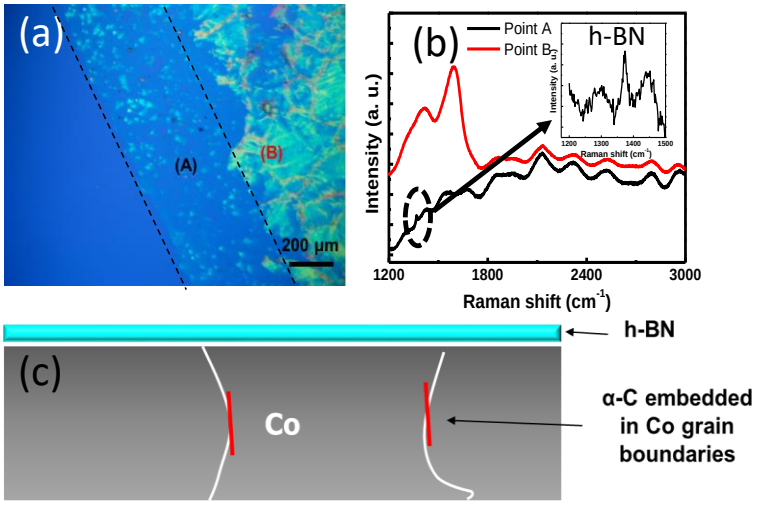

Figure 3.5 H-BN sample grown with 60-s carburization and for 180 minutes (Sample B5) transferred onto SiO_2/Si substrate under incomplete etching. (a) OM image. (b) Raman spectrum from region A (black) and region B (red) in (a). Inset shows a zoom-in spectrum around h-BN peak. (c) Schematic of h-BN sample from a cross-sectional view.

after growth, carbon precipitates preferably on the grain boundaries of Co. It is important to note that no carbon-related structure such as graphene exists at the interface between h-BN and Co according to OM image and Raman spectra results, otherwise it would have been transferred onto the SiO_2/Si substrate and detected. This result can be explained as follows: the carbon solubility in a metal is temperature-dependent, i.e., it is lower when the metal substrate temperature is lower. The precipitation formation of graphene on the surface of a metal occurs when the temperature of a carbon-saturated metal further decreases. The graphene layers continue to build up until the substrate temperature reaches a critical point at which the C atoms no longer have enough energy to form graphene. In the Co metal case, this temperature is on the order of 700 ºC, below which carbon atoms continue to precipitate to form α-C only.[33,46] For the present sample, the carburization process is insufficient, leading to low carbon concentration in Co, which is not only much lower than its saturation level at 900 °C but also not enough to saturate Co at 700 ºC. In addition, Co has a low carbon diffusion coefficient although it has a relatively high C

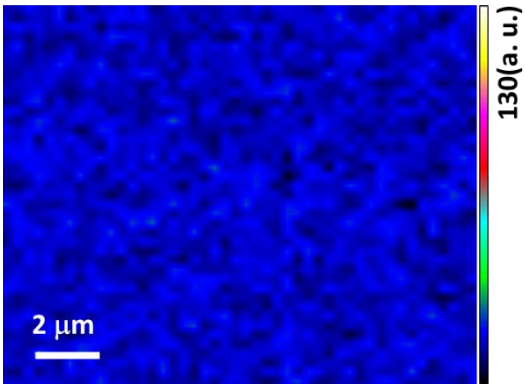

Figure 3.6 Raman mapping at graphene G peak of Sample B5 on the same area as in Figure 3.4d.

solubility.[42] When the cooling is slow, carbon atoms can take advantage of sufficient time to diffuse further into the bulk. As a result, it is more difficult for near-surface C atoms to exceed the solubility limit and nucleate graphene on the surface. These further diffused carbon atoms have ample opportunity to precipitate onto grain boundaries nearby to form α-C as the temperature continues to cool below 700 ºC. After the etchant selectively etches away Co, the embedded α-C network is revealed (Figure 3.5c). Under a careful engineering of the ratio between $FeCl_3$ and HCl in the etchant, all metal can be etched away.

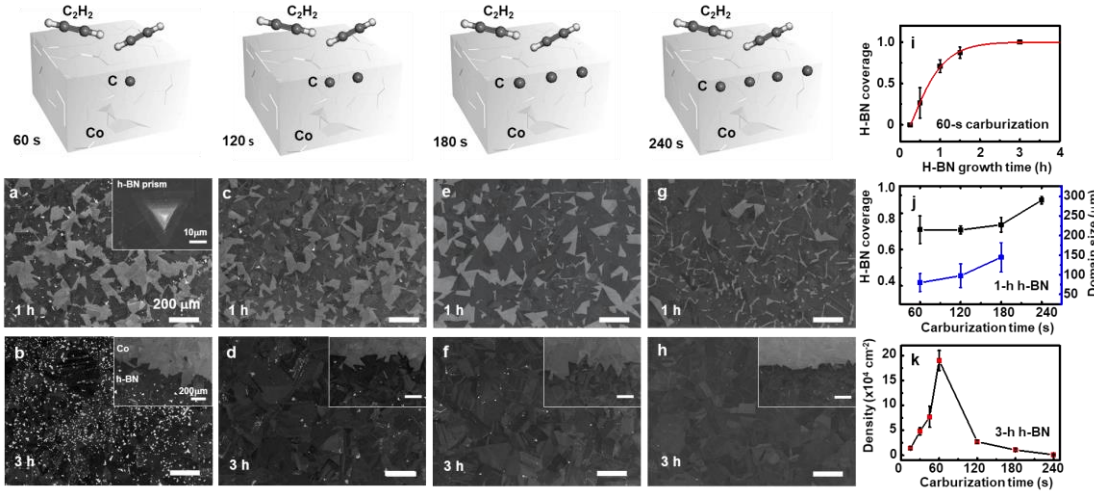

Figure 3.7 Morphology evolution of h-BN as a function of carburization time. Schematic shows that carbon concentration is controlled by carburization process duration. (a-h) Large-area SEM images of (a, c, e, g) 1-hour h-BN samples (C1, 2, 3, 4) and (b, d, f, h) 3-hour h-BN samples (D4, 5, 6, 7) on Co substrate carburized for 60, 120, 180, and 240 s, respectively. Inset in (a) shows a typical "prism" shaped adlayer. Insets in (b, d, f, h) show the edge area for contrast. (i) Plot of h-BN fractional coverage as a function of h-BN growth time with carburization time fixed at 60 s, fitted with the JMAK model in red. (j) Plot of fractional coverage and domain size of 1-h h-BN samples as a function of carburization time from 60 to 240 s. (k) Density of prism-shaped island in the 3-h h-BN samples as a function of carburization time. The scale bar in (a) inset is 10 μm and all others are 200 μm.

Figure 3.6 shows Raman mapping of graphene G peak of Sample B5 in the same area as shown in Figure 3.4d. Unlike h-BN, Raman signals of graphene or graphitic structure on metal can be easily detected. However, the present mapping shows the same intensity as the background in Figure 3.4d. Together with the spectrum shown in Figure 3.4c, in which only h-BN signal is detected, one can conclude that no graphene or graphitic structure exists on the surface of Co substrate.

Figure 3.7a-h show SEM images of h-BN samples grown for 1 h (Samples C1-C4) and 3 h (Samples D4-D7) on Co carburized from 60 to 240 s, respectively. The cartoons on top of SEM images indicate relative interstitial carbon concentration in the substrates of these samples, respectively. As seen from Figure 3.7a and b, high-density bright prism-shaped h-BN multi-layer features are formed on these 60-s carburized samples grown for 1 h and 3 h, respectively. Inset SEM image in Figure 3.7a shows a typical prism-shaped multilayer h-BN island, which appears as a bright feature in the SEM image due to the charging effect. Inset SEM image of the edge area of the sample in Figure 3.7b infers that the 3-h growth led to continuous h-BN 2D film, in contrast to partial 2D h-BN coverage in

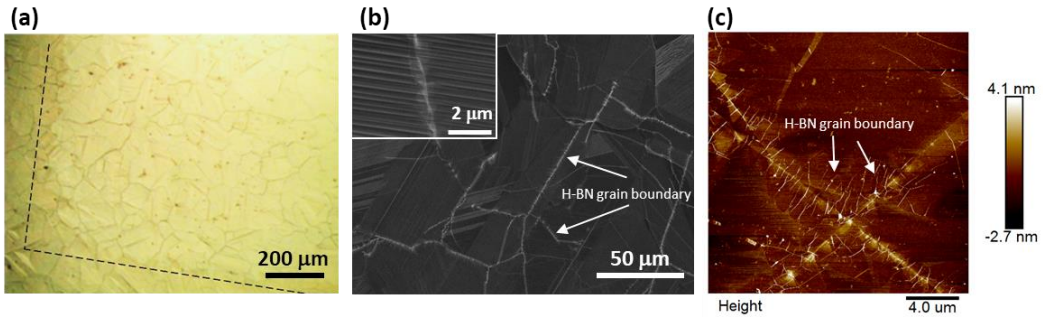

Figure 3.6 (a) Optical microscope image of as-grown continuous h-BN sample (Sample D5), (b) large-area SEM image of continuous film (Sample D7). (c) AFM image of transfer sample at the grain boundary area. The arrows point out the grain boundaries. The inset shows the detail of a grain boundary.

the 1-h h-BN sample, as shown in Figure 3.7a. The exposed Co area appears to be brighter due to less secondary electrons generated from h-BN/Co than from Co.[47] Additional evidence for the continuous nature of a 3-h h-BN film on Co substrate is shown in Figure 3.8. By fixing the Co carburization time at 60 s, additional samples (Samples B1-B5) with other h-BN growth time were grown and Figure 3.9a-e show SEM images of these samples. Only sparse h-BN nuclei emerge on the surface of a 15-min h-BN growth sample (Figure 3.9a), which suggests the time to form stable nuclei (incubation time) is around 15 minutes. Nucleation density increases rapidly in the next 15-minute growth following the incubation period (Figure 3.9b). After certain surface coverage, the size of most h-BN domains continues to increase as incoming ad-atoms are more likely to be captured by existing h-BN flake edges and Ostwald ripening process also plays a dominating role (Figure 3.9c, d). The Co surface is almost fully covered after 90 minutes of growth. Besides the lateral growth, prism-shaped ad-layers along the vertical direction are also formed favorably on the surface irregularities or defective sites. The density of these prisms increases as the growth time increases. After 3-hour growth, high-density 3D prism-shaped islands are formed on the continuous 2D layers (Figure 3.7b and Figure 3.9e). Detailed SEM, AFM, Raman, absorption characterizations of the sample under a 60-s carburization and a 3-hr h-BN growth show that the 2D h-BN film has a thickness of ~1 nm and the size of some prisms is ~10 μm in edge length and ~20 nm in height (Figure 3.4).

The lateral growth is further studied under the framework of Johnson-Mehl-Avrami-Kolmogorov (JMAK) model. Figure 3.7i plots the h-BN coverage versus its growth time.

H-BN coverage on Co was obtained by using ImageJ software, and can be fitted by an exponential curve according to the JMAK model:[48,49]

$$A_{BN} = 1 - \exp(k(t - t_0)^n) \qquad (1)$$

where A_{BN} is the h-BN fractional coverage, k is the rate constant, which depends on

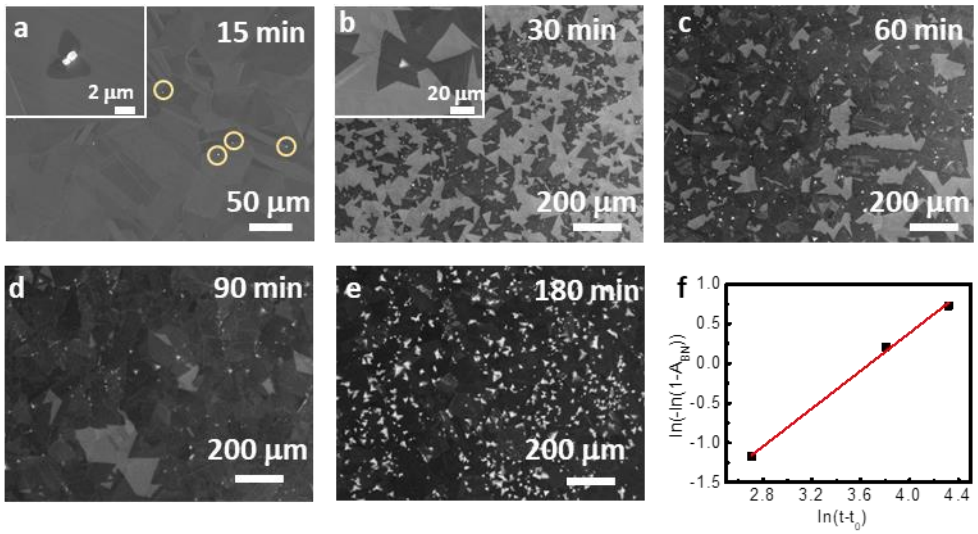

Figure 3.7 H-BN time dependent growth with 60-s carburization of Co (Samples B1-B5). (a-e) SEM images of h-BN samples grown for 15, 30, 60, 90, and 180 minutes, respectively. Yellow circle in (a) indicates small nuclei of h-BN. The inset shows an enlarged image of an individual h-BN nucleus. SEM images in (c) and (e) are from the same samples shown in Figure 3.9a and Figure 3.9b, respectively. (f) the same data in Figure 3.9i plotted in terms of Avrami coordinates, ln(-ln(1-A)) vs ln(t).

both the nucleation rate and domain growth rate. The index n is the Avrami exponent, which is related to the dimensionality of the system and time-dependent nucleation and growth rate. It can be expressed as n = qd+B, where q equals 1 for linear growth (reaction controlled) or 1/2 for parabolic growth (diffusion controlled), and d stands for the dimensionality of the growth; B is 0 for site-saturated nucleation and 1 for continuous nucleation with constant rate. Figure 3.9f shows the same data in Figure 3.7f but is plotted

using Avrami coordinates. A linear relationship is seen. The extracted Avrami exponent is $n = 1.20 \pm 0.05$, suggesting a 2D site-saturated nucleation.[49] It is worth noting that the JMAK model is based on the assumption of constant nucleation rate or a fixed number of nucleation sites, circular domain geometry, and constant, isotropic radial growth velocity.[50] Some modifications to the original JMAK model were done to apply to anisotropic radial growth[51,52]. Based on the fact that the present experimental data fit well with Eq. (1), it is reasonable to apply this model for the growth of h-BN, which does not grow isotropically.

With the change of carburization time from 60 to 240 s, the morphology of h-BN films grown for the same growth time of 1 h is evidently different as shown in Figure 3.7 a, c, e, and g. H-BN flakes appear as dark features and increase in size and coverage as the carburization time increases. Figure 3.7j shows the average h-BN domain size and h-BN fractional coverage as a function of carburization time for these 1-h h-BN samples. The domain size increases from ~80 to ~144 μm as the carburization time increases from 60 to 180 s. For the sample with a 240-s carburization time (Figure 3.7g), h-BN domains coalesce

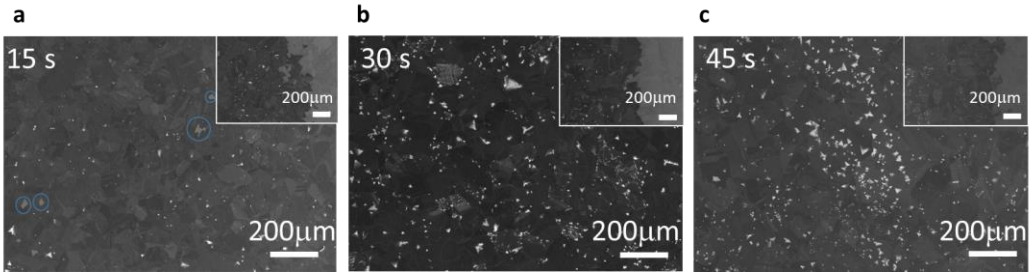

Figure 3.8. **Additional SEM images of 180-mins h-BN samples.** (a-c) SEM image of samples (Samples D1-D3) with (a) 15-, (b) 40- and (c) 45-s carburization time, respectively. H-BN pinholes are circled in blue in (a). Insets show the edge area for contrast.

and almost fully cover the Co surface. This implies that lateral growth rate increases as the increase of the carburization time.

As the h-BN growth time is extended to 3 h, the entire Co surface of all samples with different carburization time (Samples D1-D7) is covered by continuous 2D h-BN films, as seen from the SEM images in Figure 3.7b, d, f, h and Figure 3.10. Additional 3D h-BN prism-shaped islands are also formed on top of the 2D layers in some of these samples, which are clearly dependent on the carburization time. Figure 3.7k shows the density of h-BN prisms as a function of carburization time. The density of h-BN prisms decreases from

1.9×10^5 cm^{-2} to roughly zero as the Co carburization time increases from 60 to 240 s. In

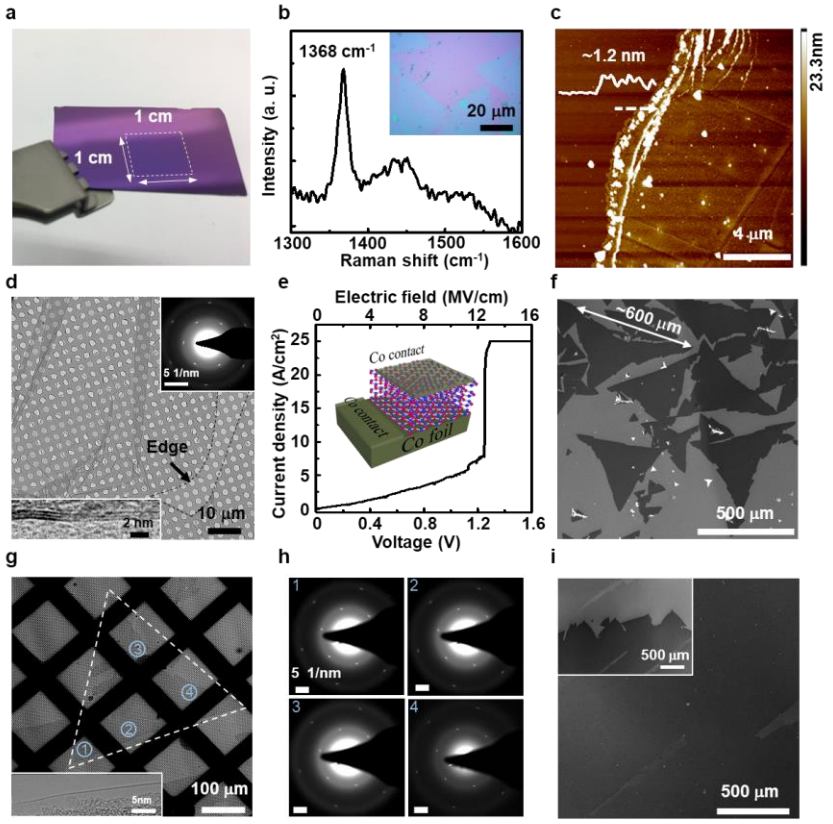

Figure 3.9 Characterization of large-area h-BN 2D layers. (a-e) show results of an h-BN sample grown on carburized Co substrate (Sample D7) and (f-h) show results of of h-BN samples grown on carburized Ni substrates. (a) photograph of the h-BN sample transferred onto SiO_2/Si substrate showing the uniform film with a size of 1cm × 1cm limited by substrate holder. (b) Raman spectrum measured on the transferred h-BN few-layers on SiO_2/Si. The inset displays optical microscope image of the corresponding sample. (c) AFM image scanning across the sample edge. (d) plane-view TEM image of h-BN sample transferred onto a holey carbon film coated copper grid, with SAED pattern shown in the top right corner inset and TEM image at the edge of the h-BN sample in the bottom left corner inset. (e) plot of current density as a function of voltage and electric field of a Co(foil)/h-BN/Co(contact) two-terminal device with the inset displaying a schematic of the device structure. (f) SEM image of an h-BN sample grown on 180-s carburized Ni substrate (Sample E1). Single-crystal h-BN flakes with a typical edge length up to ~600 μm are shown. (g) plane-view TEM image of one such flake of Sample E1 transferred onto a copper grid coated with holey carbon film with the inset displaying a TEM image at the edge of the flake. (h) SAED pattern at 4 different locations across the h-BN flake in g indicated by 1-4. (i) SEM image of an h-BN sample grown on 300-s carburized Ni substrate (Sample E2) with the SEM image of the edge area of the sample in the inset, demonstrating large-area continuous uniform 2D h-BN film on carburized Ni.

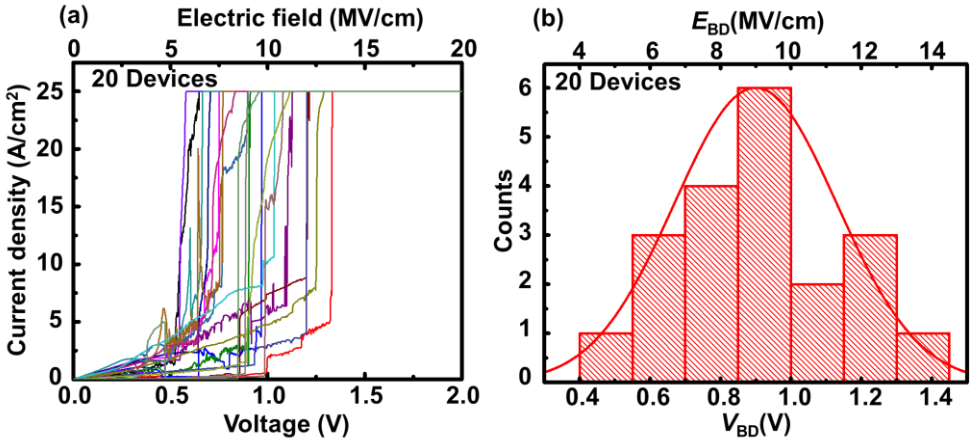

Figure 3.10 (a) Current-voltage characteristics of 20 Co/h-BN/Co devices and (b) the corresponding statistics of breakdown voltage (V_{BD}) and breakdown electric field (E_{BD})

contrast, the density of prisms increases gradually for shorter carburization time from 15 to 60 s. As discussed later, the incorporation of interstitial carbon in Co essentially enables the nucleation and growth of h-BN. As interstitial carbon content is low in these samples with the carburization time less than 60 s, the adsorption of both B and N atoms is weak, the nucleation mainly relies on defects and imperfection sites on the surface, which facilitates vertical growth of prisms. As interstitial carbon content increases in the samples with carburization time larger than 60 s, the abundance of B and N atoms on the surface as a result of the enhanced adsorption facilitates the nucleation of h-BN domains. As shown later, the diffusion of these atoms is also enhanced as a result of carbon interstitial effect. These factors are responsible for an increased lateral growth rate and domain size, thus prism-like island formation is further suppressed, leading to the dominant growth of 2D layers.

Figure 3.11a shows a photograph of a homogeneous few-layer h-BN sample (Sample D7). Figure 3.11b shows Raman spectrum of the transferred sample showing a sharp E_{2g} phonon mode at 1368 cm^{-1} and a FWHM of ~16 cm^{-1}. The inset shows an optical microscopy image of the transferred film onto a SiO_2/Si substrate, indicating large-area uniform film. Figure 3.11c shows an AFM image of the transferred film with a scan profile across a flake edge in the inset. The thickness of the h-BN film can be estimated as ~1.2 nm despite of undulating signals in the scan profile due to residual PMMA contamination

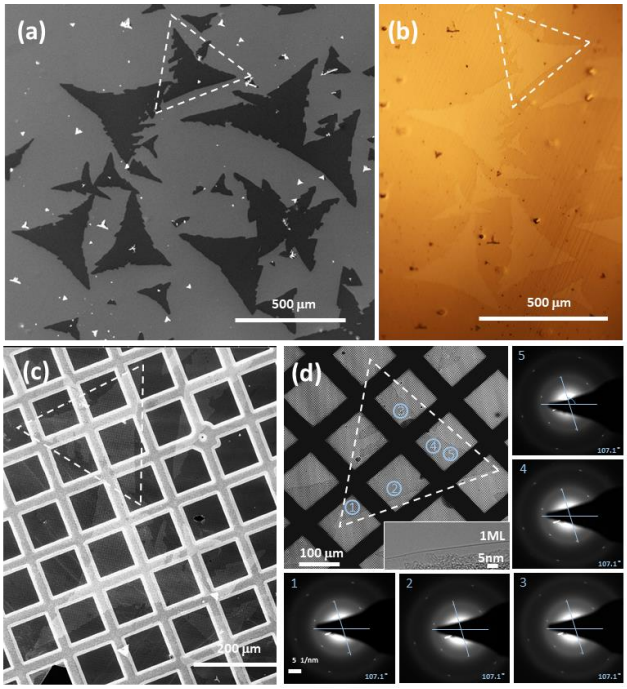

Figure 3.11 Additional information of TEM measurement of Sample E1. The same examined flake is circled out with white dashed line before and after transfer. (a,b) SEM and OM image of Sample E1 before transferring onto TEM grid, respectively. The OM image is obtained after baking the sample in air to create contrast using a similar approach described in Section 12. (c) SEM image of Sample E1 after transferring onto TEM grid. (d) TEM SAED mapping with plain-view TEM image. SAED patterns were collected from 5 arbitrary location on the flake, as circled in the plain-view TEM image. The diameter of blue circle represents the real size of SA aperture. The inset shows the edge analysis of monolayer h-BN.

from transferring process. Figure 3.11d shows a plane-view TEM image of the h-BN film transferred onto a holey carbon grid and the top right inset is its corresponding 4-spot SAED pattern, indicating high crystallinity. Further TEM analysis of the film edge in the bottom left inset shows that the film consists of three layers.

Figure 3.11e shows current density versus voltage/electric field (J-V/E) of a Co(metal contact)/h-BN/Co(foil) two-terminal device with a metal contact size of 200×200 μm^2

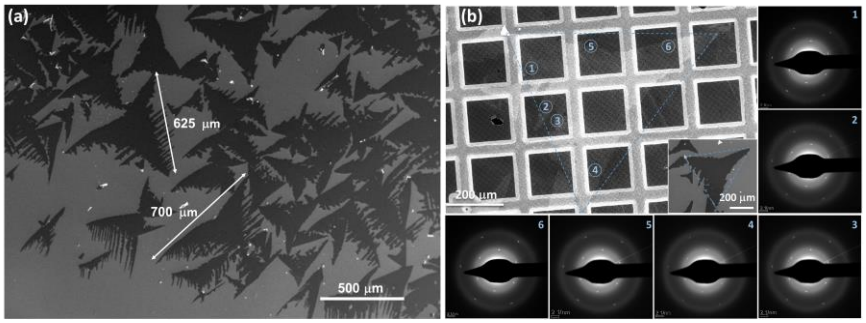

Figure 3.12 (a) Additional SEM image of the same sample (Sample E1) presented in Figure 3.11f at edge area. (b) TEM SAED mapping with corresponding SEM image of a typical dendritic h-BN flake.

based on a 240-s carburized h-BN sample (Sample D7). The thickness of the 2D h-BN is considered as ~1 nm according to the observation of a 3-layer film by TEM imaging (AFM result gives a slightly larger thickness of ~1.2 nm due to tip effect). The J-V characteristic clearly exhibits a quasi-linear relationship at the low and moderate voltage regions due to direct tunneling[53]and a dielectric breakdown. Statistical study of J-V characteristics of 20 devices in Figure 3.12 leads to an average breakdown electric field of 9 MV/cm. This number is three times as large as that of our earlier devices based on h-BN films without carburization,[31] and is comparable to those of exfoliated h-BN layers by high-

temperature high-pressure method,[54] suggesting significantly improved quality of the h-BN here.

The concept of carbon interstitial assisted growth of h-BN applies to other transition metal substrates. To avoid redundancy, we briefly show some results on carburized Ni substrates. Figure 3.11f shows SEM image of a 6-h h-BN sample grown on a 180-s carburized Ni substrate (Sample E1). Discrete h-BN single-crystalline domains with an edge length of ~600 μm are evident, which are among the largest h-BN flakes ever reported.[16] The flakes grown near the edge of the substrate show even larger size of ~700 μm in edge length (Figure 3.14). The single-crystallinity is confirmed by recording SAED patterns at different locations across the h-BN domain, which are identical (Figs. 2g&h). Additional information of TEM measurements showing the h-BN domain before and after transferring onto a TEM grid as well as additional SAED patterns at different spots can be found in Figure 3.13 & 3.14. TEM imaging also reveals that the large h-BN domain is monolayer (Figure 3.11g). A large-area continuous uniform 2D h-BN film (Sample E2) was also achieved by the same 6-h h-BN growth on a Ni substrate with an increased carburization time of 300 s, as shown in the SEM image and inset of Figure 3.11h. To further confirm continuous nature and thickness uniformity of the large-area h-BN film, large-area OM images together with large-area Raman mapping across a 1 cm × 1 cm area

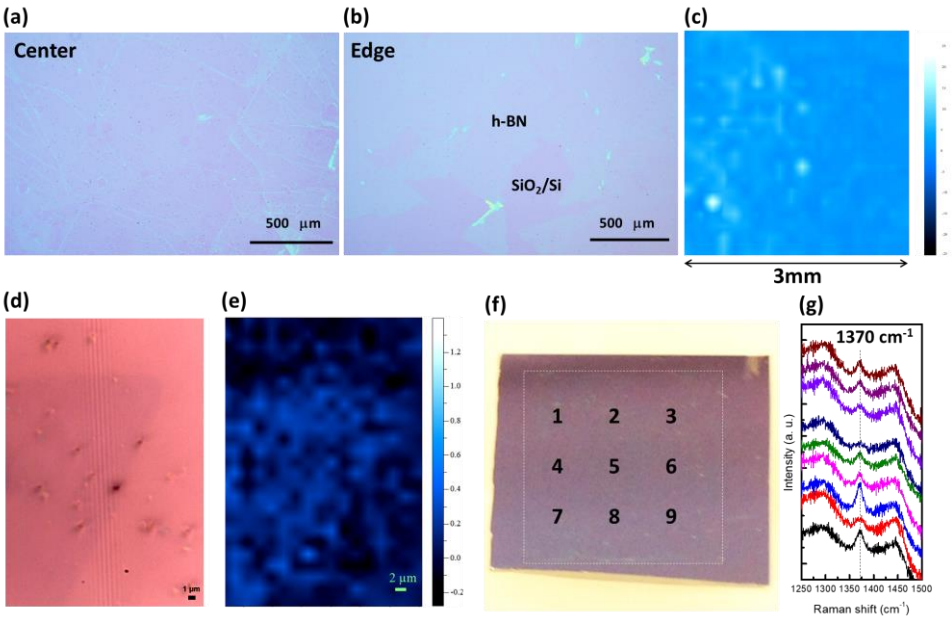

Figure 3.13 Raman mapping analysis of h-BN sample transferred onto SiO_2/Si substrate (Sample E2) (a) & (b) Low-magnification optical microscope images of the sample at center and edge, respectively. (c) Raman mapping of the h-BN characteristic peak of a 3×3 mm^2 area across the center area of the sample. (d) Higher-magnification optical microscope image of a typical h-BN triangle edge and (e) corresponding Raman mapping result. (f) Photograph of the sample with an area of 1 cm × 1 cm (g) Overlaying of Raman spectra taken at point 1-9 in (f) from bottom to top.

of the h-BN sample transferred on to a SiO_2/Si substrate are shown in Figure 3.15. Figure 3.16a and b show B1s, and N1s XPS spectra of h-BN samples C1, C2, C3, and C4 which were grown for 1 hour with carburization time from 60 to 240 s, respectively. The B1s (N1s) peak can be fitted into two peaks at slightly different binding energy (BE), with a dominant peak at a lower BE of 190.1(397.6) eV as well as a small peak at a higher BE of 190.7(398.2) eV. The difference between the lower-BE and higher-BE peaks of the B1s/N1s peaks is ~0.6/0.6 eV, which is consistent with the reported values of 0.6 eV for B and 0.5 eV for N. [55]The dominant lower-BE peak can be assigned to sp^2 B-N bond for hexagonal phase BN, and the higher-BE peak can be assigned to local cubic-like sp^3

bonds.[55-59] As seen from Figure 3.16a and b, the intensity of the 190.7(398.2) eV pair is the largest in 60-s carburized sample. As the carburization time increases from 60 s to 240 s, the intensity of the high-BE peak decreases. This result suggests the decrease of sp^3 bonds as the increase of the carburization time. Complementarily, the intensity of the lower BE pair (sp^2 bond phase) is inversely correlated to the prism density of each sample. This

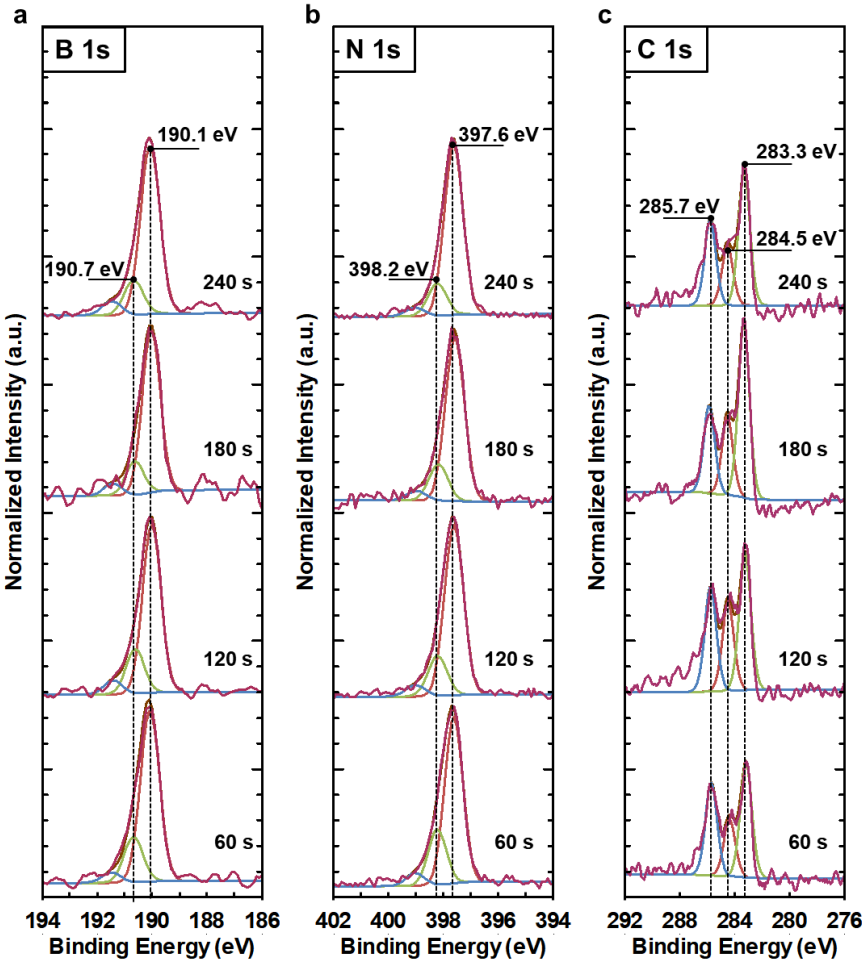

Figure 3.14 XPS of 1-h h-BN samples with different carburization time. (a-c) XPS spectra of surface resolved (a) B1s, (b) N1s, and (c) subsurface C1s after removal of h-BN layer and surface contamination by 60-second Ar ion sputtering of the h-BN samples with 60-, 120-, 180- and 240-s carburization time from bottom to top. a & b are plotted with normalized range. c is normalized at the background of each spectrum.

implies that the sp^3 bonds possibly exist in the prisms, seeding the vertical growth of multilayer prism-shaped islands, in particular in the low-carburized samples. The increase of interstitial carbon suppresses the formation of sp^3 type of bonds and promotes the lateral growth of h-BN layers in higher-carburized samples. The stoichiometry of these as-grown films were calculated to have a B:N ratio between 1.05:1 and 1:1.06, which are essentially ~1:1 within the experimental error of the XPS sensitivity factors and peak fitting.

Figure 3.16c shows XPS C1s spectra of samples C1, C2, C3, and C4 after 60-s Ar ion sputtering. This sputtering was used to completely remove h-BN layers and surface carbon contamination. Discussion on the depth-resolved XPS of the 240-s carburized sample is

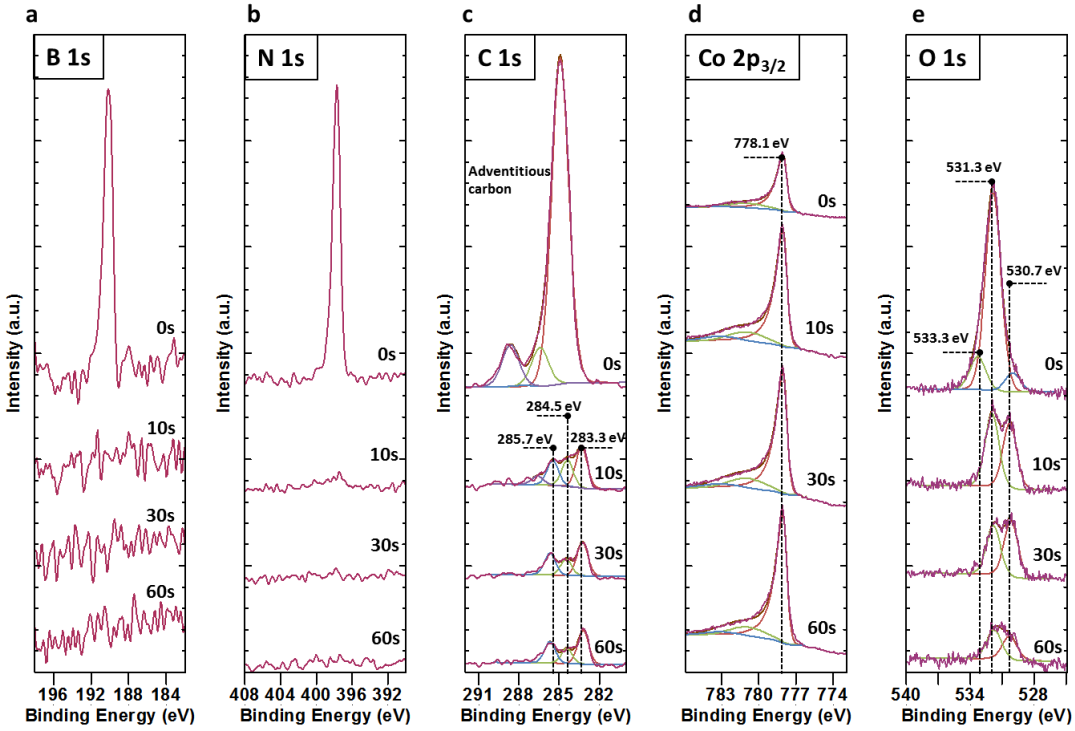

Figure 3.15 XPS depth profiling of h-BN sample with 240-s carburization. (a-e) B1s (a), N1s (b), C1s (c), Co $2p_{3/2}$ (d), O1s (e) peaks with 0- 10- 30- 60-s sputtering under 3-keV Ar ion from top to bottom, respectively.

detailed as an example in Figure 3.17. To evaluate the near-surface carbon information using XPS experiment, the key is to remove the adventitious carbon as well as h-BN layers on the surface. From Figs. 17a&b it is evident that after 10-s sputtering, majority of both B 1s and N 1s peaks are removed, while only a small peak of N 1s remains due to the high relative sensitivity factor of N 1s. After 60-s sputtering, no h-BN related signals can be detected on the surface. The surface C 1s spectrum shows typical peaks of adventitious carbon with the main peak at 284.9 eV (Figure 3.17c). All major peaks are removed after 10-s sputtering. A new peak emerges at 283.3 eV as the main peak, which can be assigned to interstitial carbon or carbide. The peaks at 284.5 eV and 285.7 eV are assigned to C-C bond as in α-C, and CO absorbed on surface, respectively. Co $2p_{3/2}$ signals show a dominate peak at 778.1 eV, which is used for binding energy calibration (Figure 3.17d). The surface O 1s intensity reduces significantly after 10-s sputtering due to the fact that surface organic compound and water are removed. Then the near surface O 1s can be fitted by two peaks at 531.3 eV as the C-O peak in CO and 530.7 eV as CoO peak (Figure 3.17e).

As seen from Figure 3.16c, a major peak at 283.3 eV is close to the assignment for interstitial carbon or carbide,[60-62] which indicates the presence of interstitial carbon atoms in the Co substrates. Compared with the XPS spectra of a reference pristine Co substrate and a pristine Co annealed at a temperature of 900 °C in H_2 environment for 1 h (Figure 3.18), the increase of interstitial carbon atoms as a result of increased carburization is evident. However, it is noted that these results are collected at room temperature, under which Co has very low solubility of carbon, and the excessive carbon atoms over the solubility level would precipitate as α-C in between Co grains (Figure 3.5). As a matter of

fact, the solubility for carbon at the growth temperature is much higher, ~1.5 at.% at 900 ºC,[63] especially at subsurface[64-66], which will impact the growth mostly. Thus, with different C_2H_2 flux rate and treatment time, the interstitial carbon concentration can vary between 0 and 1.5 at% in different samples at the growth temperature, leading to different morphology of the synthesized films. The peak at 284.5 eV can be assigned to C-C bond,[45] which is possibly originated from α-C structure embedded in Co grain boundaries (Figure 3.5). B-C[67], N-C[68] bonds are not detected in B 1s, N 1s and C 1s spectra, which confirms the formation of h-BN without C incorporation or contamination.

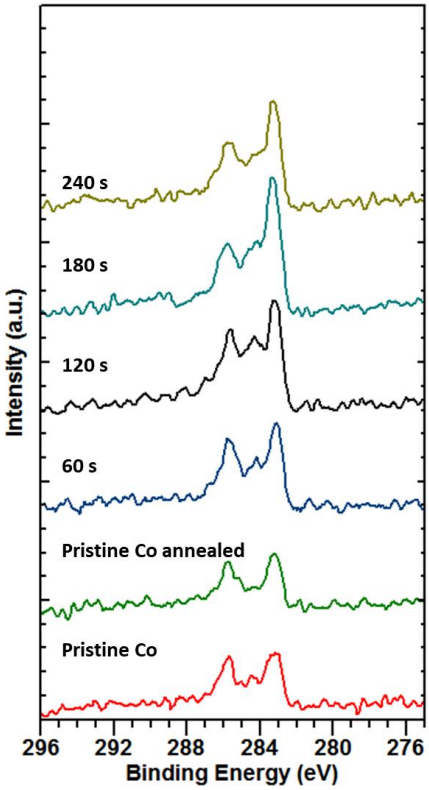

Figure 3.16 XPS spectra of C1s of several h-BN samples, a pristine Co substrate, and a Co substrate annealed in H_2 for 1 h. The h-BN samples were grown for 1 hr on carburized Co with 60-, 120-, 180- and 240-s carburization time from bottom to top. All surfaces were treated by 60-s Ar ion sputtering to remove surface layers and any contaminants prior to the measurements.

To understand the effect of Co and carburized Co on the growth of h-BN at the molecular level, ab-initio DFT simulations were performed. The surface energy of the substrate σ is defined as[69-71]

$$\sigma = \frac{[E_{slab} - \sum N_i \mu_i]}{2A} \quad (2)$$

where E_{slab} is the total energy of the substrate calculated from first principles, μ_i is the chemical potential of species *i* in the slab structure, N_i is the number of particles of the *i*-th element in the slab, and A is the area of the slab. The DFT calculations show that the Co (111) surface has a surface energy of 2037.87 mJ/m^2, compared to that of Cu (111), which is 1231.08 mJ/m^2. Cu (111) is used as a reference since h-BN can be grown on it.[2,10,11] The higher surface energy of Co (111) suggests better wettability of Co (111) as substrate.

The adsorption energy of B and N atoms on the Co substrate is calculated from the difference in total energies,

$$E_{ads} = E_{B/N} + E_{surface} - E_{B/N\ on\ surface} \quad (3)$$

where $E_{B/N\,on\,surface}$ is the total energy of the adsorbed system, in which a boron or nitrogen atom is adsorbed on the Co (111) surface. $E_{B/N}$ is the chemical potential of the adsorbed B or N atom and $E_{surface}$ is the energy of the Co (111) surface. A larger adsorption energy indicates stronger adsorption of an atom onto a surface and a positive adsorption energy corresponds to stable adsorption. Figure 3.19 summarizes the DFT calculated adsorption energies of B and N atoms on Co (111) with and without embedded interstitial

carbon and on Cu (111) substrates. Top-view and side-view schematic of the atomic positions is shown in Figure 3.19a-d. Positions to hold either B or N atoms include those directly above the hexagonally aligned Co (or Cu) atoms, and the six voids within the Co (or Cu) hexagon, three of them designated as Face Centered Cubic (FCC) sites and the other three designated as Hexagonal Closely Packed (HCP) sites. On the Cu (111) surface, the adsorption energy of B and N are small and negative for all sites. Negative adsorption energies for B and N on the Cu (111) surface suggest that h- BN should not be formed on Cu (111) unless the growth is triggered through other mechanism. The experimental demonstration of the growth of h-BN on Cu (111) was explained by the presence of preferential nucleation sites, for examples, atomic steps and defects, including extended defects such as grain boundaries and point defects.[69-71] On the Co (111) surface, as seen from Figure 3.19e, the adsorption energies of B and N on the three sites are significantly higher compared to Cu (111) surface. In addition, the adsorption energies of N on both the HCP and FCC sites of the Co surface are positive, suggesting enhanced adsorption of N atoms onto these sites of the substrate. The above comparison between Co and Cu substrates indicates that h-BN would be more likely to grow on Co under certain conditions such as at a relatively low growth temperature assuming both substrates are free of surface irregularities as preferential nucleation sites.

As the growth temperature is raised to a certain point such as 900 ºC in this case, the desorption rates of both B and N atoms on Co (111) surface become higher, leading to zero growth as shown earlier. The central theme of this work is to enable the growth of h-BN at these conditions by enhancing the adsorption and diffusion of B and N atoms on Co (111) using carbon interstitials in the substrate. In the XPS studies in Figure 3.16, we have shown the existence of interstitial carbon in Co. It was also reported that the octahedral sites in Co

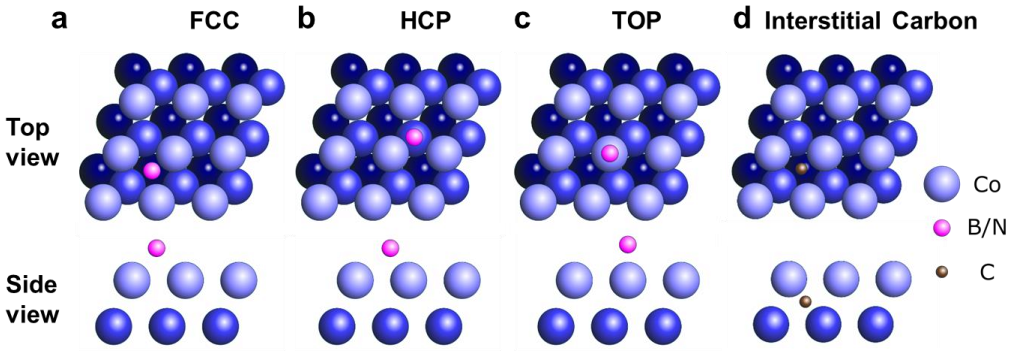

e

Adsorption Energy eV/atom	Boron			Nitrogen		
	FCC	HCP	Top	FCC	HCP	Top
Cu(111)	-1.74	-1.71	-3.26	-1.11	-1.19	-3.22
Co(111)	-0.80	-0.69	-2.23	0.26	0.50	-1.80
Co(111) With interstitial carbon	-0.522	-0.081	Not stable	0.298	1.062	Not stable

Figure 3.17 DFT calculation results of adsorption energies of B and N on Co (111) with and without embedded interstitial carbon. (a-d), Top-view and side-view schematic of (a) B/N atoms on FCC sites, (b) B/N atoms on HCP sites, (c) B/N atoms on top of substrate atoms, and (d) interstitial carbon on an octahedral site of the substrate. (e) A summary of adsorption energies of B and N on a reference Cu (111) substrate and on Co (111) substrates with and without embedded interstitial carbon.

(111) are the most stable sites for interstitial carbon.[72] Thus, with the assumption of an interstitial carbon at the octahedral site in a supercell of Co (111), which is 0.6 Å below the surface, adsorption energies of different sites for B and N were calculated using the

same DFT calculation method summarized in the Experimental details section. As seen from Figure 3.19e, except for the top site where both B and N are pushed away and hence can be considered unstable, the adsorption energies of B and N are further increased for HCP and FCC sites compared to no interstitial carbon. In particular, both B and N atoms prefer to adsorb at the HCP sites with the highest adsorption energy of -0.08, and 1.06 eV/atom, respectively.

From the above experiment and simulation results, we can rationalize the growth control from the perspective of adsorption energy. According to the framework of Robinson and Robins model regarding nucleation[49, 73], when nucleation is limited by the desorption of surface adatoms, the saturation nucleation density N_s can be expressed as:

$$N_s \propto N_{s0} \exp(-\frac{E_a}{2kT}) \qquad (2)$$

where $E_a = E_{diff} - E_{ads} - E_{att}$ is the nucleation activation energy, and it is related to the adsorption energy E_{ads}, diffusion activation energy E_{diff} and energy barrier of attachment for the capture of a surface adatom by a supercritical nucleus E_{att}. N_{s0} is a pre-exceptional term, which is related to the impinging rate of B/N atoms onto the surface and the density of nucleation sites. As seen from Eq. (2), at a given temperature and source flux, the increase of adsorption energy (E_{ads}) and attachment energy (E_{att}), and reduction of diffusion activation energy (E_{diff}) can promote the nucleation of h-BN. As seen from Figure 3.19, E_{ads} for B and N are 0.609 eV and 0.562 eV higher when interstitial carbon is present, which in turn have enhanced the nucleation of h-BN through Eq. (2).

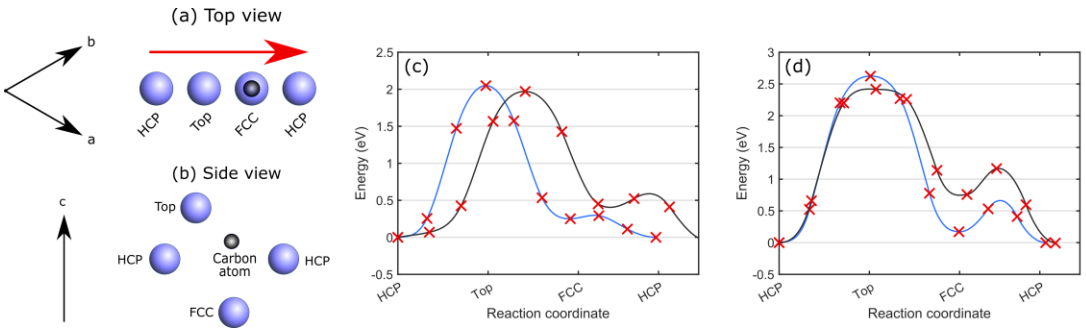

Figure 3.18 Reaction path from an NEB calculation showing the diffusion activation energy from one HCP site to another (a) Top view and (b) side view of a Co (111) surface. Minimum energy path for (c) a boron and (d) a nitrogen atom diffusing from one HCP site to the neighboring HCP site of Co (111) surface without (blue curve) or with (black curve) interstitial carbon atom.

To elaborate the carbon interstitial effect on diffusion activation energy (E_{diff}), simulation using the climbing image nudged elastic band (CI-NEB) method was carried out [38]. As seen from Figure 3.20, E_{diff} is reduced by 0.079 eV and 0.207 eV for B and N atoms, respectively, after the interstitial carbon is present in the substrate, leading to the

increase of nucleation of h-BN as well according to Eq. (2). The carbon interstitial effect on the attachment energy (E_{att}) remains elusive. Hypothetically, the change of E_{att} may not be as significant as the other energy terms since it is largely correlated to the formation energy of B-N bond, which is assumed to be constant.

On pristine Co substrates, low and negative adsorption energy of B atoms on Co surface means a low B atomic sticking coefficient, leading to a low h-BN growth probability and reliability. Higher desorption of both B and N atoms on the Co surface at higher substrate temperatures further reduce the possibility of the growth. The existence of interstitial carbon atoms in Co assists the adsorption and diffusion of B and N atoms on the Co surface, and thus enhances the nucleation of h-BN. As interstitial carbon concentration in Co is low, the h-BN nucleation relies mostly on imperfections such as defects, grain boundaries, and local valleys/protrusions on the surface. This condition results in the formation of both 2D h-BN and 3D prism-shaped islands, as discussed in the XPS analysis. The competition between 2D and 3D growth modes is clearly demonstrated from the effect of the carburization level on the density of prism-shaped islands (Figure 3.7k). On the other hand, as interstitial carbon concentration is high, h-BN nucleation happens uniformly across the surface as a result of abundant B and N atoms on the surface. In addition, an increased mobility of B and N atoms suppresses the vertical growth of 3D islands and promotes the 2D growth of uniform few-layer h-BN films through the preferential nucleation at the edges of growing flakes and Ostwald ripening processes. There is also negligible possibility that the h-BN would have been formed through precipitation growth mode under the current experimental condition.

3.4. **Conclusion**

In conclusion, a new dimension of control in the growth of h-BN by modifying the transition metal substrates via carburization has been achieved. A systematic SEM study of MBE grown h-BN on carburized Co foils is presented to reveal the h-BN nucleation and domain growth, and evolution of morphology as a function of carbon interstitial concentration in Co. The interstitial carbon atoms in Co triggers and enhances the growth of h-BN at the given condition. Further increase of the carbon concentration promotes lateral growth of h-BN few-layers and eliminates the prism-shape island formation. The lateral h-BN growth is fitted with JMAK model. Characterizations were carried out on a few-layer h-BN sample grown on a 240-s C_2H_2 treated Co substrate, revealing that a tri-layer h-BN film with good uniformity in thickness and a breakdown electric field of 9 MV/cm is formed. Single-crystalline h-BN flakes of ~600 μm, and large-area uniform h-BN monolayer were achieved on carburized Ni substrates. The growth mechanism is further studied by DFT calculations. The adsorption and diffusion of both B and N atoms are enhanced by the existence of interstitial carbon atoms in the substrate, resulting in a reliable and controllable growth of 2D h-BN in contrast to no growth on pristine Co. The concept proposed and demonstrated here, namely interstitial-assisted growth of h-BN 2D films not only paves the way of reliable synthesis of high-quality, large-area, uniform 2D h-BN for various applications but also can be applied to advance the synthesis of other 2D crystal materials.

3.5. **References**

[1] Nag, A.; Raidongia, K.; Hembram, K. P.; Datta, R.; Waghmare, U. V.; Rao, C. Graphene Analogues of BN: Novel Synthesis and Properties. *ACS Nano* **2010,** 4, 1539-1544.

[2] Song, L.; Ci, L.; Lu, H.; Sorokin, P. B.; Jin, C.; Ni, J.; Kvashnin, A. G.; Kvashnin, D. G.; Lou, J.; Yakobson, B. I. Large Scale Growth and Characterization of Atomic Hexagonal Boron Nitride Layers. *Nano Lett.* **2010,** 10, 3209-3215.

[3] Watanabe, K.; Taniguchi, T.; Kanda, H. Direct-bandgap Properties and Evidence for Ultraviolet Lasing of Hexagonal Boron Nitride Single Crystal. *Nat. Mater.* **2004,** 3, 404.

[4] Dean, C. R.; Young, A. F.; Meric, I.; Lee, C.; Wang, L.; Sorgenfrei, S.; Watanabe, K.; Taniguchi, T.; Kim, P.; Shepard, K. L. Boron Nitride Substrates for High-Quality Graphene Electronics. *Nat. Nanotech.* **2010,** 5, 722-726.

[5] Britnell, L.; Gorbachev, R.; Jalil, R.; Belle, B.; Schedin, F.; Mishchenko, A.; Georgiou, T.; Katsnelson, M.; Eaves, L.; Morozov, S. Field-Effect Tunneling Transistor Based on Vertical Graphene Heterostructures. *Science* **2012,** 335, 947-950.

[6] Lee, K. H.; Shin, H.-J.; Lee, J.; Lee, I.-y.; Kim, G.-H.; Choi, J.-Y.; Kim, S.-W. Large-Scale Synthesis of High-quality Hexagonal Boron Nitride Nanosheets for Large-area Graphene Electronics. *Nano Lett.* **2012,** 12, 714-718.

[7] Levendorf, M. P.; Kim, C.-J.; Brown, L.; Huang, P. Y.; Havener, R. W.; Muller, D. A.; Park, J. Graphene and Boron Nitride Lateral Heterostructures for Atomically Thin Circuitry. *Nature* **2012,** 488, 627.

[8] Cassabois, G.; Valvin, P.; Gil, B. Hexagonal Boron Nitride is an Indirect Bandgap Semiconductor. *Nat. photonics* **2016,** 10, 262-266.

[9] Kubota, Y.; Watanabe, K.; Tsuda, O.; Taniguchi, T. Deep Ultraviolet Light-Emitting Hexagonal Boron Nitride Synthesized at Atmospheric Pressure. *Science* **2007,** 317, 932-934.

[10] Kim, K. K.; Hsu, A.; Jia, X.; Kim, S. M.; Shi, Y.; Hofmann, M.; Nezich, D.; Rodriguez-Nieva, J. F.; Dresselhaus, M.; Palacios, T. Synthesis of Monolayer Hexagonal Boron Nitride on Cu Foil Using Chemical Vapor Deposition. *Nano Lett.* **2011,** 12, 161-166.

[11] Tay, R. Y.; Park, H. J.; Ryu, G. H.; Tan, D.; Tsang, S. H.; Li, H.; Liu, W.; Teo, E. H. T.; Lee, Z.; Lifshitz, Y. Synthesis of Aligned Symmetrical Multifaceted Monolayer

Hexagonal Boron Nitride Single Crystals on Resolidified Copper. *Nanoscale* **2016,** 8, 2434-2444.

[12] Driver, M. S.; Beatty, J. D.; Olanipekun, O.; Reid, K.; Rath, A.; Voyles, P. M.; Kelber, J. A. Atomic Layer Epitaxy of h-BN (0001) Multilayers on Co (0001) and Molecular Beam Epitaxy Growth of Graphene on h-BN (0001)/Co (0001). *Langmuir* **2016,** 32, (11), 2601-2607.

[13] Kidambi, P. R.; Blume, R.; Kling, J.; Wagner, J. B.; Baehtz, C.; Weatherup, R. S.; Schloegl, R.; Bayer, B. C.; Hofmann, S. In Situ Observations During Chemical Vapor Deposition of Hexagonal Boron Nitride on Polycrystalline Copper. *Chem. Mater.* **2014,** 26, 6380-6392.

[14] Ismach, A.; Chou, H.; Ferrer, D. A.; Wu, Y.; McDonnell, S.; Floresca, H. C.; Covacevich, A.; Pope, C.; Piner, R.; Kim, M. J. Toward the Controlled Synthesis of Hexagonal Boron Nitride Films. *ACS Nano* **2012,** 6, 6378-6385.

[15] Shi, Y.; Hamsen, C.; Jia, X.; Kim, K. K.; Reina, A.; Hofmann, M.; Hsu, A. L.; Zhang, K.; Li, H.; Juang, Z.-Y. Synthesis of Few-Layer Hexagonal Boron Nitride Thin Film by Chemical Vapor Deposition. *Nano Lett.* **2010,** 10, 4134-4139.

[16] Meng, J.; Zhang, X.; Wang, Y.; Yin, Z.; Liu, H.; Xia, J.; Wang, H.; You, J.; Jin, P.; Wang, D. Aligned Growth of Millimeter-Size Hexagonal Boron Nitride Single-Crystal Domains on Epitaxial Nickel Thin Film. *Small* **2017,** 13, 1604179.

[17] Caneva, S.; Weatherup, R. S.; Bayer, B. C.; Brennan, B.; Spencer, S. J.; Mingard, K.; Cabrero-Vilatela, A.; Baehtz, C.; Pollard, A. J.; Hofmann, S. Nucleation control for large, Single Crystalline Domains of Monolayer Hexagonal Boron Nitride via Si-Doped Fe Catalysts. *Nano Lett.* **2015,** 15, 1867-1875.

[18] Kim, S. M.; Hsu, A.; Park, M. H.; Chae, S. H.; Yun, S. J.; Lee, J. S.; Cho, D.-H.; Fang, W.; Lee, C.; Palacios, T. Synthesis of Large-Area Multilayer Hexagonal Boron Nitride for high Material Performance. *Nat. Commun.* **2015,** 6, 8662.

[19] Caneva, S.; Weatherup, R. S.; Bayer, B. C.; Blume, R.; Cabrero-Vilatela, A.; Braeuninger-Weimer, P.; Martin, M.-B.; Wang, R.; Baehtz, C.; Schloegl, R. Controlling Catalyst Bulk Reservoir Effects for Monolayer Hexagonal Boron Nitride CVD. *Nano Lett.* **2016,** 16, (2), 1250-1261.

[20] Sutter, P.; Lahiri, J.; Zahl, P.; Wang, B.; Sutter, E. Scalable Synthesis of Uniform Few-Layer Hexagonal Boron Nitride Dielectric Films. *Nano Lett.* **2012,** 13, 276-281.

[21] Kim, G.; Jang, A.-R.; Jeong, H. Y.; Lee, Z.; Kang, D. J.; Shin, H. S. Growth of High-Crystalline, Single-Layer Hexagonal Boron Nitride on Recyclable Platinum Foil. *Nano Lett.* **2013,** 13, 1834-1839.

[22] Hao, Y.; Bharathi, M.; Wang, L.; Liu, Y.; Chen, H.; Nie, S.; Wang, X.; Chou, H.; Tan, C.; Fallahazad, B. The Role of Surface Oxygen in the Growth of Large Single-Crystal Graphene on Copper. *Science* **2013,** 342, 720-723.

[23] Song, X.; Gao, T.; Nie, Y.; Zhuang, J.; Sun, J.; Ma, D.; Shi, J.; Lin, Y.; Ding, F.; Zhang, Y. Seed-Assisted Growth of Single-Crystalline Patterned Graphene Domains on Hexagonal Boron Nitride by Chemical Vapor Deposition. *Nano Lett.* **2016,** 16, 6109-6116.

[24] Ismach, A.; Mende, P.; Dolocan, A.; Addou, R.; Aloni, S.; Wallace, R.; Feenstra, R.; Ruoff, R.; Colombo, L. Carbon-Assisted Chemical Vapor Deposition of Hexagonal Boron Nitride. *2D Mater.,* **2017***,* 4, 025117.

[25] Zheng, R.; Xu, Z.; Khanaki, A.; Tian, H.; Zuo, Z.; Zheng, J.-G.; Liu, J. Low-Temperature Growth of Graphene on Iron Substrate by Molecular Beam Epitaxy. *Thin Solid Films* **2017,** 627, 39-43.

[26] Cho, Y.-J.; Summerfield, A.; Davies, A.; Cheng, T. S.; Smith, E. F.; Mellor, C. J.; Khlobystov, A. N.; Foxon, C. T.; Eaves, L.; Beton, P. H. Hexagonal Boron Nitride Tunnel Barriers Grown on Graphite by High Temperature Molecular Beam Epitaxy. *Sci. Rep.* **2016,** 6, 34474.

[27] Summerfield, A.; Davies, A.; Cheng, T. S.; Korolkov, V. V.; Cho, Y.; Mellor, C. J.; Foxon, C. T.; Khlobystov, A. N.; Watanabe, K.; Taniguchi, T. Strain-Engineered Graphene Grown on Hexagonal Boron Nitride by Molecular Beam Epitaxy. *Sci. Rep.* **2016,** 6, 22440.

[28] Nakhaie, S.; Wofford, J.; Schumann, T.; Jahn, U.; Ramsteiner, M.; Hanke, M.; Lopes, J.; Riechert, H. Synthesis of Atomically Thin Hexagonal Boron Nitride Films on Nickel Foils by Molecular Beam Epitaxy. *Appl. Phys. Lett.* **2015,** 106, (21), 213108.

[29] Wofford, J. M.; Nakhaie, S.; Krause, T.; Liu, X.; Ramsteiner, M.; Hanke, M.; Riechert, H.; Lopes, J. M. J. A hybrid MBE-Based Growth Method for Large-Area Synthesis of Stacked Hexagonal Boron Nitride/Graphene Heterostructures. *Sci. Rep.* **2017,** 7, 43644.

[30] Xu, Z.; Khanaki, A.; Tian, H.; Zheng, R.; Suja, M.; Zheng, J.-G.; Liu, J. Direct Growth of Hexagonal Boron Nitride/Graphene Heterostructures on Cobalt Foil Substrates by Plasma-Assisted Molecular Beam Epitaxy. *Appl. Phys. Lett.* **2016,** 109, 043110.

[31] Xu, Z.; Tian, H.; Khanaki, A.; Zheng, R.; Suja, M.; Liu, J. Large-Area Growth of Multi-Layer Hexagonal Boron Nitride on Polished Cobalt Foils by Plasma-Assisted Molecular Beam Epitaxy. *Sci. Rep.* **2017,** 7, 43100.

[32] Xu, Z.; Zheng, R.; Khanaki, A.; Zuo, Z.; Liu, J. Direct Growth of Graphene on In Situ Epitaxial Hexagonal Boron Nitride Flakes by Plasma-Assisted Molecular Beam Epitaxy. *Appl. Phys. Lett.* **2015,** 107, 213103.

[33] Zuo, Z.; Xu, Z.; Zheng, R.; Khanaki, A.; Zheng, J.-G.; Liu, J. In-Situ Epitaxial Growth of Graphene/h-BN van der Waals Heterostructures by Molecular Beam Epitaxy. *Sci. Rep.* **2015,** 5, 14760.

[34] Zheng, R.; Khanaki, A.; Tian, H.; He, Y.; Cui, Y.; Xu, Z.; Liu, J. Precipitation Growth of Graphene under Exfoliated Hexagonal Boron Nitride to Form Heterostructures on Cobalt Substrate by Molecular Beam Epitaxy. *Appl. Phys. Lett.* **2017,** 111, 011903.

[35] Khanaki, A.; Tian, H.; Xu, Z.; Zheng, R.; He, Y.; Cui, Z.; Yang, J.; Liu, J. Effect of High Carbon Incorporation in Co Substrates on the Epitaxy of Hexagonal Boron Nitride/Graphene Heterostructures. *Nanotechnology* **2017,** 29, (3), 035602.

[36] Perdew, J. P.; Burke, K.; Ernzerhof, M. Generalized Gradient Approximation Made Simple. *Phys. Rev. Lett.* **1996,** 77, (18), 3865.

[37] Ernzerhof, M.; Scuseria, G. E. Assessment of the Perdew–Burke–Ernzerhof Exchange-Correlation Functional. *The Journal of Chemical Physics* **1999,** 110, (11), 5029-5036.

[38] Henkelman, G.; Uberuaga, B. P.; Jónsson, H. A Climbing Image Nudged Elastic Band Method for Finding Saddle Points and Minimum Energy Paths. *The Journal of chemical physics* **2000,** 113, (22), 9901-9904.

[39] Kula, P.; Pietrasik, R.; Dybowski, K. Vacuum Carburizing—Process Optimization. *J. Mater. Process. Technol.* **2005,** 164, 876-881.

[40] Xie, J.; Spallas, J. P. Different Contrast Mechanisms in SEM Imaging of Graphene, Technical Report, Agilent Technologies; http://www.toyo.co.jp/file/pdf/spm/files/agi/5991-0782EN.pdf, 2012.

[41] Gorbachev, R. V.; Riaz, I.; Nair, R. R.; Jalil, R.; Britnell, L.; Belle, B. D.; Hill, E. W.; Novoselov, K. S.; Watanabe, K.; Taniguchi, T.; Geim, A. K.; Blake, P. Hunting for monolayer boron nitride: optical and Raman signatures. *Small* **2011,** 7, (4), 465-468

[42] Koh, A. T.; Foong, Y. M.; Chua, D. H. Comparison of the Mechanism of Low Defect Few-layer Graphene Fabricated on Different Metals by Pulsed Laser Deposition. *Diamond Relat. Mater.* **2012,** 25, 98-102.

[43] Stenger, I.; Schue, L.; Boukhicha, M.; Bérini, B.; Placais, B.; Loiseau, A.; Barjon, J. Low Frequency Raman Spectroscopy of Few-Atomic-Layer Thick hBN Crystals. *2D Mater.* **2017**, 4, 031003.

[44] Greenler, R. G.; Slager, T. Spectrochim. Method for Obtaining the Raman Spectrum of a Thin Film on a Metal Surface. *Acta, Part A* **1973,** 29, 193-201.

[45] Zheng, M.; Takei, K.; Hsia, B.; Fang, H.; Zhang, X.; Ferralis, N.; Ko, H.; Chueh, Y.-L.; Zhang, Y.; Maboudian, R.; Javey, A. Metal-catalyzed crystallization of amorphous carbon to graphene. *Appl. Phys. Lett.* **2010,** 96, (6), 063110.

[46] Rodríguez-Manzo, J. A.; Pham-Huu, C.; Banhart, F. Graphene Growth by a Metal-catalyzed solid-state Transformation of Amorphous Carbon. *ACS Nano* **2011,** 5, 1529-1534.

[47] Pease, R. S. An X-ray Study of Boron Nitride. *Acta Crystallogr.* **1952,** 5, 356-361.

[48] Johnson, W. A. Reaction Kinetics in Process of Nucleation and Growth. *Transaction of AIME* **1939,** 135, 416-458.

[49] Kim, H.; Mattevi, C.; Calvo, M. R.; Oberg, J. C.; Artiglia, L.; Agnoli, S.; Hirjibehedin, C. F.; Chhowalla, M.; Saiz, E. Activation Energy Paths for Graphene Nucleation and Growth on Cu. *ACS Nano* **2012,** 6, 3614-3623.

[50] Weatherup, R. S.; Shahani, A. J.; Wang, Z.-J.; Mingard, K.; Pollard, A. J.; Willinger, M.-G.; Schloegl, R.; Voorhees, P. W.; Hofmann, S. In Situ Graphene Growth Dynamics on Polycrystalline Catalyst Foils. *Nano Lett.* **2016,** 16, (10), 6196-6206.

[51] Li, J.; Wang, J.; Xu, Q.; Yang, G. Comparison of Johnson–Mehl–Avrami–Kologoromov (JMAK) Kinetics with a Phase Field Simulation for Polycrystalline Solidification. *Acta Mater.* **2007,** 55, (3), 825-832.

[52] Kooi, B. J. Monte Carlo Simulations of Phase Transformations Caused by Nucleation and Subsequent Anisotropic Growth: Extension of the Johnson-Mehl-Avrami-Kolmogorov Theory. *Phys. Rev. B* **2004,** 70, (22), 224108.

[53] Lee, G.-H.; Yu, Y.-J.; Lee, C.; Dean, C.; Shepard, K. L.; Kim, P.; Hone, J. Electron Tunneling through Atomically Flat and Ultrathin Hexagonal Boron Nitride. *Appl. Phys. Lett.* **2011,** 99, 243114.

[54] Hattori, Y.; Taniguchi, T.; Watanabe, K.; Nagashio, K. Layer-By-Layer Dielectric Breakdown of Hexagonal Boron Nitride. *ACS Nano* **2014,** 9, 916-921.

[55] Schwarz, M.; Riss, A.; Garnica, M.; Ducke, J.; Deimel, P. S.; Duncan, D. A.; Thakur, P. K.; Lee, T.-L.; Seitsonen, A. P.; Barth, J. V. Corrugation in the Weakly Interacting Hexagonal-BN/Cu (111) System: Structure Determination by Combining Noncontact Atomic Force Microscopy and X-Ray Standing Waves. *ACS Nano* **2017,** 11, (9), 9151-9161.

[56] Koepke, J. C.; Wood, J. D.; Chen, Y.; Schmucker, S. W.; Liu, X.; Chang, N. N.; Nienhaus, L.; Do, J. W.; Carrion, E. A.; Hewaparakrama, J. Role of Pressure in the Growth of Hexagonal Boron Nitride Thin Films from Ammonia-Borane. *Chem. Mater.* **2016,** 28, (12), 4169-4179.

[57] Panayiotatos, Y.; Logothetidis, S.; Handrea, M.; Kautek, W. Homogeneous and Amorphous Sputtered Sp3-Bonded BN Films at RT: a Stress, Spectroscopic Ellipsometry and XPS Study. *Diamond Relat. Mater.* **2003,** 12, (3-7), 1151-1156.

[58] Widmayer, P.; Boyen, H.-G.; Ziemann, P.; Reinke, P.; Oelhafen, P. Electron Spectroscopy on Boron Nitride Thin Films: Comparison of Near-Surface to Bulk Electronic Properties. *Phys. Rev. B* **1999,** 59, 5233.

[59] Khanaki, A.; Xu, Z.; Tian, H.; Zheng, R.; Zuo, Z.; Zheng, J.-G.; Liu, J. Self-Assembled Cubic Boron Nitride Nanodots. *Sci. Rep.* **2017,** 7, 4087.

[60] Bonzel, H.; Krebs, H. On the Chemical Nature of the Carbonaceous Deposits on Iron After CO Hydrogenation. *Surf Sci.* **1980,** 91, 499-513.

[61] Panzner, G.; Diekmann, W. The Bonding State of Carbon Segregated to α-iron Surfaces and on Iron Carbide Surfaces Studied by Electron Spectroscopy. *Surf Sci.* **1985,** 160, 253-270.

[62] Zhang, C.; Zhao, S.; Jin, C.; Koh, A. L.; Zhou, Y.; Xu, W.; Li, Q.; Xiong, Q.; Peng, H.; Liu, Z. Direct Growth of Large-area Graphene and Boron Nitride Heterostructures by a Co-Segregation Method. *Nat. Commun.* **2015,** 6, 6519.

[63] Ishida, K.; Nishizawa, T. The C-Co (Carbon-Cobalt) System. *J. Phase Equilib.* **1991,** 12, 417-424.

[64] van Helden, P.; Ciobîcă, I. M. A DFT Study of Carbon in the Subsurface Layer of Cobalt Surfaces. Chem. Phys. Chem **2011**, 12, (16), 2925-2928.

[65] Jansen, A. P.; Agrawal, R.; Spanu, L. Thermodynamics and Kinetics of Carbon Deposits on Cobalt: a Combined Density Functional Theory and Kinetic Monte Carlo Study. PCCP **2016**, 18, (41), 28515-28523.

[66] Xu, J.; Saeys, M. First Principles Study of the Stability and the Formation Kinetics of Subsurface and Bulk Carbon on a Ni Catalyst. The Journal of Physical Chemistry C **2008**, 112, (26), 9679-9685.

[67] Shirasaki, T.; Derré, A.; Ménétrier, M.; Tressaud, A.; Flandrois, S. Synthesis and Characterization of Boron-Substituted Carbons. *Carbon* **2000,** 38, (10), 1461-1467.

[68] Wada, Y.; Yap, Y.; Yoshimura, M.; Mori, Y.; Sasaki, T. The Control of BN and BC Bonds in BCN Films Synthesized Using Pulsed Laser Deposition. *Diamond Relat. Mater.* **2000,** 9, (3-6), 620-624.

[69] Jensen, F.; Besenbacher, F.; Lægsgaard, E.; Stensgaard, I. Surface Reconstruction of Cu (110) Induced by Oxygen Chemisorption. *Phys. Rev. B* **1990,** 41, 10233.

[70] Li, X.; Cai, W.; An, J.; Kim, S.; Nah, J.; Yang, D.; Piner, R.; Velamakanni, A.; Jung, I.; Tutuc, E. Large-Area Synthesis of High-Quality and Uniform Graphene Films on Copper Foils. *Science* **2009,** 324, 1312-1314.

[71] Hasegawa, Y.; Avouris, P. Direct Observation of Standing Wave Formation at Surface Steps Using Scanning Tunneling Spectroscopy. *Phys. Rev. Lett.* **1993,** 71, 1071.

[72] Liu, S.; van Duin, A. C.; van Duin, D. M.; Liu, B.; Edgar, J. H. Atomistic Insights into Nucleation and Formation of Hexagonal Boron Nitride on Nickel from First-Principles-Based Reactive Molecular Dynamics Simulations. *ACS Nano* **2017,** 11, 3585-3596.

[73] Robinson, V.; Robins, J. Nucleation Kinetics of Gold Deposited onto UHV Cleaved Surfaces of NaCl and KBr. Thin Solid Films 1974, 20, (1), 155-175.

[74] Kresse, G.; Hafner, J. Ab Initio Molecular Dynamics for Liquid Metals. *Phys. Rev. B* **1993,** 47, (1), 558.

Chapter 4 Growth Dynamics of Millimeter-sized Single-crystal Hexagonal Boron Nitride Monolayers on Secondary Recrystallized Ni (100) Substrates

4.1. Introduction

Within the two dimensional (2D) material family, hexagonal boron nitride (h-BN) plays a critical role as the 2D dielectric and wide band gap semiconductor [1-4]. In recent years, there have been many reports on large-area single-crystal graphene and transition metal dichalcogenides (TMDs) well over a few millimeter to centimeter [5, 6] as well as a variety of industrially scalable approaches [7, 8]. In comparison, the development of the 2D h-BN is relatively immature. The domain size is mostly less than 100 micrometers. Reports on h-BN domains with a size close to one millimeter are rare [9, 10]. Although wafer-scale single crystals have been reported through the coalescence of identically aligned h-BN domains [11], on twin-free single-crystal Rh (111) thin films [12], and on low-symmetry Cu (110) vicinal surface [13], it is noted that discrete h-BN domains or flakes over one millimeter have not been reported, and the understanding of the growth dynamics remains elusive. Controllable synthesis of large-size single-crystal h-BN is highly desirable but challenging. A great deal of h-BN synthesis is carried out on various transition metal substrates, such as Cu [1, 2, 14], Co [15, 16], Ni [17, 18], Fe [19-21], thanks to their catalytic activities favorable for the nucleation and growth of high-quality h-BN. Nevertheless, rational engineering of catalytic effects of a given transition metal substrate by alloying or incorporating dissimilar species has been rarely studied for the h-BN growth in order to enhance the control of layer number, nucleation density, and domain size; the only available efforts to date are Si-doping or N-doping of Fe substrates [19, 21], oxygen passivation of Cu substrates [22] and carbon incorporation of Co/Ni substrates [10].

While majority of the h-BN synthesis effort have been performed using chemical vapor deposition (CVD), molecular beam epitaxy (MBE) is versatile in terms of its ability to precisely control solid, gas, and plasma sources and tune the growth parameters. MBE has already been used to grow 2D h-BN and h-BN/graphene heterostructures [10, 23-29]. In this work, we report the synthesis of millimeter-size single-crystal h-BN domains through an interstitial carbon assisted approach in an MBE system. While the interstitial carbon assisted growth of h-BN has been proposed in our recent effort [10], leading to a large single-crystal h-BN flake of 600-700 μm, it is essential to achieve even larger single-crystal h-BN flakes with edge lengths on the order of millimeters or even continuous wafer-scale single-crystal 2D films. In addition, the growth thermal dynamics and kinetics in terms of temperature-dependent growth and substrate surface engineering have not been comprehensively studied; numerical simulations are necessary to further elucidate the effect of the carbon incorporation on the tuning of the catalytic activities of transition metal substrates for complete controlled growth of large 2D h-BN single crystals. Here, we designed Ni substrates with carburization process through pretreatment of secondary recrystallized Ni with acetylene prior to the actual growth of h-BN. The growth dynamics were studied by tuning different growth parameters including substrate temperature, and B and N source ratio. From the perspective of activation energy through density functional theory (DFT) calculations, we rationalized the role of interstitial carbon incorporation in enhancing the catalytic activities of the transition metals. Through the control of the growth parameters, a single-crystal h-BN monolayer domain with a size as large as 1.4 mm in edge

length was achieved. Furthermore, a high-quality continuous single-layer h-BN with an extremely high breakdown electric field of 9.75 MV/cm was demonstrated.

4.2. **Experimental details**

Substrate preparation Ni foils with a thickness of 0.1 mm and a purity of 99.995% from Alfa Aesar were polished on a SBT 920 Lapping and Polishing workstation and cut into 1 cm × 1 cm pieces as substrates. These pieces were degreased and deoxidized with acetone, IPA and diluted hydrochloric acid (10%), rinsed in deionized (DI) water, blown dry and finally loaded into an MBE chamber.

Hydrogen annealing and carburization A re-designed Perkin-Elmer MBE system with a background pressure of ~10^{-9} Torr was used for the sample growth. The substrate was heated to 950 ºC and annealed at this temperature under a 10-sccm flow of hydrogen gas for 60 minutes to enhance the recrystallization of Ni. Then, the substrate temperature was adjusted to the growth temperature. 0.5-sccm C_2H_2 gas was introduced into chamber with a pressure of 5×10^{-5} Torr to enrich Ni with carbon prior to h-BN growth. H-BN growth step started after the carburization process.

H-BN growth A Knudsen effusion cell filled with B_2O_3 powder (Alfa Aesar, 99.999% purity) was used as boron (B) source. Nitrogen plasma (Airgas, 99.9999% purity) generated by an electron cyclotron resonance (ECR) system and high-purity ammonia (American Gas Group, 99.9995% purity) were used as nitrogen (N) sources. The h-BN growth was conducted by simultaneous introduction of B and N sources onto the Ni

substrate at 890-950 ºC. B cell temperature was maintained at constant temperature throughout the growth. NH_3 gas was controlled at a constant flow rate by a Mass Flow Controller (MFC) and introduced to the chamber through a shut-off valve. Nitrogen plasma as an alternative N source is generated from an ECR plasma source with a power of 228 W. The growth pressure was on the order of 10^{-4} Torr. After the growth, the samples were cooled to room temperature at a rate of 10 ºC/min.

Transferring of h-BN samples The Ni substrates were etched by $FeCl_3$/HCl solution after spin-coating PMMA (495 A4) on as-grown samples. The PMMA/h-BN stack was then transferred into 10% HCl, 5% HCl and DI water successively to rinse out the residual etchant. The floating h-BN film was taken out by a desired substrate and left to dry for at least 12 hours. After that, a few drops of PMMA were deposited again on the transferred film and soaked for another two hours. The additional PMMA is used to soften the previous PMMA layer and enhance the attachment of h-BN on the substrate. PMMA was removed by dipping the sample into acetone bath. Finally, the sample was annealed at 400 °C inside a CVD furnace for 3 hours in Ar/O_2 flow of 300 sccm to remove any remaining organic residue.

Characterizations SEM images were acquired using an FEI NNS450 system in secondary electron (SE) imaging mode with a beam voltage of 10 kV. Raman characterizations were performed using a HORIBA LabRam system equipped with a 60-mW, 532-nm green laser. XPS characterization was conducted using a Kratos AXIS ULTRA XPS system equipped with an Al Kα monochromatic X-ray source and a 165-mm mean radius electron energy hemispherical analyzer. The fitting of XPS data was

performed using CasaXPS software. As-measured XPS data was first calibrated by using Ni $2p_{3/2}$ peak at 852.6 eV (Lorentzian Asymmetric line shape). B 1s, N 1s peaks were convoluted with Gaussian/Lorentzian line shape after background-corrected by Shirley type background. AFM images were obtained using a Veeco D5000 AFM system. TEM images and selected area electron diffraction (SAED) patterns were acquired using a FEI Tecnai12 system. TEM sample was prepared by picking a transferred h-BN film using a 200-mesh Cu grid covered with holey carbon film with orthogonal array of 1.2-μm diameter holes.

Device fabrication and electrical measurement Ni(contact)/h-BN/Ni(foil) two-terminal devices were fabricated by a standard photolithography and lift-off process. A Ni layer of 100 nm was patterned as top square contacts with an edge length of 50 μm on the surface of as-grown h-BN film. Reactive ion etching (RIE) was performed with a 50-sccm SF_6 plasma, under a power of 50 W, and for 15 seconds to etch the h-BN film between devices, which ensured isolation of different devices on the same substrate. Current-voltage (I-V) characteristics were obtained by an Agilent 4155C semiconductor parameter analyzer equipped with probing tips having a diameter of about 5 μm (Signatone, SE-TL).

DFT calculations First-principles density functional theory (DFT) calculations used the projector augmented wave method and the Perdew-Burke-Ernzerhof (PBE) type generalized gradient approximation [50, 51] as implemented in the software package VASP [52]. Spin polarization was included self-consistently in all calculations. For the unit cell calculations, a Monkhorst-Pack scheme was adopted to integrate over the Brillouin zone with a k-mesh of 9×9×1. A plane-wave basis cutoff of 550 eV was used. All structures

were optimized until the largest force on the atoms was less than 0.01 eV/Å. We have modeled the adsorption energies of B and N atoms on the (100) surface of Ni. A single B or N atom was placed on specific sites of the surface of a supercell consisting of four atomic layers of Ni atoms. The supercell size in the XY-plane for (100) surface is 4×4. The integration over the Brillouin zone for the surfaces was done with a converged k-mesh of 3×3×1. These sites include the top, 2-fold bridge and 4-fold hollow site of Ni (100), on which the adsorption of B or N atoms would enable an epitaxial relationship between h-BN and the substrates. A vacuum gap of 15 Å was introduced to avoid interactions between the periodically repeated surfaces. To simulate the diffusion activation energies, we adopted the climbing image nudged elastic band (CI-NEB) method [53]. The spring force between adjacent images was set to 5.0 eV/Å. The migration energies, namely diffusion activation energies were obtained for the different adsorbates between the different sites of the (100) surface of Ni. The initial and final positions of the adsorbed atoms were set at two hollow sites of Ni (100). Eight images were considered to calculate the activation energies between the initial and final states. For calculation of adsorption and diffusion energies for B and N on carbon-incorporated Ni, one interstitial carbon occupying the octahedral site in a supercell of Ni (100), which is 1.58 Å below the surface, was assumed.

4.3. **Results and discussion**

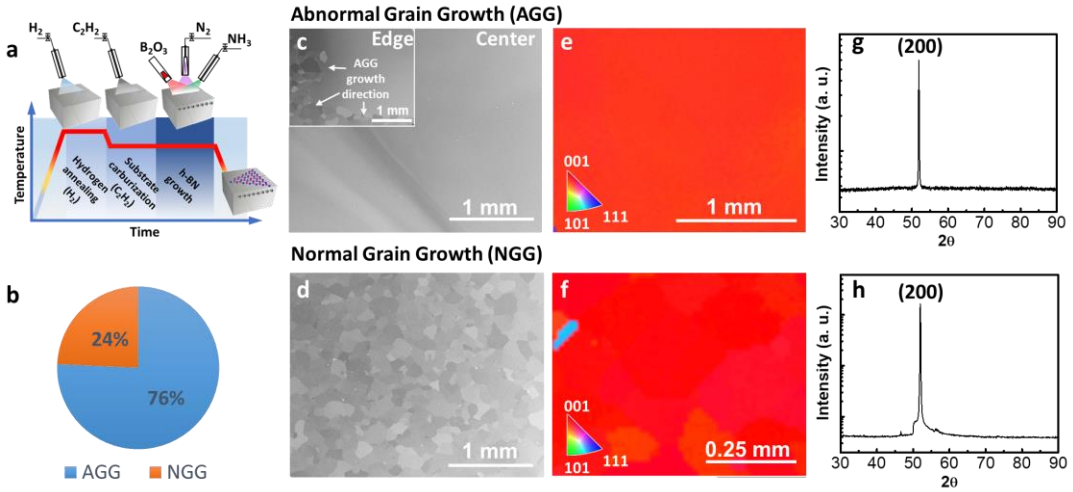

Figure 4.1 Characterization of Ni substrate after annealing. (a) Schematic of a typical growth procedure. (b) Statistics of 100 AGG and NGG samples with annealing temperature at 950 °C and growth temperature from 890 - 950 °C. (c, d) SEM images, (e, f) EBSD mapping, and (g, h) XRD spectra of post-annealed AGG and NGG Ni substrates, respectively. Inset in c shows an SEM image at the edge of the sample where boundary between AGG and NGG can be clearly seen. The white arrows indicate the migration directions of the abnormal grain.

We adopt a simple MBE growth procedure as illustrated in Figure 4.1a, in which Ni substrate undergoes three growth steps including hydrogen annealing, substrate carburization and h-BN growth. The hydrogen annealing temperature is controlled at 950 °C , which is slightly higher than the growth temperature (890-950 °C), in order to enhance the recrystallization of Ni. Figure 4.1b-h summarize morphology results of Ni substrates after 1-hour hydrogen annealing at 950 °C. The grains in as-received Ni foils have been deformed by cold rolling, and, as a result, additional dislocations are formed, and the grain boundary surface area is increased. Upon annealing, recrystallization and grain growth occur in order to reduce the internal energy. In general, there are two different types of grain growth, which are Normal Grain Growth (NGG) and Abnormal Grain

Growth (AGG) [30]. NGG usually stops when the average grain size is comparable with the substrate thickness, and the grain size is uniformly distributed. AGG is also known as secondary recrystallization, in which only a small population of the grains which are favored will grow in consumption of another population which is not favored, due to the surface and interface energy anisotropy, resulting in the formation of considerably large grains [30]. Figure 4.1c shows an scanning electron microscope (SEM) image of a typical Ni substrate with AGG grains (denoted as AGG Ni) after 1-h hydrogen annealing at 950 °C . The majority of the substrate consists of only a few grains with a size of a few millimeters. The inset image was taken at the edge of the sample where the boundary between AGG grains and NGG grains is identified. The AGG growth direction is indicated by the white arrows. In contrast, typical NGG Ni with the same annealing condition has small grains with an average size of ~100 μm, which is comparable to the foil thickness. Electron backscatter diffraction (EBSD) mapping reveals that the dominant texture is (100) for both AGG and NGG Ni (Figure 4.1e&f), which is also confirmed by X-ray diffraction (XRD) as seen in Figure 4.1g&h, respectively. This is because (100) grains have lower strain energy density compared to grains with other surface planes in the elastic region [31]. The

Table 4.1 Summary of growth conditions of the typical samples

Step	Parameters	Sample I	Sample II	Sample III	Sample IV
Hydrogen Annealing	Substrate	Ni (AGG)	Ni (AGG)	Ni (NGG)	Ni (AGG)
	Substrate temperature [ºC]	950	950	950	950
	Hydrogen gas flow [sccm]	10	10	10	10
	Duration [mins]	60	60	60	60
Carburization	Acetylene gas flow [sccm]	0.5	0.5	0.5	0.5
	Duration [s]	300	300	300	300
	Substrate temperature [ºC]	910	910	910	910
H-BN Growth	Substrate temperature [ºC]	910	910	910	910
	Boron cell temperature [ºC]	1150	1120	1120	1130
	Ammonia gas flow [sccm]	5	10	10	10
	Nitrogen gas flow [sccm]	10	0	0	0
	Nitrogen ECR current [mA]	60	-	-	-
	Duration [hours]	8	8	8	8

narrow peak in XRD in Figure 4.1g reveals good single crystallinity for the AGG substrate compared to the wide peak in Figure 4.1h for NGG Ni. Even though majority of the substrates used in this work have gone through AGG, a small portion of them show only NGG. Statistics of 100 samples grown at 890 – 950 °C after 1-h annealing at 950 °C shows that AGG occurance is 76%, while NGG occurs in the remaining 24%. We attribute this to the variation in strain and stress level during the cold working process in the as-received Ni foils. In general, secondary recrystallization is a cheap and easy way to produce single-crystal metal. Different methods such as cyclic heat treatment, and impurity incorporation have been reported to enhance the AGG [32, 33]. The engineering of post processing procedure in order to produce AGG is beyond the scope of this work. Here, we focus on the study of h-BN growth on AGG Ni (100) substrates.

The next crucial step for enabling the formation and growth of h-BN including large single-crystal flakes and high-quality continuous films is the incorporation of carbon in these Ni (100) substrates. Table 4.1 summarizes four typical h-BN samples (Samples I-IV), and all these samples underwent a carburization process by introducing a 0.5-sccm acetylene flux for 300 s at 910 °C. Figure 4.2a shows an SEM image of a reference sample

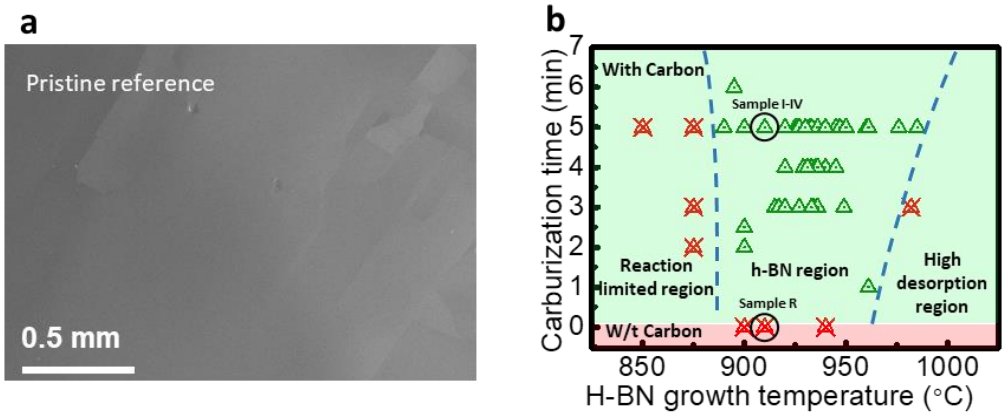

Figure 4.2 (a) SEM image of a reference sample grown with the same growth condition as Sample II except the substrate carburization step. (b) Summary of 58 samples grown at different carburization time and substrate temperature. Green marks label successful h-BN growth, and red marks label unsuccessful h-BN growth. The h-BN growth duration for green-marked samples is between 3 and 8 hours, while the growth of red-marked samples lasted more than 6 hours. The blue dashed lines are guide of eyes to identify the h-BN growth window. The circles indicate where the reference sample in (a) and Samples I-IV described in Table 4.1 are located.

grown with the same growth condition as Sample II except that there was no substrate carburization step. As seen from the image, the sample shows typical AGG Ni grains and texture without any h-BN on the substrate. Figure 4.2b shows the statistical summary of 58 samples regarding the effect of substrate carburization on the h-BN growth on AGG Ni (100) at different temperature. Without carburization, the growth of h-BN was not successful, as indicated by the red markers at zero carburization time in the figure. With

carburization, there is a temperature window for successful h-BN growth as indicated by

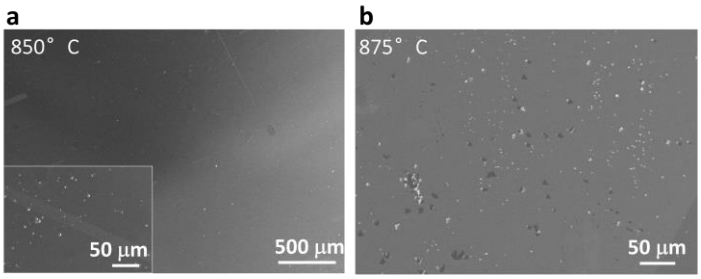

Figure 4.3 SEM images of samples with 10-sccm N_2 plasma and 5-sccm NH_3 on 300-s carburized AGG Ni substrates grown for 3 hours at (a) 850 °C, and (b) 875 °C.

blue dashed lines in the figure. In addition, the growth temperature window opens up wider as the carburization time increases. As the growth temperature is lower than ~875 °C, only some sparse white features, which are not h-BN, were deposited on the substrates, as shown in Figure 4.3. This region lies in kinetically controlled region due to low-temperature effect [34, 35] and is labeled as reaction-limited region. As the growth temperature is higher than ~960-980 °C indicated by the right blue dashed line in the figure, no h-BN could be grown due to high desorption of B and N atoms. It should be noted that the amount of carbon dissolved in the Ni substrates during the carburization process here is low, thus they will not precipitate to be incorporated into h-BN film or form graphene during the sample cooling period. Detailed experimental proof can be found elsewhere [10, 29]. The rationale of the carburization effect on the growth of h-BN can be further clarified as we continue to discuss the experiment and simulation details.

Figure 4.4 gives an overview of h-BN growth under typical conditions (Samples I-IV). Sample I was grown using a mixture of nitrogen plasma and ammonia (NH_3) as the nitrogen source (refered as mixed nitrogen source). Sample I serves as the baseline sample as similar

growth condition was reported in the previous work [10]. Nitrogen plasma can provide N radicals. On the other hand, NH_3 can be efficiently decomposed to absorbed N atoms on hot Ni surface, for example, at a temperature of 430 K, a decomposition efficiency of 23% was attained [36]. While the mixture of nitrogen plasma and ammonia gas can potentially provide more N sources, the chemistry of the formation of h-BN can be more complicated compared with sole nitrogen sources. Here, pure NH_3 gas was adopted as the N source in the growth of Sample II-IV. Figure 4.4a-c show SEM and dark-field optical microscope (DF-OM) images of Sample I. Complementary to SEM imaging, DF-OM imaging is also a non-destructive method to effectively visualize 2D material on metal [37]. DF-OM imaging relying on scattered light can pick up the uneveness on a surface easily. As seen from Figure 4.4a-c, h-BN flakes over 0.5 mm were achieved. Figure 4.4d-f show SEM and DF-OM images of Sample II. H-BN flakes with a size over 1 mm were achieved with lower nucleation density compared to Sample I. Sample III was grown under the same condition with Sample II. However, Ni substrate in Sample II underwent AGG, thus it can be treated as single-crystal substrate, while only NGG was observed in Sample III. In comparison to Sample II, both flake size and uniformity were compromised (Figure 4.4g-i). H-BN adlayers (white features) can be occasionally observed across the sample. As discussed above, even though both AGG and NGG Ni substrates are uniform in texture with (100) as the dominant texture, more grain boundaries on NGG substrate act as additional preferential nucleation sites for h-BN. Increased roughness also hinders the surface diffusion of adatoms which limits the domain size. Growth condition was further controlled by increasing B source flux. As the B cell temperature increases to 1130 °C, continuous h-

BN film (Sample IV) was achieved on AGG Ni as seen in Figure 4.4j-l. Figure 4.4j shows an SEM image of the center of the sample where continuous h-BN film is observed. Figure 4.4k and 4.4l show an SEM image and a DF-OM image of the edge area of the sample, respectively. By comparing the SEM and DF-OM imaging at the same area, a flake with a size close to 2 mm can be indentified using the contrast in DF-OM (Figure 4.4l). The grain boundary is revealed under DF-OM because the thermal induced corrugation depends on the alignment between h-BN and the metal substrate [38].

X-ray photoemission spectroscopy (XPS) was performed on as-grown Sample II to further confirm the existence and stoichiometry of h-BN. The binding energies of B 1s and N 1s are shown to be at 190.0 eV and 397.5 eV, respectively (Figure 4.5a), with a stoichiometry ratio of unity. The sample was further transferred onto a variety of substrates for further characterizations. Figure 4.5b shows a UV-vis absorption spectrum performed

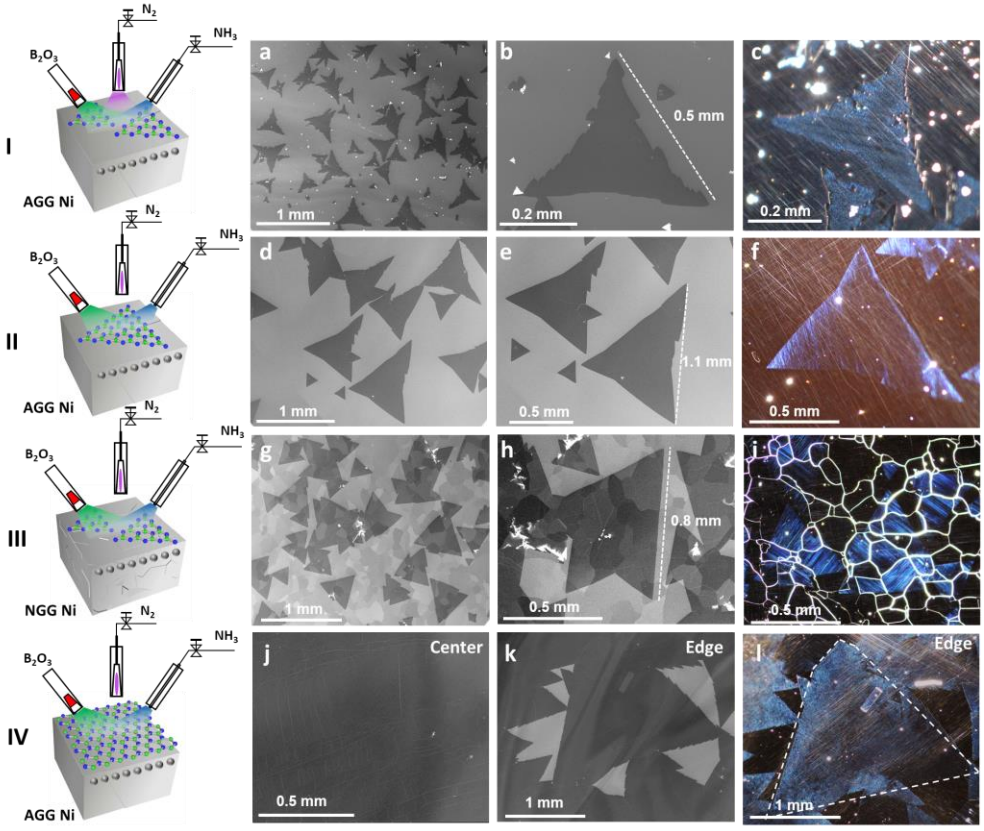

Figure 4.4 Overview of mm-sized single-crystal h-BN flakes and continuous h-BN monolayer. (a-i) Large-area SEM, small-area SEM, DF-OM images of single-crystal h-BN flakes grown with (a-c) a mixture of 10-sccm N_2 plasma and 5-sccm NH_3 on AGG Ni (Sample I), (d-f) 10-sccm NH_3 on AGG Ni (Sample II), and (g-i) 10-sccm NH_3 on NGG Ni (Sample III). (j) SEM image of the center area, and (k-l) SEM and DF-OM images of the edge area, respectively, of a continuous h-BN monolayer sample grown on AGG Ni with 10-sccm NH_3 and B_2O_3 effusion cell temperature at 1130 °C (Sample IV). Detailed growth conditions of these samples are summarized in the Experimental details section.

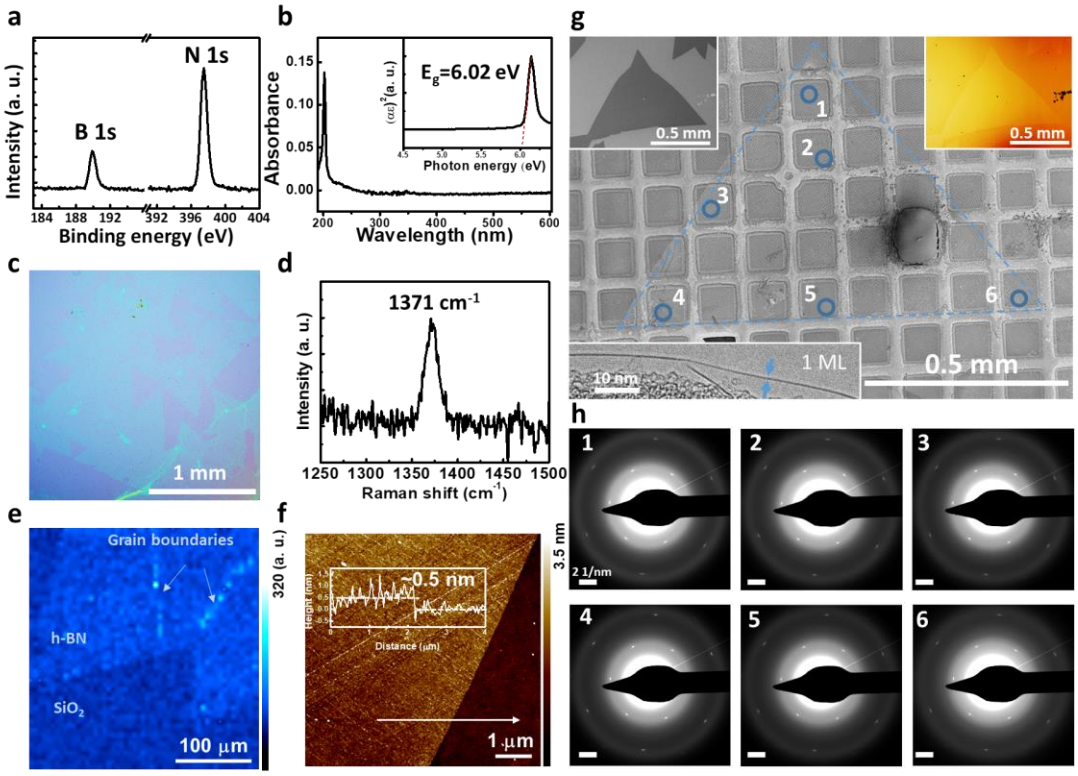

Figure 4.5 Characterization of typical single h-BN flake (Sample II). (a) XPS B 1s and N 1s spectra. (b) UV-Vis absorption spectrum of a transferred h-BN sample on sapphire. Inset is $(A\varepsilon)^{1/2}$ versus ε curve. (c) Optical microscope image of h-BN flakes transferred onto SiO_2 substrate. (d) Raman spectrum of h-BN film transferred onto SiO_2/Si substrate. The spectrum was background corrected by subtracting the background signal from SiO_2/Si substrate. (e) Raman mapping of an h-BN flake near the edge. The arrow indicates the grain boundaries where a typical overlapping grain boundary can be found. Higher intensity of Raman signal is due to larger thickness. (f) AFM image of h-BN flake transferred onto SiO_2/Si substrate. The inset shows the scan profile across the white arrow. The thickness is measured as ~0.5 nm. (g) SEM image of one such flake of Sample II transferred onto a copper grid coated with holey carbon film with the inset displaying a TEM image at the edge of the flake. (h). SAED patterns at 6 different locations across the h-BN flake in (g) indicated by 1-6.

after the sample was transferred onto a sapphire substrate. A strong peak at 203 nm with a sharp absorption edge can be observed, corresponding to a band gap of 6.02 eV for h-BN extracted from the Tauc equation for a direct bandgap (inset in Figure 4.5b) [39]. Figure 4.5c shows an OM image of the h-BN flakes transferred onto a SiO_2/Si substrate. Raman

spectroscopy was further performed on the transferred sample. An E_{2g} phonon mode at 1371 cm^{-1} can be found in the Raman spectrum with a full width at half maximum (FWHM) of 17.8 cm^{-1}, corresponding to monolayer h-BN [40] (Figure 4.5d). Large-area Raman mapping at the edge of a domain is presented in Figure 4.5e. The uniform contrast indicates good quality. It is worth noting that multilayer regions of finite width (~5 μm) are often found at the grain boundaries. Similar phenomenon was reported and discussed elsewhere [10]. Figure 4.5f shows an AFM image of the transferred h-BN. A step height at the flake edge was measured as 0.5 nm, which is consistent with the monolayer h-BN thickness on SiO_2 [40]. An AFM scan was also performed on the as-grown sample and the result is shown in Figure 4.6. The root mean square (RMS) roughness of the film is 3.67 nm while the RMS roughness of the AGG Ni substrate is ~1.04 nm. The increased roughness is due to further reconstruction of the Ni surface during the growth of the h-BN film, which conforms onto the area [38].

Transmission electron microscopy (TEM) analysis was conducted to confirm the single-crystal nature of the mm-sized h-BN domains. Figure 4.5g shows an SEM image of a mm-sized h-BN flake in Sample II which was transferred onto a mesh-200 Cu grid covered by

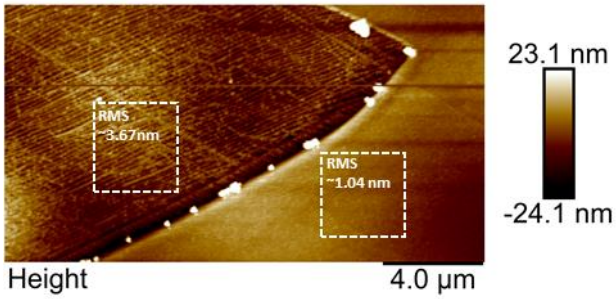

Figure 4.6 AFM image of as-grown h-BN sample. The areas enclosed by the dashed lines are used to estimate the RMS roughness.

holey carbon film. The h-BN flake outlined by blue dashed lines can be clearly seen, despite the residue introduced during the transfer process. SEM and OM images of the same flake on the as-grown sample area are also shown in the upper left and upper right insets, respectively. It is worth noting that the OM image was taken after oxidization in air in order to enhance the contrast. Selective area electron diffraction (SAED) patterns at six different spots were collected across the flakes as marked by the blue circles and labeled with numbers 1-6. The corresponding SAED patterns are shown in Figure 4.5h. The identical six-fold symmetric diffraction spots confirm the single-crystallinity of the mm-sized domain and high quality. The monolayer layer nature is further confirmed by the TEM edge analysis (bottom left inset in Figure 4.5g).

Growth temperature plays an important role in the growth dynamics. Figure 4.7a-e shows SEM images of samples grown from 890 °C to 950 °C. All other growth conditions are the same including AGG Ni (100) substrate, 0.5 sccm acetlyne carburization for 5 min, amonnia source of 10 sccm, and boron cell at 1120 °C. Figure 4.7f shows a plot of the

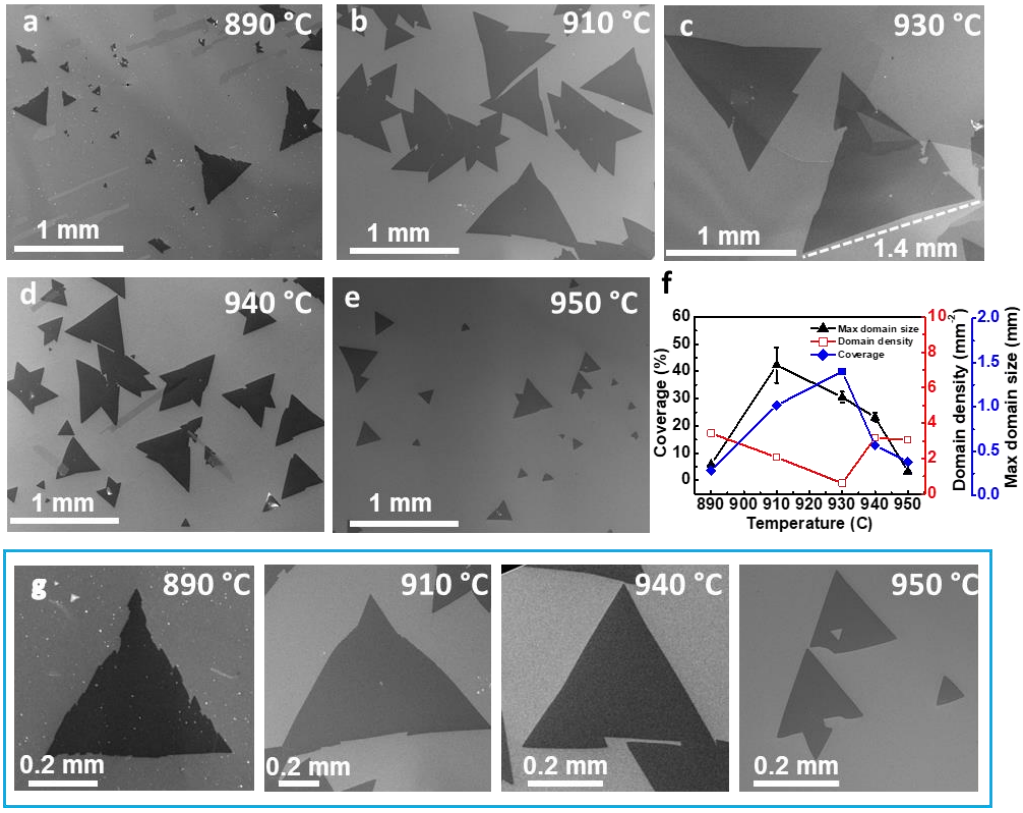

Figure 4.7 Substrate temperature control of large-size single-crystal h-BN flakes. (a-e) SEM images of h-BN samples grown at 890 °C, 910 °C, 930 °C, 940 °C and 950 °C, respectively. (f) Plot of coverage, domain density and maximum domain size as a function of temperature. (g) Zoom in SEM images showing typical h-BN flakes grown with different substrate temperature at 890 °C, 910 °C, 940 °C and 950 °C, respectively.

coverage, domain density and maximum domain size as a function of the growth temperature. SEM images of typical h-BN domains obtained under different growth temperature are shown in Figure 4.7g. As seen from the SEM images, the domain shape changes from a concave triangle with dendritic edge to slightly convex triangle with

straight edge as the substrate temperature increases. Similar results were achieved for the h-BN growth with mixed nitrogen source as seen in Figure 4.8. In general, the growth of 2D material can be described by three sequential steps, i.e., source atoms adsorption, adatoms hopping and diffusion across adsorption sites on substrate surface, and adatoms bonding and attachment to active sites of an existing domain edge. Each step has an associated energy barrier to overcome. Besides, the adatoms desorption and edge atoms detachment also happen at the same time. Adatom diffusion and attachment/detachment can directly affect the growth of a domain edge, and, therefore, can be typical limiting factors. In a diffusion-limited growth scenario, where the diffusion of adatoms is relatively slow with a high diffusion barrier, or the attachment is relatively effective, the 2D domain usually shows a concave shape with dendritic edges due to the variation in local concentration gradient of adatoms [41]. When the attachment energy barrier is increased and/or the diffusion barrier is decreased, the growth is then shifted to attachment/detachment limited growth. The domain shape often exhibits an equilibrium shape with straight edges according to the Wulf construction. The present temperature dependent domain shape evolution results indicate the gradual transition from diffusion-limited growth mode to attachment/detachment-limited growth mode.

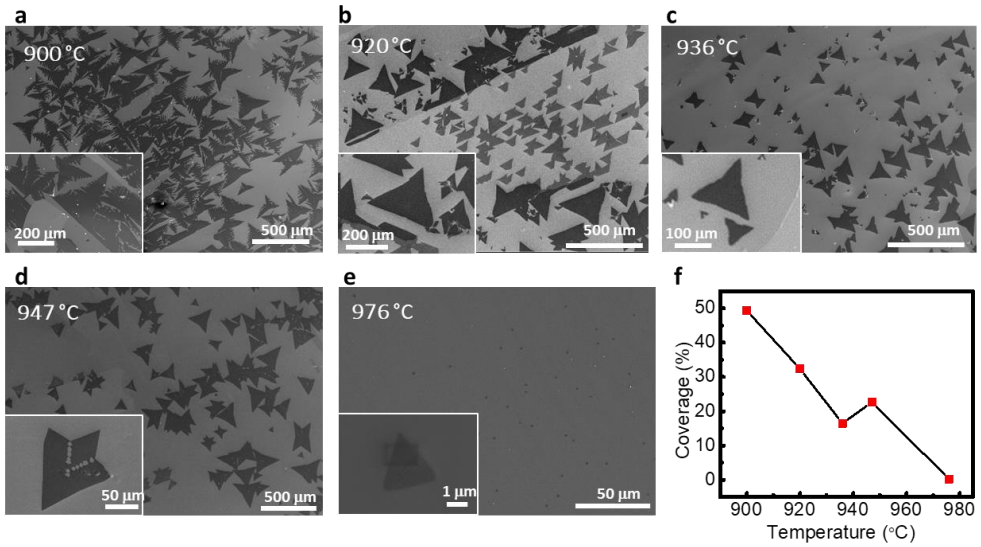

Figure 4.8 SEM image of 3-hour h-BN samples with 10-sccm N_2 plasma and 5-sccm NH_3 on 300-s carburized AGG Ni substrates at (a) 900 °C, (b) 910 °C, (c) 936 °C, (d) 947 °C, and (e) 976 °C, respectively. The insets are zoom-in images of individual flakes. (f) Plot of h-BN coverage as a function of growth temperature.

As seen from Figure 4.7f, the maximum domain size evolves with the growth temperature and the largest domain was achieved around 930 °C to be 1.4 mm (indicated in Figure 4.7c), which happens at the transition region between diffusion- and attachment/detachment- limited regions. This can be explained by the highest atomic efficiency. Further increase of the temperature leads to increased detachment/dissociation of the edge atoms, which limits the increase of the domain size. High desorption rate of B/N atoms also limits the supply of feedstock for edge attachment and limits the growth rate. The domain density remains in a low and similar level, and almost independent of temperature within a span of 60 °C (Figure 4.7f).

Precursor type and flux also have direct influence on the growth dynamics. Different N sources including pure N_2 plasma, pure NH_3 and their mixture contribute differently to the morphology of h-BN samples. Some results are shown in Figure 4.4, Figure 4.7 and Figure 4.8, and a comprehensive study of this aspect is reported elsewhere [42]. Likewise, the B flux is critical to the coverage of h-BN as well due to high desorption rate of B [11,43]. Therefore, changing B_2O_3 cell temperature will change the B flux, and, in turn, change the coverage and morphology of h-BN. As seen from Figure 4.4, the morphology changes from discrete h-BN flakes (Sample II) to continuous uniform h-BN monolayer film (Sample IV) after the B_2O_3 cell temperature increases from 1120 °C to 1130 °C. As the B_2O_3 cell temperature keeps increasing from 1130 °C to 1170 °C, besides the formation of continuous uniform h-BN monolayers, adlayers start to form and increase in density

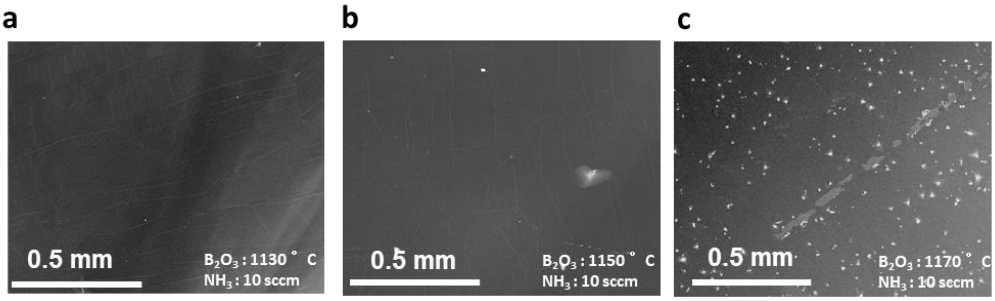

Figure 4.9 (a-c) SEM images of continuous h-BN films grown with B_2O_3 cell temperature at 1130, 1150, and 1170 °C, respectively. Other growth parameters are 910 °C substrate temperature, and 10-sccm NH_3 flow rate.

(Figure 4.9). It has been reported that the hydrogen terminated graphene edge can facilitate the intercalation growth of graphene multilayers due to the weak edge-substrate coupling [44]. Because of the same intercalation mechanism, these adlayers are local h-BN

multilayers rather than boron clusters or other forms of boron nitrides. Details about the formation and nature of these adlayers are reported elsewhere [42].

In order to study the quality of the as-grown continuous uniform h-BN monolayer, Ni(metal contact)/h-BN/Ni(foil) two-terminal devices with a metal contact size of 50×50 μm^2 based on Sample IV were fabricated. Figure 4.10 shows I-V characteristics of 25 devices, and the bottom right inset shows the distribution of corresponding breakdown voltages (V_{BD}). As seen from Figure 4.10, the devices operate under direct tunneling process at lower voltages and undergo typical soft breakdown as the bias increases to a certain voltage; the peak V_{BD} is determined to be 0.65 V from a Gaussian fit. Assuming the

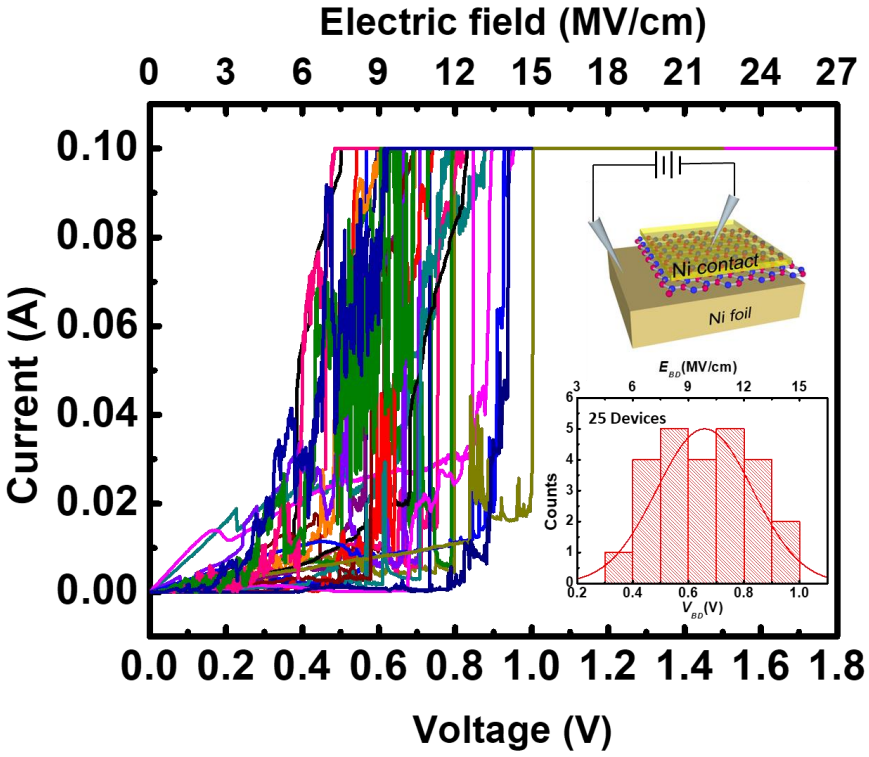

Figure 4.10 Electrical property of h-BN monolayer (Sample IV). Current-voltage characteristics of 25 Ni/h-BN/Ni capacitor devices. The upper and lower insets show the schematic of the device and the corresponding statistics of breakdown voltage (V_{BD}) and breakdown electric field (E_{BD}), respectively.

interaction between the top/bottom Ni contacts with the middle single-layer h-BN is through Van der Waals forces, the Van der Waals distance between the top and bottom Ni contacts is ~0.667 nm. Thus, the estimated average breakdown electric field is 9.75 MV/cm, which is slightly higher than the previous reported value of a 3-layer h-BN film on Co and is comparable with that of exfoliated h-BN [45], suggesting high quality of the single-layer h-BN film.

To reveal the epitaxial relationship between h-BN flakes and Ni (100) substrate, SEM imaging and EBSD analysis were combined to characterize the samples. Figure 4.11 a&b show SEM images of typical flakes at different locations of an h-BN sample. As seen from these images, most h-BN domains have one edge aligned along either [011] or $[0\bar{1}1]$ directions. This is similar to the observation that h-BN flakes have two equivalent alignments on Cu (100) surface, being along two diagonal directions [011] and $[0\bar{1}1]$, due

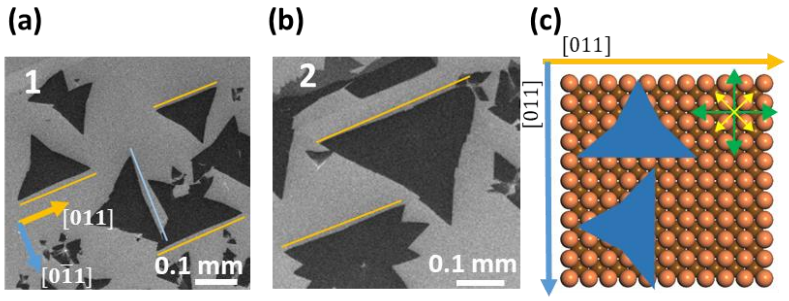

Figure 4.11 (a, b) SEM images of an h-BN sample grown on AGG Ni with 10-sccm N_2 plasma and 5-sccm NH_3, B cell temperature of 1150 °C, and substrate temperature of 910 °C for 3 h at two different location (marked as 1 and 2). Typical h-BN flake consists of one straight edge and two curved edges. Straight edges are used to identify the orientation, as indicated with orange or blue lines. The angle between blue and orange edges is ~90°. According to the SEM-EBSD, the [011] and $[\mathbf{0\bar{1}1}]$ of Ni substrate are labeled with orange and blue arrows, respectively. (c) Schematics representation of h-BN flake orientation on Ni (100) surface. The green and yellow arrows indicate the fast and slow diffusion directions, respectively.

to the fourfold symmetry of Cu (100) [46]. In addition, the domains usually consist of one straight edge and two concave edges. This is reminiscent of the 4-lobed graphene flakes grown on Cu (100) [47]. We believe the anisotropic diffusion is also responsible for this phenomenon, as the concave edge is typical for diffusion-limited growth. Figure 4.11c shows a schematic of the formation of the asymmetric h-BN domains. The fast and slow diffusion directions are indicated by green and yellow arrows, respectively. With the given alignment configuration of Ni (100) substrate, the h-BN domains have one edge aligned with the [011] family direction. This straight edge is also perpendicular to a fast diffusion direction. On the other hand, the other two edges as two growth fronts are facing the slow diffusion direction. As a result, these edges are more prone to the depletion of local adatoms supply and fall into diffusion-limited region.

Finally we briefly discuss the results from the thermal dynamics point of view. As a matter of fact, the focal point of enabling the growth of large-area single-crystal h-BN here is the incorporation of carbon interstitials into secondary recrystalized Ni (100). Our earlier effort of the growth of h-BN on carburized Co (111) substrates has already indicated the enhanced adsorption and diffusion of B and N atoms on Co (111) [11]. Since both Ni and Co are transition metals, this suggests that carbon incorporation into these substrates changes the catalytic effect of these metals. From the perspective of crystal growth, stronger catalytic effect is equivalent to smaller nucleation activation energy. The nucleation activation energy E_a is expressed as [48, 49]:

$$E_a=E_{ads}+E_{diff}+E_{att} \quad (1),$$

namely, it is related to the adsorption energy E_{ads}, diffusion activation energy E_{diff}, and nucleation barrier or energy barrier of attachment for the capture of a surface adatom by a supercritical nucleus E_{att}. As seen from Eq. (1), at a given temperature and source flux, the increase of adsorption, diffusion, and attachment, namely smaller adsorption energy (E_{ads}), diffusion energy (E_{diff}), and attachment energy (E_{att}) can promote the nucleation of h-BN. Since the attachment energy is an energy barrier for a B or N atom to overcome to attach covalently to an existing nuclei on the substrate, the attachment energies will be the same for a given transition metal with or without interstitials if the change of the lattice parameters of a metal substrate is assumed to be negligible after the incorporation of small and moderate amount of interstitials. Therefore, an understanding of the change of adsorption energy and diffusion energy before and after the incorporation of carbon interstitial can help understand the h-BN nucleation and growth on Ni here.

The adsorption energies of B and N atoms on Ni is calculated using the following expression,

$$E_{ads} = E_{B/N\ on\ surface} - E_{B/N} - E_{surface} \qquad (2),$$

where $E_{B/N\ on\ surface}$ is the total energy of a B or N atom on the surface of a supercell. $E_{B/N}$ is the chemical potential of the adsorbed B or N atom, and $E_{surface}$ is the total energy of the isolated supercell. Detailed methodology of the DFT simulation of adsorption energy is in Experimental details section. Figure 4.12a shows a summary of adsorption energies of B and N atoms onto top, hollow and bridge sites of Ni (100) with and without embedded carbon interstitials. As seen from Figure 4.12a, the adsorption energies of B and N atoms

a

Adsorption Energy eV/atom	Adsorption sites	Ni (100)	
		Pristine	With C
B	Top	4.38	3.88
	Hollow	0.65	0.62
	Bridge	2.68	2.65
N	Top	7.69	0.639
	Hollow	-2.75	-2.80
	Bridge	-1.13	-1.18

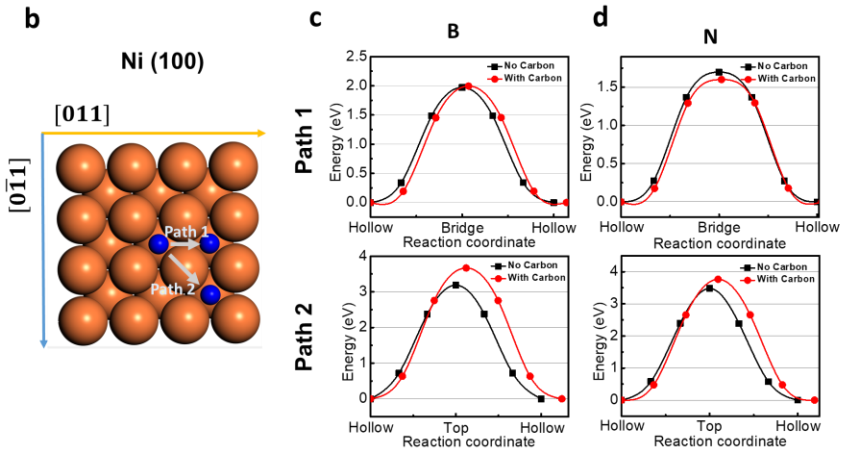

Figure 4.12 Theoretical calculation of adsorption and diffusion energies of B and N atoms on Ni (100). (a) A summary of adsorption energies of B and N on Ni (100) with and without an embedded interstitial carbon. (b-g) Reaction path from an NEB calculation showing the diffusion activation energy from one adsorption site to another. (b) Top view of a Ni (100) surface with a B or N atom adsorbed on it. Two diffusion paths are indicated with white arrows. Minimum energy path along path 1 and path 2 for (c) a B and (d) an N atom diffusing from one hollow site to the neighboring hollow site of Ni (100) surface without (black curve) or with (red curve) interstitial carbon atom.

decrease on Ni (100) after the incorporation of carbon interstitials. As a result, the activation energy reduces for carburized Ni (100).

To study the carbon interstitial effect on diffusion activation energy (E_{diff}) of B and N atoms, simulations using the climbing image nudged elastic band (CI-NEB) method were carried out. For Ni (100) substrate (Figure 4.12b), Figure 4.12c-d show the diffusion energies for both B and N atoms along two directions from one hollow site to another, denoted as path 1 and path 2 in Figure 4.12b. The diffusion barriers for both B and N along path 2 are larger than that along path 1 with or without carbon in the substrate, which confirms the hypothesis of the fast and slow diffusion directions to be path 1 and path 2, respectively. After the incorporation of carbon, the diffusion energies for B and N along path 2 are further increased while that along path 1 are almost unchanged and decreased, respectively. This suggests that although the nucleation may still take the slow diffusion path 2, it dominantly takes the fast diffusion path (path 1). Overall, the unchanged B and reduced N diffusion energies along path 1 and reduced B and N adsorption energies contribute to the reduction of nucleation activation energy, in turn, the nucleation and growth of h-BN become more efficient, leading to larger single-crystal h-BN flakes and eventually continuous high-quality monolayer films on carburized Ni (100). Finally, it should be noted that the calculated values of absorption and diffusion energies may not be absolute to represent real thermodynamic situation precisely due to relative simplification in the above simulations, such as using small supercell, considering individual atoms rather than group of atoms and their interactions, etc. However, the change of these values can

reasonably explain different nucleation and growth of h-BN on Ni (100) with and without carburization.

4.4. **Conclusion**

In conclusion, we demonstrated controllable synthesis of millimeter-size single-crystal h-BN domains through an interstitial carbon assisted approach. Interstitial C atoms in Ni (100) substrates promote B and N adsorption and push the growth into fast diffusion regions, which essentially reduces nucleation activation energy. With proper preparation of high-quality substrates, which yields large Ni (100) grains, Single-crystal h-BN monolayer domains over 1 mm were routinely obtained and a large single-crystal h-BN domain of 1.4 mm was achieved. Continuous large-area single-layer h-BN film with a high breakdown electric field of 9.75 MV/cm was also demonstrated. The growth dynamics were studied by tuning different growth parameters including substrate temperature, and B and N source fluxes. The epitaxial relationship between h-BN and substrate was studied with the assistance of EBSD mapping. The in-depth experimental analysis combined with the support of DFT simulations paves the way towards full understanding of the growth mechanism of 2D h-BN on transition metal substrates. The experimental demonstration of millimeter-sized large single-crystal h-BN domains and continuous large-area single-layer h-BN films represents a further step towards practical applications of these 2D materials.

4.5. **References**

[1] L. Song, L. Ci, H. Lu, P. B. Sorokin, C. Jin, J. Ni, A. G. Kvashnin, D. G. Kvashnin, J. Lou, B. I. Yakobson, *Nano Lett.* **2010**, 10, 3209.

[2] K. K. Kim, A. Hsu, X. Jia, S. M. Kim, Y. Shi, M. Hofmann, D. Nezich, J. F. Rodriguez-Nieva, M. Dresselhaus, T. Palacios, *Nano Lett.* **2011**, *12*, 161.

[3] M. Xu, T. Liang, M. Shi, H. *Chen, Chem. Rev.* **2013**, *113*, 3766.

[4] J. Yin, J. Li, Y. Hang, J. Yu, G. Tai, X. Li, Z. Zhang, W. Guo, *Small* **2016**, *12*, 2942.

[5] Y. Hao, M. Bharathi, L. Wang, Y. Liu, H. Chen, S. Nie, X. Wang, H. Chou, C. Tan, B. Fallahazad, *Science* **2013**, *342*, 720.

[6] Y. Gong, G. Ye, S. Lei, G. Shi, Y. He, J. Lin, X. Zhang, R. Vajtai, S. T. Pantelides, W. Zhou, *Adv. Funct. Mater.* **2016**, *26*, 2009.

[7] T. Wu, X. Zhang, Q. Yuan, J. Xue, G. Lu, Z. Liu, H. Wang, H. Wang, F. Ding, Q. Yu, *Nat. Mater.* **2016**, *15*, 43.

[8] X. Xu, Z. Zhang, J. Dong, D. Yi, J. Niu, M. Wu, L. Lin, R. Yin, M. Li, J. Zhou, *Science Bulletin* **2017**, *62*, 1074.

[9] J. Meng, X. Zhang, Y. Wang, Z. Yin, H. Liu, J. Xia, H. Wang, J. You, P. Jin, D. Wang, *Small* **2017**, *13*, 1604179.

[10] H. Tian, A. Khanaki, P. Das, R. Zheng, Z. Cui, Y. He, W. Shi, Z. Xu, R. Lake, J. Liu, *Nano Lett.* **2018**, *18*, 3352.

[11] J. S. Lee, S. H. Choi, S. J. Yun, Y. I. Kim, S. Boandoh, J.-H. Park, B. G. Shin, H. Ko, S. H. Lee, Y.-M. Kim, *Science* **2018**, *362*, 817.

[12] H. Cun, A. Hemmi, E. Miniussi, C. Bernard, B. Probst, K. Liu, D. T. Alexander, A. Kleibert, G. Mette, M. Weinl, *Nano Lett.* **2018**, *18*, 1205.

[13] L. Wang, X. Xu, L. Zhang, R. Qiao, M. Wu, Z. Wang, S. Zhang, J. Liang, Z. Zhang, Z. Zhang, *Nature* **2019**, *570*, 91.

[14] R. Y. Tay, H. J. Park, G. H. Ryu, D. Tan, S. H. Tsang, H. Li, W. Liu, E. H. T. Teo, Z. Lee, Y. Lifshitz, *Nanoscale* **2016**, *8*, 2434.

[15] M. S. Driver, J. D. Beatty, O. Olanipekun, K. Reid, A. Rath, P. M. Voyles, J. A. Kelber, *Langmuir* **2016**, *32*, 2601.

[16] Z. Xu, H. Tian, A. Khanaki, R. Zheng, M. Suja, J. Liu, *Sci. Rep.* **2017**, *7*, 43100.

[17] Y. Shi, C. Hamsen, X. Jia, K. K. Kim, A. Reina, M. Hofmann, A. L. Hsu, K. Zhang, H. Li, Z.-Y. Juang, *Nano Lett.* **2010**, *10*, 4134.

[18] A. Ismach, H. Chou, D. A. Ferrer, Y. Wu, S. McDonnell, H. C. Floresca, A. Covacevich, C. Pope, R. Piner, M. J. Kim, *ACS Nano* **2012**, *6*, 6378.

[19] S. Caneva, R. S. Weatherup, B. C. Bayer, B. Brennan, S. J. Spencer, K. Mingard, A. Cabrero-Vilatela, C. Baehtz, A. J. Pollard, S. Hofmann, *Nano Lett.* **2015**, *15*, 1867.

[20] S. M. Kim, A. Hsu, M. H. Park, S. H. Chae, S. J. Yun, J. S. Lee, D.-H. Cho, W. Fang, C. Lee, T. Palacios, *Nat. Commun.* **2015**, *6*, 8662.

[21] S. Caneva, R. S. Weatherup, B. C. Bayer, R. Blume, A. Cabrero-Vilatela, P. Braeuninger-Weimer, M.-B. Martin, R. Wang, C. Baehtz, R. Schloegl, *Nano Lett.* **2016**, *16*, 1250.

[22] R.-J. Chang, X. Wang, S. Wang, Y. Sheng, B. Porter, H. Bhaskaran, J. H. Warner, *Chem. Mater.* **2017**, *29*, 6252.

[23] Y.-J. Cho, A. Summerfield, A. Davies, T. S. Cheng, E. F. Smith, C. J. Mellor, A. N. Khlobystov, C. T. Foxon, L. Eaves, P. H. Beton*, Sci. Rep.* **2016**, *6*, 34474.

[24] A. Summerfield, A. Davies, T. S. Cheng, V. V. Korolkov, Y. Cho, C. J. Mellor, C. T. Foxon, A. N. Khlobystov, K. Watanabe, T. Taniguchi, *Sci. Rep.* **2016**, *6*, 22440.

[25] S. Nakhaie, J. Wofford, T. Schumann, U. Jahn, M. Ramsteiner, M. Hanke, J. Lopes, H. Riechert, *Appl. Phys. Lett.* **2015**, *106*, 213108.

[26] Z. Xu, A. Khanaki, H. Tian, R. Zheng, M. Suja, J.-G. Zheng, J. Liu, *Appl. Phys. Lett.* **2016**, *109*, 043110.

[27] Z. Xu, R. Zheng, A. Khanaki, Z. Zuo, J. Liu, *Appl. Phys. Lett.* **2015**, *107*, 213103.

[28] R. Zheng, A. Khanaki, H. Tian, Y. He, Y. Cui, Z. Xu, J. Liu, *Appl. Phys. Lett.* **2017**, *111*, 011903.

[29] A. Khanaki, H. Tian, Z. Xu, R. Zheng, Y. He, Z. Cui, J. Yang, J. Liu, *Nanotechnology* **2017**, *29*, 035602.

[30] T. Kusama, T. Omori, T. Saito, S. Kise, T. Tanaka, Y. Araki, R. Kainuma, *Nat. Commun.* **2017**, *8*, 354.

[31] E. Zielinski, R. Vinci, J. Bravman, *J. Appl. Phys.* **1994**, *76*, 4516.

[32] T. Omori, T. Kusama, S. Kawata, I. Ohnuma, Y. Sutou, Y. Araki, K. Ishida, R. Kainuma, *Science* **2013**, *341*, 1500.

[33] R. Wang, D. G. Purdie, Y. Fan, F. C. Massabuau, P. Braeuninger-Weimer, O. J. Burton, R. Blume, R. Schloegl, A. Lombardo, R. S. Weatherup, *ACS Nano* **2019**，*13*， 2114.

[34] S. Nakhaie, M. Heilmann, T. Krause, M. Hanke, J. M. J. Lopes, *J. Appl. Phys.* **2019**, *125*, 115301.

[35] A. Tonkikh, E. Voloshina, P. Werner, H. Blumtritt, B. Senkovskiy, G. Güntherodt, S. Parkin, Y. S. Dedkov, *Sci. Rep.* **2016**, *6*, 23547.

[36] D. Chrysostomou, J. Flowers, F. Zaera, *Surf. Sci.* **1999**, *439*, 34.

[37] X. Kong, H. Ji, R. D. Piner, H. Li, C. W. Magnuson, C. Tan, A. Ismach, H. Chou, R. S. Ruoff, *Appl. Phys. Lett.* **2013**, *103*, 043119.

[38] N. R. Wilson, A. J. Marsden, M. Saghir, C. J. Bromley, R. Schaub, G. Costantini, T. W. White, C. Partridge, A. Barinov, P. Dudin, *Nano Research* **2013**, *6*, 99.

[39] C. Elias, P. Valvin, T. Pelini, A. Summerfield, C. Mellor, T. Cheng, L. Eaves, C. Foxon, P. Beton, S. Novikov, *Nat. Commun.* **2019**, *10*, 2639.

[40] J. Han, J.-Y. Lee, H. Kwon, J.-S. Yeo, *Nanotechnology* **2014**, *25*, 145604.

[41] J. Dong, L. Zhang, F. Ding, *Adv. Mater.* **2018**, *31*, 1801583.

[42] Y. He, H. Tian, A. Khanaki, W. Shi, J. Tran, Z. Cui, P. Wei, J. Liu, *Appl. Surf. Sci.* **2019**, 143851.

[43] J. A. Rodriguez, C. M. Truong, J. S. Corneille, D. W. Goodman, *J. Phys. Chem. A* **1992**, *96*, 334.

[44] H. Shu, X. Chen, F. Ding, *Chemical Science* **2014**, *5*, 4639.

[45] Y. Hattori, T. Taniguchi, K. Watanabe, K. Nagashio, *ACS Nano* **2014**, *9*, 916.

[46] G. E. Wood, A. J. Marsden, J. J. Mudd, M. Walker, M. Asensio, J. Avila, K. Chen, G. R. Bell, N. R. Wilson, *2D Mater.* **2015**, *2*, 025003.

[47] D. H. Jung, C. Kang, J. E. Nam, H. Jeong, J. S. Lee, *Sci. Rep.* **2016**, *6*, 21136.

[48] T. Li, C. Liu, Z. Zhang, B. Yu, H. Dong, W. Jia, Z. Jia, C. Yu, L. Gan, B. Xu, *Nanoscale Res. Lett.,* **2018**, *13*, 130.

[49] R. Yue, Y. Nie, L. A. Walsh, R. Addou, C. Liang, N. Lu, A. T. Barton, H. Zhu, Z. Che, D. Barrera, *2D Mater.* **2017**, *4*, 045019.

[50] J. P. Perdew, K. Burke, M. Ernzerhof, *Phys. Rev. Lett.* **1996**, *77*, 3865.

[51] M. Ernzerhof, G. E. Scuseria, *J. Chem. Phys.* **1999**, *110*, 5029.

[52] G. Kresse, J. Hafner, *Phys. Rev. B* **1993**, *47*, 558.

[53] G. Henkelman, B. P. Uberuaga, H. Jónsson, *J. Chem. Phys.* **2000**, *113*, 9901.

Chapter 5 Large-area Adlayer-free Single-layer h-BN Film Achieved by Controlling Intercalation Growth

5.1. Introduction

Since the isolation of single-layer graphene in 2004 [1], 2D materials have been intensively investigated, resulting in many novel devices that have unparalleled performances [2-6]. Many of these applications require precise control of film thickness. For example, single layer film may act as perfect encapsulation or insulation for other 2D materials, while multilayer film is used as excellent tunneling barrier or robust field-effect dielectric for tunneling devices and transistors, respectively. Further accurate control of the number of atomic layers in vertical heterostructures also potentially maximizes the performance of the devices based on these structures. However, while progress has been made in the scalable growth on several catalyst metal substrates [7-13], the precise control of its thickness has remained a great challenge. Non-uniform adlayers in h-BN growth are frequently observed, which compromise the uniformity and flatness of films. Thus, understanding of the formation of adlayers can provide insight into the growth of uniform 2D layers. Specifically, single-layer film can be achieved if adlayer growth is eliminated. In contrast, large multilayer film can be achieved if each layer of the adlayer seeds can grow uniformly in the lateral direction.

To date, the growth mechanism of adlayers remains elusive. One proposed mechanism suggests that sequential layers grow on top of existing layers with an assistance of defective nucleation sites [14], while others suggest that sequential layers grow underneath through intercalation[15] or precipitation [16]. Similar debate exists in graphene growth for a long

time. Some propose that sequential graphene layers grown on top originate from multilayer seed [17]. For example, Kidambi *et al*. reported on-top growth mechanisms by using hydrogen etching [15]. On the other hand, Li *et al.* demonstrated that the second layer grows underneath the first layer on Cu foil by carbon isotope labeling [18]. Also in graphene/h-BN heterostructure growth, intercalation growth of graphene under h-BN cover on Ni substrate was directly observed by *in situ* LEEM [19]. On the other hand, direct growth of graphene on exfoliated h-BN was also achieved under an extremely high growth temperature of 1850 °C [20]. Thus, whether sequential layers grow on top or from bottom depends on the growth conditions and techniques used.

2D h-BN layers are synthesized using various methods such as atomic layer deposition (ALD) [21-23], chemical vapor deposition (CVD) [10, 26, 24-28], and molecular beam epitaxy (MBE) [29-36]. Each one has its own merits. For example, the ALD technique can produce h-BN films with relatively high quality at low growth temperature. Low-temperature process is important for some device applications. CVD process usually requires high temperature to decompose gaseous sources, but it is relatively simple, thus perhaps it is the most popular method. As an alternative, MBE is versatile for the synthesis of 2D h-BN due to its great controllability of growth parameters and in situ atomic-layer monitoring technique such as reflection high-energy electron diffraction (RHEED). In our recent paper regarding the MBE growth of 2D h-BN films on carburized Co and Ni substrates, we demonstrated that subsurface carbon interstitials enhance the absorption and diffusion of B and N atoms on the surface for promoting the h-BN growth [37]. Here, we focus on a study of the growth of h-BN adlayers. We used two different nitrogen sources,

namely nitrogen plasma and ammonia to study the influence of hydrogen atoms; used polycrystalline Co, polycrystalline Ni, and single crystalline Ni substrates to study the influence of substrate crystallographic defects; and used different substrate carburization time to study the interstitial carbon effect. The samples were characterized by X-ray photoelectron spectroscopy (XPS), atomic force microscopy (AFM), Raman spectroscopy, scanning electron microscopy (SEM), and transmission electron microscopy (TEM). By optimizing these growth parameters, we achieved the growth of a large-area adlayer-free single-layer h-BN film, and thus this study provides a strategy towards uniform h-BN 2D film growth.

5.2. **Experimental details**

A Perkin-Elmer MBE system with a background pressure of ~10^{-9} Torr was used for the sample growth. Boron was supplied by a Knudsen effusion cell filled with B_2O_3 powder (Alfa Aesar, 99.999% purity), which is heated up to around 1150 °C. Nitrogen plasma was produced by introducing nitrogen gas (Airgas, 99.9999% purity) through an electron cyclotron resonance (ECR) nitrogen plasma generator. ECR current was set at 60 mA with a power of 228 W. Ammonia (American Gas Group, 99.9995% purity) was introduced independently through another channel. Gas flow rate of each nitrogen source is limited up to 10 sccm by a mass flow controller (MFC), and total gas flow rate is limited up to 15 sccm by the turbo pump ability. Before growth, Co and Ni substrates with a size of 1 cm × 1 cm, a thickness of 0.1 mm, and a purity of 99.995% were mechanically polished, then

cleaned with acetone, IPA and diluted hydrochloric acid (10%), and deionized (DI) water. All samples were grown at a substrate temperature of 900 °C. Without specific notification, the growth on Ni lasts 6 h, and on Co lasts 3 h.

SEM images were acquired using a FEI NNS450 system in secondary electron (SE) imaging mode with a beam voltage of 10 kV. Raman characterizations were performed using a HORIBA LabRam system equipped with a 60-mW, 532-nm green laser. AFM images were obtained using a Veeco D5000 AFM system. TEM images and selected area electron diffraction (SAED) patterns were acquired using a FEI Tecnai12 system. TEM sample was prepared by picking a transferred h-BN film using a 200-mesh Cu grid covered with holey carbon film with orthogonal array of 1.2-μm diameter holes. XPS characterization was conducted using a Kratos AXIS ULTRA XPS system equipped with an Al Kα monochromatic X-ray source and a 165-mm mean radius electron energy hemispherical analyzer. The fitting of XPS data was performed using CasaXPS software.

5.3. **Results and discussion**

We performed experiments based on three major growth factors, namely hydrogen, substrate type, and substrate carburization level. Figure 5.1(i) and (ii) show two rows of SEM images of as grown films using different "N_2 plasma + ammonia" mixture,

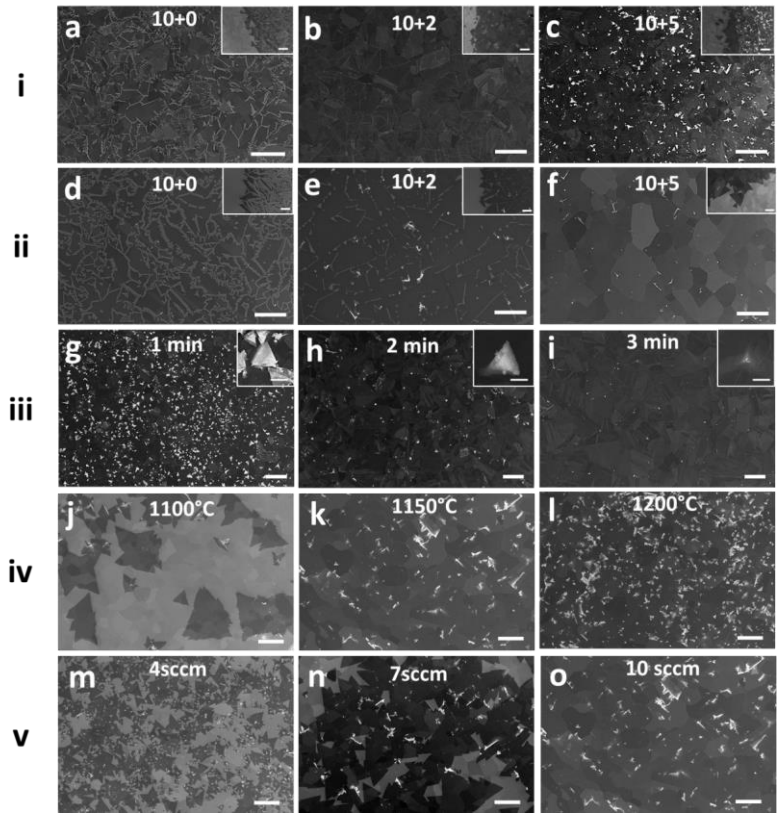

Figure 5.1 SEM images for morphology evolution of h-BN at different growth condition. (i) and (ii) are samples grown with different "N_2 plasma + ammonia" mixture on Co and Ni, respectively. Insets are SEM images taken near the edge. The numbers on SEM images stand for gas flow rate (sccm). (iii) are samples grown with different carburization time on Co. Insets are close-up of adlayers. The scale bar for insets in (h), (i), and (j) are 50 μm, 25 μm, and 10 μm, respectively. C_2H_2 gas flow rate used for carburization is also 0.5 sccm, and the nitrogen mixture is 10+5. (iv) are samples grown with different boron source temperature on Ni with 10 sccm ammonia. (v) are samples grown with different gas flow rate of ammonia with boron cell kept 1150 °C. For samples in (i), (ii), (iii), and (iv), the substrates were carburized with 0.5-sccm C_2H_2 for 1 min before growth. All samples were grown with substrate temperature kept at 900 °C. Growth time on Co is 3 h, while growth time on Ni is 6 h. All the scale bars are 200 μm.

respectively. The numbers on the SEM images stand for the gas flow rates (sccm) of N_2 plasma and ammonia, respectively. While the samples in Figure 5.1(i) were grown on polycrystalline Co, those in Figure 5.1(ii) were grown on polycrystalline Ni. Thin h-BN film appears to be darker than bare metal surface due to the attenuation effect, while thick h-BN adlayers appear to be bright due to charging effect [38]. Before growth, the substrates were annealed at 900 °C in hydrogen environment for 20 min to remove native oxide layers, then carburized with 0.5-sccm C_2H_2 for 1 min to promote the adsorption and diffusion of B and N atoms [37]. Immediately after these substrate treatments, the growth for all h-BN samples took place by introducing B sources from a B_2O_3 effusion cell at 1150 °C and N mixture sources at a substrate temperature of 900 °C. Samples grown on Ni last 6 h, and on Co last 3 h. After the growth, the substrate was cooled to room temperature at a rate of about 10 degree/min. Other growth details are described in the Methods. Clear h-BN morphology transformation was demonstrated in the images from left to right on both Ni and Co substrates, as more adlayers appear with the increased amount of ammonia. However, there are fewer adlayers on Ni than on Co under the same growth conditions, therefore the h-BN morphology transformation on Ni is less drastic. Figure 5.1(iii) shows SEM images of films grown on Co with different carburization time. For this batch of samples, the nitrogen source of "10+5" mixture was used. As shown in Figure 5.1(iii), while continuous 2D h-BN films have been formed in all samples, introducing more carbon into Co results in fewer adlayers. Similar change of the adlayer density with the level of

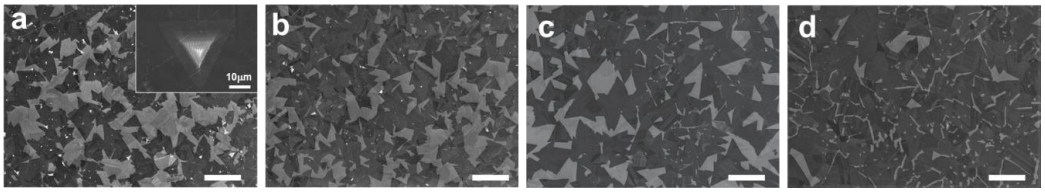

Figure 5.2 SEM images of h-BN grown with different carburization time of: (a) 1 min; (b) 2 min; (c) 3 min; (d) 4 min; growth time of these four sample is 1 h. All scale bars are 200 μm.

carburization is also observed for the samples grown using shorter growth duration of 1h (Figure 5.2). With the same carburization, nitrogen and boron source flux rates also have influence on the growth of adlayers. Figure 5.1(iv) shows SEM images of samples grown with different B_2O_3 effusion cell temperature and the same 10-sccm ammonia. Figure 5.1(v) shows SEM images of samples grown with different ammonia flux and the same B_2O_3 effusion cell temperature of 1150 °C. All these samples were grown at 900 °C for 6 h with 1-min carburization of Ni. As can be seen, increasing the source flux rate of either boron or nitrogen results in larger coverage at the same growth duration, which indicates larger growth speed. Meanwhile, adlayers appear in all samples, and their density increases with the increase of source flux rate.

Before discussing how these three factors influence the morphology of adlayers, we briefly discuss how the adlayers may have been formed in our case, namely, whether the adlayers are formed by growing sequential layers from top of or underneath existing layers. In general, growth without metal surface catalysis requires extreme growth conditions, such as high partial pressure (e.g. ambient pressure) [39], high temperature [20, 40, 41], or special technique [42] to overcome the activation barrier, and the resulted films often have low coverage and uniformity [43]. On the other hand, direct growth on transition metal

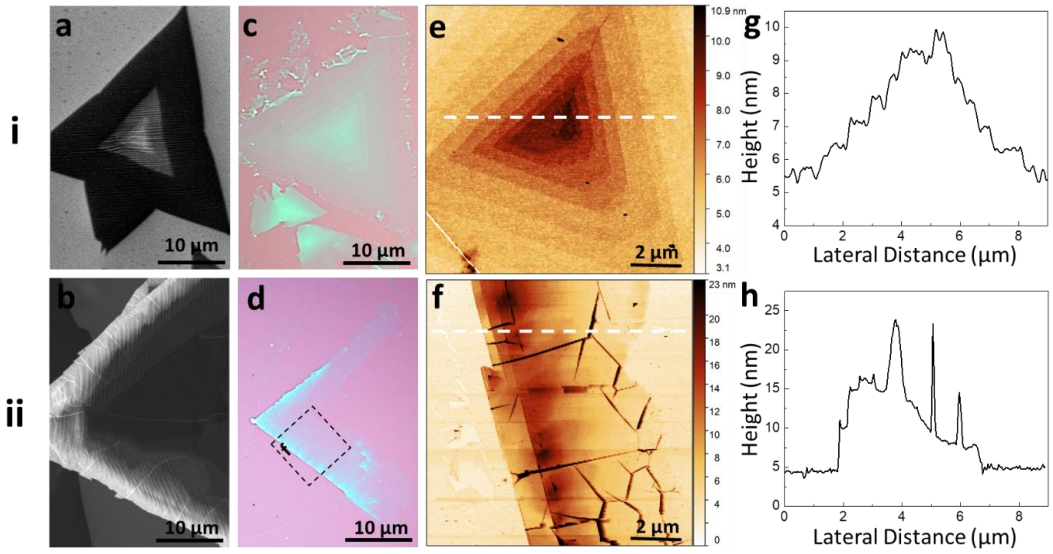

Figure 5.3 Configuration of adlayers with (i) and without (ii) a nucleation site in the center. (a/b) SEM images of adlayers on as grown sample; (c/d) Optical microscope images of adlayers after transferred onto SiO_2/Si substrate; (e/f) AFM images of adlayers after transferred onto SiO_2/Si substrate; (g/h) Height profile taken along white dashed lines in e/f, respectively.

surface can be achieved at much lower temperature with higher coverage due to a reduced activation barrier by catalytic effect. Since the growth temperature we used is very low (900 °C), it is unlikely to trigger the growth of h-BN on top of the non-catalyzing surface. Till now, two growth mechanisms were reported for the growth-from-below scenario, namely, precipitation (or segregation) and intercalation. Precipitation growth refers to the segregation of source atoms from catalyst substrate, which requires a large solubility of precursor [44-47] and a tendency to form metastable carbide (for graphene growth) [48, 49]. On the other hand, intercalation growth is caused by the diffusion of source atoms into the film/substrate interface, which is reported to be related to edge atom state [50, 51] and interface binding [19]. Although B solubilities in Ni (~0.3 at. % at 1085 °C [52]) and Co (~0.3 at. % at 1110 °C [53]) are considerably large, N solubilities in these metals are

reported to be extremely low (in Ni, ~0.004 at. % at 1550 °C [54]; in Co, ~0.017 at. % at 1600 °C [55]). Thus, those adlayers should be most probably formed by intercalation, instead of precipitation.

Since adlayers are formed from below, the growth of adlayers can be influenced mainly by two processes: one is the nucleation process; the other is the intercalation process. The growth of adlayers requires both a nucleation site to start the growth and a path for source supply in the interface. We first discuss how the nucleation process influences the adlayer growth. The detailed structures of adlayers are shown in Figure 5.3. Two kinds of adlayers are observed. Figure 5.3(i) shows the configuration of "prism-adlayers" with a preferential nucleation site in the center, and Figure 5.3(ii) shows the configuration of "ribbon-adlayers" with preferential nucleation sites along the edges. The SEM images shown in Figure 5.3 a/b are taken on as grown samples, with brighter area corresponding to thicker area. Figure 5.3 c/d show optical microscope images of the transferred adlayers on SiO_2/Si, indicating clear thickness distribution. On "prism-adlayers", a defective nucleation site is always found in the center, as resolved by the AFM image in Figure 5.3e. The line profile in Figure 5.3g, which was taken across the adlayer further shows the protrusion in the center and h-BN steps around it. The narrow peaks are caused by wrinkles on h-BN. On the other hand, no discernable nucleation site is observed on "ribbon-adlayers", as shown in the AFM image of Figure 5.3f. The line profile in Figure 5.3h shows the decreased thickness towards the center of the flake (right hand side).

The “prism-adlayers” may originate from crystallographic defects and impurities on substrate surface, where the high surface energy is beneficial to h-BN nucleation process [14]. Multilayer seeds might form at the beginning of the growth, however, the upper layers with outer edges receive more resources than inner layers, which results in different lateral growth speeds, leading to the formation of prism-like structures. The inner layer will stop growth once it is too far away from the outmost edges, or the outmost edges merge with other flakes, which stops the intercalation process. On the other hand, the “ribbon-adlayers”

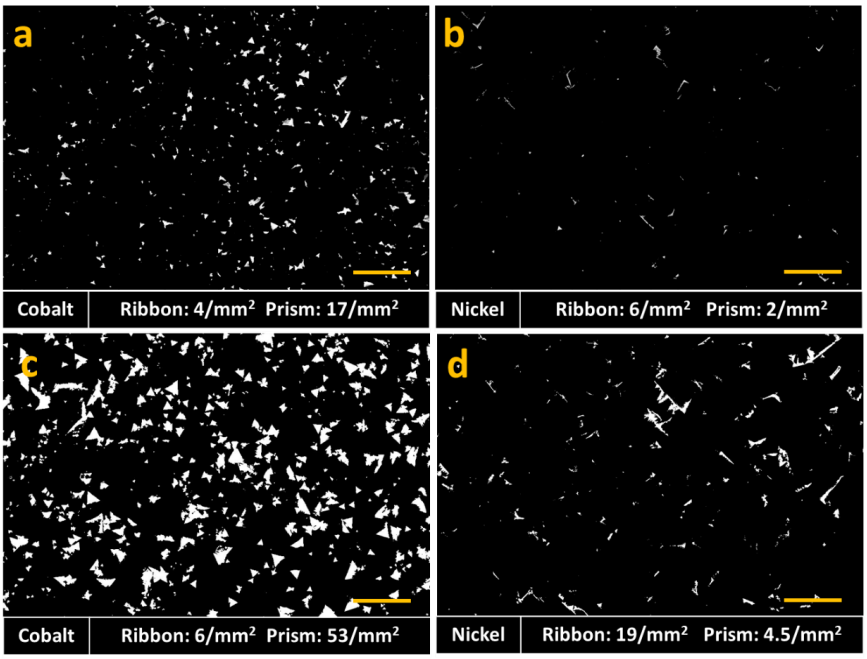

Figure 5.4 Statistical results of adlayers on Co and Ni substrate. (a/c) Counting of adlayers on Co substrate; (b/d) Counting of adlayers on Ni substrate. All scale bars are 200 μm and the areas for all four samples are 2 mm × 4/3 mm.

are likely formed during the h-BN flake expansion. The specific reason of this kind of adlayer growth is not clear, nevertheless, it may be related to the changes of atom arrangement on substrate surface. As h-BN edges reach those regions with different atom

arrangement during growth, mismatch is formed due to the loss of epitaxial relationship between h-BN film and substrate. The mismatch results in weaker binding areas where more intercalation happens [19]. B and N sources intercalate and accumulate in the confined interface, and subsequently nucleate to form atom rings and clusters, which later grow into extra layers. Similar nucleation process was reported in graphene growth [56].

As seen from Figure 5.1, even though these two kinds of adlayers coexist on every

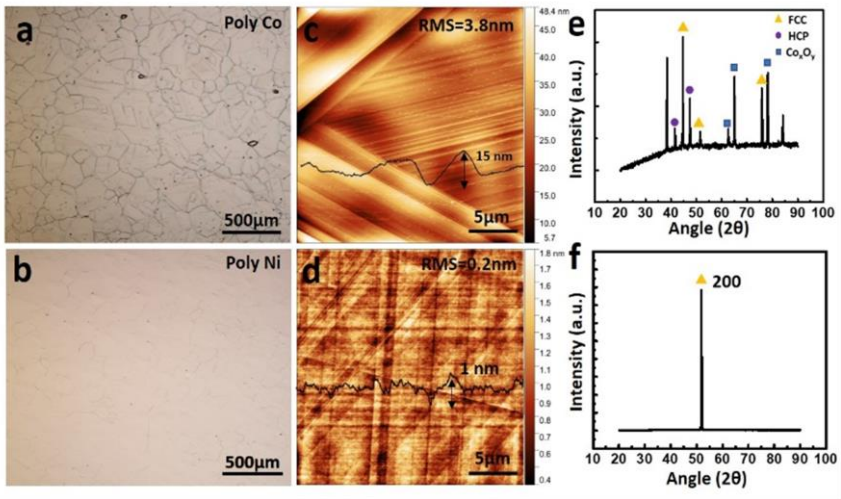

Figure 5.6 Characterization of polycrystalline Co and Ni substrates. (a/b) Optical microscope images, (c/d) AFM images, and (e/f) XRD results of Co and Ni substrates, respectively; The substrates were polished and annealed in hydrogen environment at 900 °C for 3 h.

sample with adlayers, “prism-adlayers” are dominant on Co substrate, while “ribbon-adlayers” dominate on Ni surface. These adlayers can be clearly identified by using ImageJ software, and their statistical results are summarized and shown in Figure 5.4. Co and Ni are quite similar in terms of their catalytic effect [57] and B/N solubilities. However, their surface morphology is quite different after heat treatment (Figure 5.6). More crystallographic defects (twin boundaries, terraces, large steps, etc.) form on Co surface

than on Ni surface, which may be related to the special phase transformation of Co between HCP and FCC phases [58]. The Co surface also has worse facet uniformity, as it consists of various lattice planes. Besides FCC (111), (200), (220), there are also HCP planes. On the other hand, Ni surface is dominated by FCC (100) plane. This observation further confirms that "prism-adlayers" are related to crystallographic defects and impurities. Meanwhile, more adlayers are formed on polycrystalline Co substrate than on polycrystalline Ni substrate at the same growth condition, which may be due to the formation of more multilayer seeds on Co.

Figure 5.5 shows SEM images of a sample, which was grown using the same growth conditions as the sample shown in Figure 5.1k or 5.1o, further revealing different adlayer growth scenarios. As shown in Figure 5.5a, more adlayers appear on polycrystalline region (upper right) than on single crystalline region (lower left), which illustrates the strong influence of crystallographic defects in adlayer growth. Figure 5.5 b/c are adlayers grown around dents and grooves (grain boundaries) on substrate surface. Except for the adlayers directly caused by crystallographic defects, some adlayers are formed due to the intercalation near edges, such as line defects (Figure 5.5d) and edges of flakes (Figure 5.5e). The existence of small amount of adlayers on single crystalline region is mainly caused by impurities, as shown in Figure 5.5f.

Next, we discuss how hydrogen and interstitial carbon influence the intercalation process. During the growth, N precursor is provided from two sources, namely, N_2 plasma and ammonia. While N_2 plasma is atomic source, ammonia can be regarded as molecular source.

The N_2 plasma generated by ECR plasma generator consists of N_2, N_2*, N_2+, N+, N, and e-, among which only N+ (neutralizes once reaching the grounded substrate surface) and N can bond with B atom and contribute to h-BN growth. On the other hand, ammonia undergo stepwise dehydrogenation on hot metal surface, which results in NH_2, NH radicals, and N and H atoms [59]. By using different mixture of N_2 plasma and ammonia, we observed the h-BN morphology transformation from smooth sub-monolayer to non-uniform multilayer growth. As shown in (i) and (ii), when pure N_2 plasma was used as N source (Figure 5.1 a/d), as grown h-BN film is uniform without any adlayers. However, dendritic gaps (1 μm to 8 μm wide) are formed between adjacent h-BN flakes all over the surface, which do not merge even after the growth time reaches 4.5 h for the samples grown on Co (Figure 5.7). Dendritic edge has been widely reported in graphene growth, which is believed to originate from the competition between adatom diffusion along island edges and adatom surface diffusion [60]. When surface diffusion is much faster, edge atoms cannot relax efficiently to find energetically more favorable locations along island edges before additional adatoms migrate by surface diffusion to join them, resulting in dendritic edges. However, our time dependent growth shows that isolated flakes are in well-defined triangle shape with straight edges (Figure 5.7a), which indicates fast edge atom diffusion rate. Only when those edges of adjacent flakes approach closer, twig-like gaps are formed. The resistance to merge may be related to the bombardment effect of N_2 plasma. According to ECR plasma studies, N_2+ and N+ ions have kinetic energy ranging from 6 eV to 30 eV due to the so-called Sheath potential, which is resulted from ambipolar diffusion of ions and electrons [61]. Ions with this kinetic energy have been used for poly-Si etching, and

are able to damage GaN epilayer [62]. The bombardment effect of N_2 ECR plasma on h-BN was directly proved by comparing the h-BN films grown on both front and back sides of a substrate followed by the plasma exposure as detailed in Figure 5.8 a-f.

When 2-sccm ammonia was introduced in addition to 10-sccm N_2 plasma, the gaps begin to sew up (Figure 5.1 b, e). Since the growth pressure (2×10^{-4} Torr) did not change much, the alleviation of the plasma's bombardment effect due to mean free path change can be ignored. Instead, the "sewing effect" may be caused by hydrogen. Hydrogen atoms

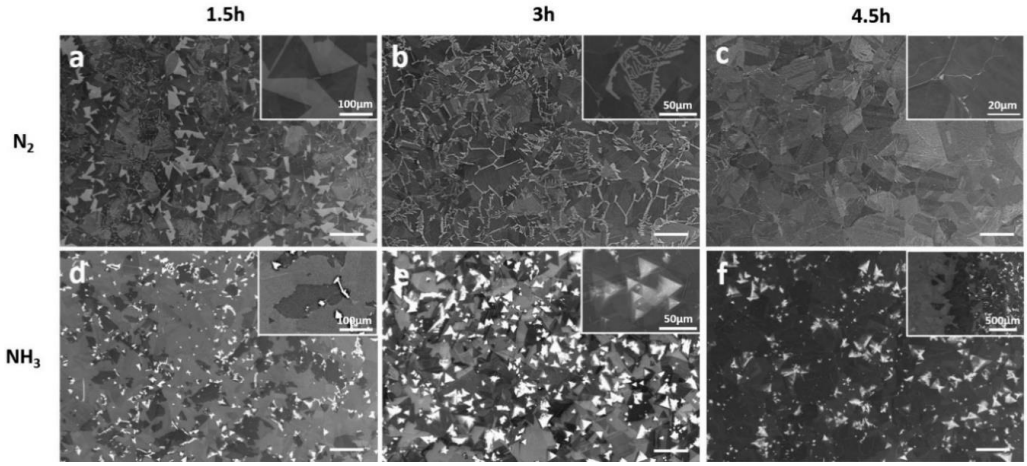

Figure 5.7 SEM images of as grown h-BN on Co substrates. (a/b/c) samples grown with 10-sccm N_2 plasma for 1.5 h, 3 h, and 4.5 h, respectively; (d/e/f) samples grown with 10-sccm ammonia for 1.5 h, 3 h, and 4.5 h, respectively. Black features are thin h-BN film, and white features are thick h-BN adlayers. All the scale bars are 200 μm. Insets are zoom in images.

are known to have strong influence in graphene growth. For example, the graphene crystal patterns can be tailored by adjusting CH_4/H_2 ratio [60]; the formation of single and bilayer graphene is closely related to the presence of hydrogen [51]; super large single-crystalline graphene domain can be achieved by removing hydrogen atoms on growing edges [63]. Similar to graphene growth, hydrogen atom can also terminate h-BN edge [64, 65]. The

presence of hydrogen on h-BN edges can be inferred from the irregular shape of h-BN domains formed when using pure ammonia as N precursor (Figure 5.7d). Hydrogen termination results in lower edge atom diffusion rate, thus edge atoms cannot relax sufficiently to find energetically more favorable locations along island edges before additional B/N atoms migrate by surface diffusion to join them. In the absence of such relaxation, irregular edges are formed [66, 67]. The presence of hydrogen atoms on growing edges could have alleviated the plasma's bombardment effect, so as to make the edges easier to merge. On the other hand, the presence of hydrogen on growing edges may also be responsible for the lower lateral growth rate when using ammonia, as shown in the time-dependent growth results in Figure 5.7. For the same growth time, using ammonia results in lower coverage than using N_2 plasma. Additional activation energies are needed to release hydrogen species from hydrogen terminated edge atoms and/or hydrogen-contained incoming precursors to form h-BN [63], resulting in lower growth rate.

Adlayers were formed when more ammonia was introduced (Figure 5.1c/f). As discussed above, these adlayers should be formed from below by intercalation. In graphene growth, people had reported that hydrogen atoms terminating the growing edges could result in the intercalation growth of adlayers [50, 51]. Here we propose a similar intercalation model, in which the density of B/N atoms in the interface (n_{in}) is proportional to the penetration probability j_{pnen} (possibility of atoms penetrate through the edge) and the density of B/N atoms outside the edge (n_{out}). j_{pnen} is a factor related to the activeness of h-BN edges, which is determined by the activation energy barrier for h-BN growth. The more

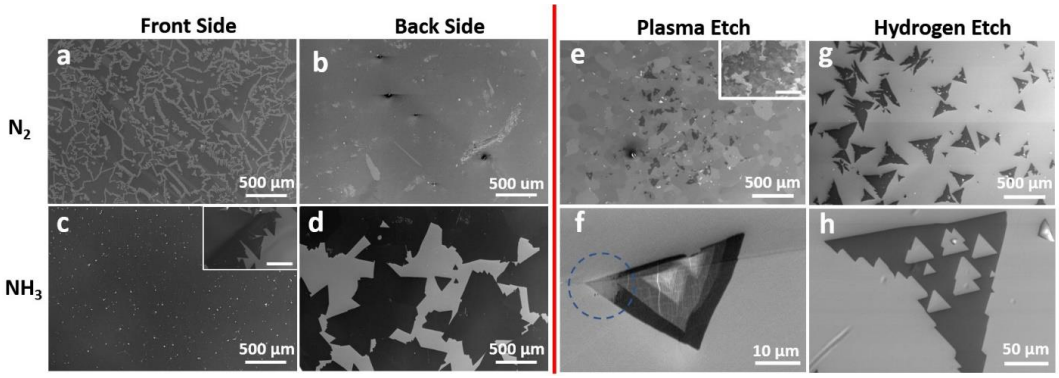

Figure 5.8 SEM images of as grown h-BN on Ni substrates. (a/b) Front and back side of as grown sample using 10-sccm nitrogen plasma; (c/d) front and back side of as grown sample using 10-sccm ammonia; the scale bar of inset image in (c) is 500 µm; (e) front side of 5-min-plasma-etched sample grown with 10+5 mixture; the inset shows backside of the sample with a scale bar of 500 µm; (f) close-up of an h-BN flake in (e); (g) 5-min-hydrogen-etched sample grown with 10+5 mixture; (h) close-up of an h-BN flake in (g). All samples were grown at 900 °C with 1-min carburization, and the B_2O_3 effusion cell kept at 1150 °C.

active the edges are, the more likely that upcoming atoms get caught and contribute to the lateral growth, thus the less likely these atoms penetrate into the interface. n_{out} is related to source flux rate and adsorption coefficient on catalyst substrate. Larger source flux rate and adsorption coefficient would result in larger n_{out}. By passivating the edges with hydrogen, we actually increase the j_{pnen}, thus more B/N atoms end up in the interface, and in turn, adlayers grow. In a hydrogen-free environment (N_2 plasma as N source), the growing edges with unpaired dangling bonds are very active and readily catch upcoming B and N atoms, thus the j_{pnen} is small, leading to no adlayer growth. It is worth noting that potential use of the mixture of hydrogen and nitrogen gas as N source cannot replace the role of ammonia because pure hydrogen gas strongly etches h-BN (Figure 5.8 g/h).

Interstitial carbon embedded in the substrate affects the adlayer growth as well. The amount of interstitial carbon was controlled by the introduction time of C_2H_2 treatment of

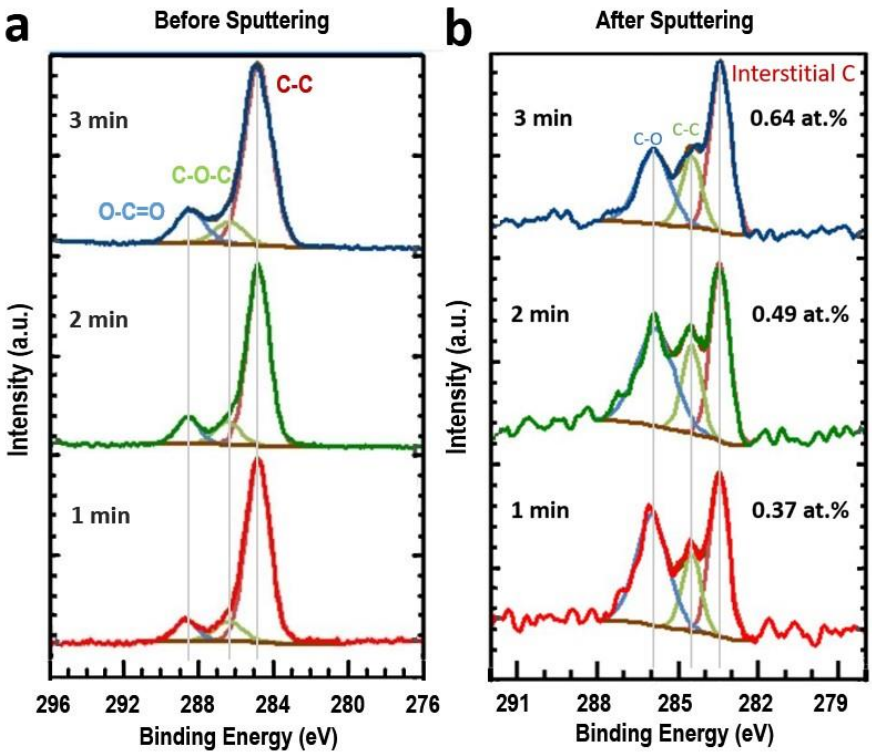

Figure 5.9 XPS characterization of C_1s on samples with 1-min, 2-min, and 3-min carburization. (a) Before sputtering; (b) and after sputtering. As the carburization time increases, the subsurface carbon concentration increases.

hot substrates prior to h-BN growth, and longer carburization time led to higher density of interstitial carbon in the substrate, as revealed by XPS studies. Figure 5.9 shows XPS spectra of C_1s on samples with different carburization time as shown in Figure 5.1(iii). As-measured XPS data was first deconvoluted, and fitted with Shirley background and GL(30) line shape. The spectrum was then calibrated by shifting C-C main peak to 284.8 eV. As shown in Figure 5.9a, the C_1s signal was dominated by adventitious carbon before sputtering, with C-C/C-H peak at 284.8 eV, C-O-H/C-O-C at 286.3 eV, and O-C=O at 288.5 eV, respectively. Even with different carburization time, no discernable differences were observed before sputtering. Figure 5.9b shows the C_1s peak after 60-s Ar+ ion

sputtering. From bottom to up, these are the profiles for 1-min, 2-min, and 3-min carburized samples, respectively. After sputtering, the dissolved interstitial carbon peak at 283.6 eV is resolved [68, 69]. The other two small peaks at 284.8 eV and 286.3 eV are assigned to residual adventitious C-C/C-H and C-O-H/C-O-C carbon, respectively. Precipitated carbon onto grain boundaries may also contribute to the peak at 284.8 eV. No sp^2 C-C bond and Ni-C bond signals are detectable within the limit of the XPS system, suggesting no graphitic or graphene structures have been formed. Based on the depth resolved XPS data, we calculated the interstitial carbon concentration. It was found that the atomic percentage for 1-min, 2-min, and 3-min carburization is 0.37 at.%, 0.49 at.%, and 0.64 at.%, respectively. However, since the depth resolved XPS data were obtained at room temperature, the real carbon concentration at the growth temperature may be different. According to the first-principles calculation, the subsurface carbon concentration in Ni can be as high as 50 at.% before carbon atoms diffuse deep into the bulk [70], thus the carbon concentration at subsurface during growth should be proportional to carburization time.

As shown in Figure 5.1 (iii), increasing the carburization time suppresses the growth of adlayers. Our previous work indicates that interstitial carbon atoms at the subsurface octahedral sites can enhance the absorption of B and N atoms on Co and Ni substrates and increase the h-BN growth speed [37]. The increased growth speed can be caused by increased source supply (n_{out}), since the absorption of B and N atoms on the surface is enhanced. It may also be caused by improved catalytic activities of the transition metals under the interstitial carbon incorporation, which results in smaller activation energy barrier for the nucleation and growth of h-BN. In other words, h-BN edges are more active

in catching upcoming B and N atoms and the growth becomes faster. To elucidate how interstitial carbon exactly works, we campare it to the source flux dependent growth (Figure 5.1(iv) and 5.1(v)), where only n_{out} is changed. As stated earlier, the increase of source flux results in the increase of growth rate. However, the amount of adlayers is also increased. This can be understood based on the intercalation model as discussed above. Since j_{pnen} remains unchanged, the increase in n_{out} results in more B and N atoms in the interface, thus more growth of adlayers. On the other hand, the increase of the amount of interstitial carbon also results in larger growth speed, however, the amount of adlyers decreases (Figure 5.2). This suggests that interstitial carbon does not increase h-BN growth rate simply by increasing the abosortion of B/N on the surface (increase of n_{out}). It improves the catalytic effect of the substrate as well. With improved catalytic effect, not only adsorption and diffusion of B and N atoms enhance 37], but also the h-BN edges are much more ready to catch upcoming B/N atoms, therefore j_{pnen} decreases, and fewer B/N atoms end up in the interface.

So far, we have discussed the factors influencing the growth of h-BN adlayer, including substrate crystallographic defects, hydrogen, and interstitial carbon. While substrate crystallographic defects have strong influence on the nucleation process,

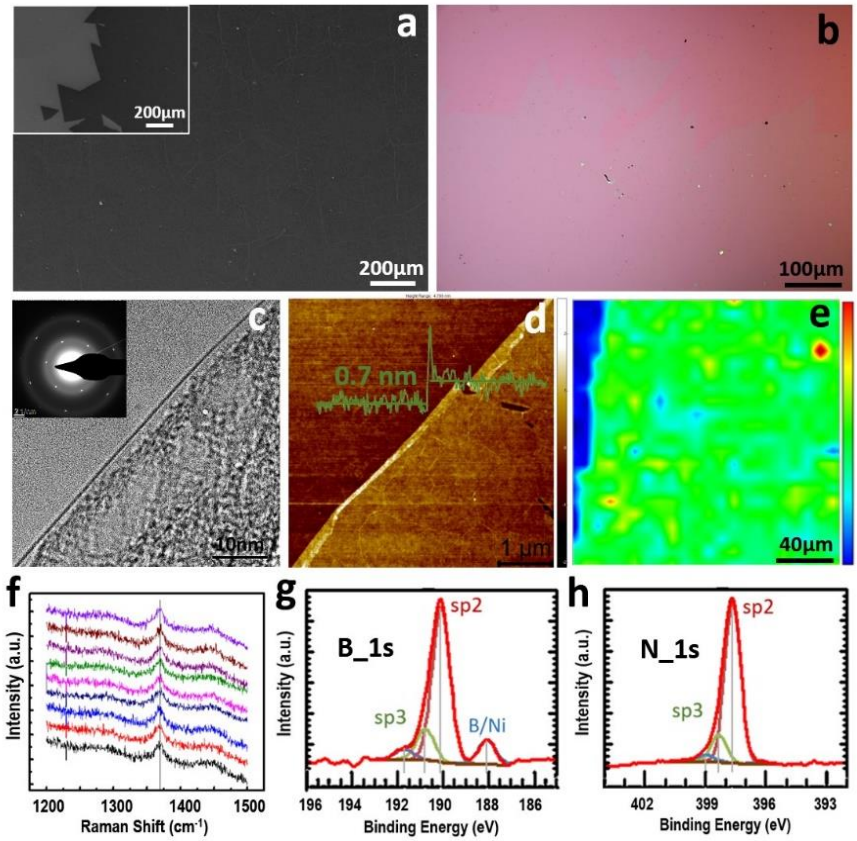

Figure 5.10 Characterization of single-layer h-BN film grown on Ni. (a) SEM image of as grown sample, with the inset showing edge area of film; (b) Optical microscope image of the sample after transferred onto SiO_2/Si substrate; (c) TEM image of the sample after transferred onto TEM grid, with inset showing the SAED pattern; (c) AFM image taken on the transferred sample; (d) Raman mapping of h-BN characteristic peak on the transferred sample; (f) 9 random Raman spectra extracted from (e); (g) XPS spectrum of B_1s; (h) XPS spectrum of N_1s.

hydrogen and interstitial carbon can control the growth of adlayers by engineering the activeness of h-BN edges. Activated edges diminish intercalation growth by decreasing the penetration probability of B/N atoms, while passivated edges promote intercalation growth by increasing the penetration probability of B/N atoms. Considering all these factors, we made an attempt to achieve precise control of the number of layers. First, uniform single-layer film can be obtained by eliminating intercalation growth. To achieve this, single

crystalline Ni substrate was chosen in order to diminish the formation of multilayer seeds. A mixture of 10-sccm N_2 plasma and 2-sccm ammonia was used as nitrogen source, in which the 2-sccm ammonia help alleviate plasma bombardment effect and sew the gaps between flakes. 4-min C_2H_2 carburization was used to compensate the effect from the presence of H and keep the h-BN edge active to B and N. The temperature of B_2O_3 effusion cell and substrate were kept at 1150 °C and 900 °C, respectively. The growth time was 6 h. Figure 5.10a shows an SEM image of single-layer film taken at the center of as grown sample, with the inset showing the film edge area. No large adlayers were observed over the 1 cm^2 surface. Corresponding RHEED images are shown in Figure 5.11, revealing the characteristic patterns of both the substrate and h-BN film. Figure 5.10b shows an optical microscopy image of the transferred h-BN film on SiO_2/Si substrate. The film was transferred by modified RCA process [71], followed by an annealing at 400 °C in oxygen environment for 3 h to remove water and PMMA residue [72, 73]. The transferred film shows uniform contrast in large area despite of some small contaminations (black and yellow dots), indicating high film quality. The thickness of the single-layer h-BN film was confirmed by TEM as shown in Figure 5.10c. Inserted SAED pattern shows bright spots in hexagonal arrangement, indicating the hexagonal arrangement of B and N atoms. The rings in SAED pattern are formed due to the diffraction of electrons by amorphous holy carbon thin film on TEM grids. The AFM image in Figure 5.10d was taken on transferred film shown in Figure 5.10b. Larger thickness (0.7 nm) compared to theoretical value (0.33 nm) of single-layer film may be caused by different atomic forces between tip/h-BN and tip/SiO_2, weak binding between h-BN film and SiO_2/Si substrate, as well as water and gases

intercalated in the interface [14]. Raman mapping was performed on the transferred sample, and the result is shown in Figure 5.10e. The green contrast is corresponding to E_{2g} peak of h-BN. The slight nonuniformity in Raman intensity may be caused by the corrugation of h-BN film formed during transfer process. Figure 5.10f shows Raman spectra extracted from nine different spots of Raman map, and all the peaks are located around 1369.5 cm^{-1}, which implies single-layer h-BN [74]. Figure 5.10 g/h show XPS spectra of B_1s and N_1s signals of as grown single layer h-BN film, respectively. As-measured XPS data was first deconvoluted, and fitted with Shirley background and GL(0) line shape. These spectra were then calibrated by shifting C-C main peak to 284.8 eV. The main peaks of B and N are measured to be 190.1 eV and 397.6 eV, respectively, an indication of sp^2 bonds, which is consistent with other reports [15, 16]. The smaller peak next to the main peak at higher position, 190.7 (398.2) eV, is assigned to cubic-like sp^3 bond [75, 76]. The neglectable small peak at the highest position, 191.6 (399.5) eV, is assigned to oxygen related defects

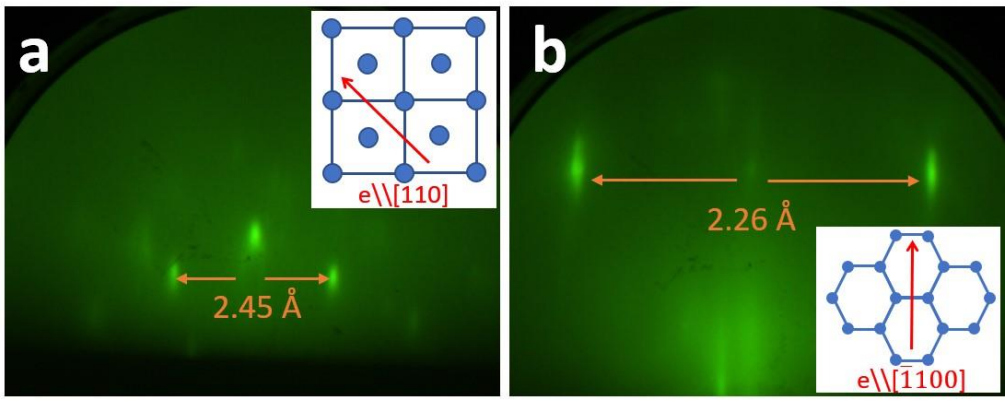

Figure 5.11 (a) RHEED pattern of the Ni substrate. (b) RHEED pattern of the Ni substrate with single layer h-BN grown on top. The inset show the incidence direction of the RHEED electron beam.

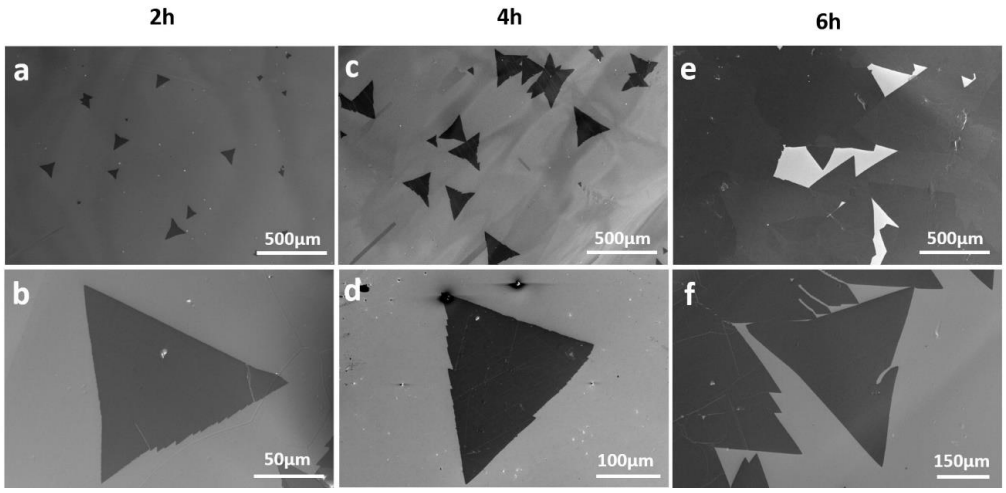

Figure 5.12 SEM images of single-layer h-BN on Ni at a growth time of (a/b) 2 h; (c/d) 4 h; and (e/f) 6 h. All samples were grown at 900 °C with "10+2" mixture and 4-min carburization. The B_2O_3 effusion cell temperature is 1150 °C.

77]. The boron to nitrogen ratio calculated based on XPS data is around 0.96. SEM images of growth time dependent single-layer films are shown in Figure 5.12. As the growth time increases, the coverage of the h-BN single-layer film increases.

The obstacle towards large-area bilayer and multilayer growth is the differentiated growth speeds between inner and outer layers, which is caused by insufficient source supply in the interface. In other words, the h-BN growth speed lies in a source limited region. On the other hand, if sufficient B and N atoms are supplied, h-BN growth may be transitioned into a self-limited region, where the growth speed is not limited by source supply, instead, it is limited by the bond formation rate. Then the growth speed of inner edge may have a chance to catch up outer edge so that large-area bilayer or multilayer films can be achieved. Toward this end, we grew a sample with an attempt of increasing B supply. Prior to introduction of both N and B sources, we deposited B only for 30 mins with B_2O_3 cell kept at 1175 °C. The pre-deposition of B allows the saturation of B in the substrate

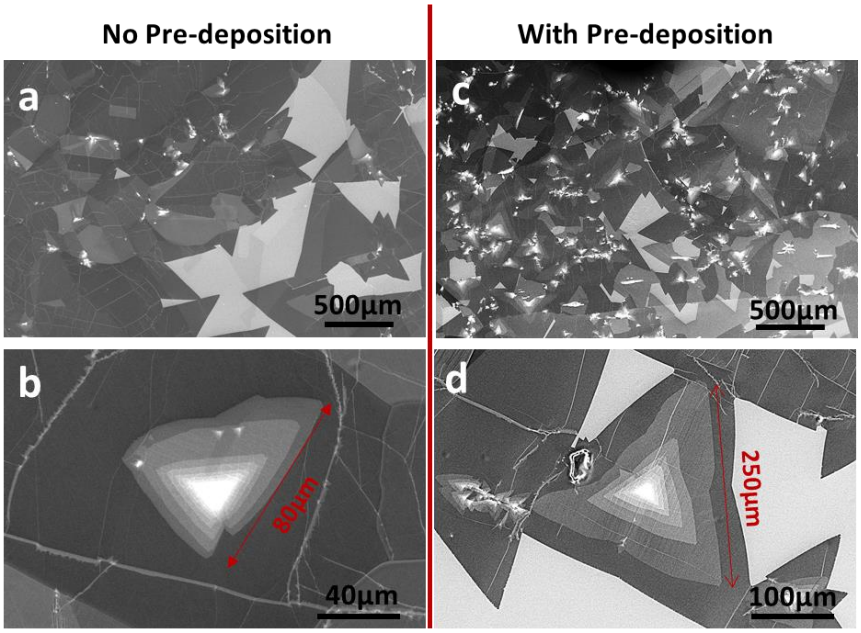

Figure 5.13 SEM characterization of pre-deposition dependent growth. (a) h-BN film grown without pre-deposition of boron; (b) close-up of one of the prism-adlayers on sample (a); (c) h-BN film grown with pre-deposition of boron; (d) close-up of one of the prism-adlayers on sample (d).

prior to growth; it also leads to the existence of abundant B atoms on the surface, in particular around surface defects or other imperfect or irregular sites. Once N atoms are introduced, the multilayer seed nucleation may have higher chances to happen. In other words, if the growth started without B pre-deposition, portion of B atoms would diffuse into the substrate at the early growth stage due to its solubility, then less B atoms would meet N atoms to nucleate and grow into multilayer seeds at the growth stage. The result of comparing h-BN growth with and without pre-deposition of B is shown in Figure 5.13. With pre-deposition, the adlayer size is significantly increased, and the second layer can reach up to 250µm. However, improved strategy to provide sufficient B and N sources to the interface between the outmost layer and the substrate is needed to achieve wafer-scale uniform multilayer growth, which is in progress.

5.4. **Conclusion**

We have carried out a study of intercalation growth of h-BN adlayers. By comparing the growth on different catalyst substrates, we showed that crystallographic defects on catalyst substrates play an important role in adlayer nucleation process. By using N plasma, ammonia, and their mixtures as nitrogen sources, we found that hydrogen played multiple roles in h-BN growth. On one hand, hydrogen terminating growing edges can provide protection against plasma's bombardment effect, making 2D h-BN flakes easier to merge. On the other hand, it passivates h-BN edges, which results in slower lateral growth rate and more intercalation growth of 3D adlayers. We also further revealed an important role played by interstitial carbon in the transition metal substrates, which enhances the substrate catalytic effect. The enhanced catalytic effect not only promotes the adsorption of B and N atoms, but also makes h-BN edges active in catching upcoming B and N atoms, which results in larger growth speed and less intercalation growth of adlayers. By controlling the mixture of atomic N and molecular N sources, we achieved large-area growth of adlayer-free single-layer h-BN film on a carburized single-crystalline Ni substrate. Our research work helps reveal the h-BN adlayer growth mechanism and provides insight towards controllable growth of wafer-scale h-BN 2D films with uniform thickness.

5.5. **References**

[1]Novoselov, K. S.; Geim, A. K.; Morozov, S. V.; Jiang, D.; Zhang, Y.; Dubonos, S. V.; Grigorieva, I. V.; Firsov, A. A., Electric field effect in atomically thin carbon films. Science 2004, 306, 666-669.

[2]Britnell, L.; Gorbachev, R.; Jalil, R.; Belle, B.; Schedin, F.; Mishchenko, A.; Georgiou, T.; Katsnelson, M.; Eaves, L.; Morozov, S., Field-effect tunneling transistor based on vertical graphene heterostructures. Science 2012, 335, 947-950.

[3]Bao, Q.; Loh, K. P., Graphene photonics, plasmonics, and broadband optoelectronic devices. ACS Nano 2012, 6, 3677-3694.

[4]Cheng, R.; Li, D.; Zhou, H.; Wang, C.; Yin, A.; Jiang, S.; Liu, Y.; Chen, Y.; Huang, Y.; Duan, X., Electroluminescence and photocurrent generation from atomically sharp WSe2/MoS2 heterojunction p–n diodes. Nano Lett. 2014, 14, 5590-5597.

[5]Withers, F.; Del Pozo-Zamudio, O.; Mishchenko, A.; Rooney, A.; Gholinia, A.; Watanabe, K.; Taniguchi, T.; Haigh, S.; Geim, A.; Tartakovskii, A., Light-emitting diodes by band-structure engineering in van der Waals heterostructures. Nat. Mater. 2015, 14, 301.

[6]Maity, A.; Doan, T.; Li, J.; Lin, J.; Jiang, H., Realization of highly efficient hexagonal boron nitride neutron detectors. Appl. Phys. Lett. 2016, 109, 072101.

[7]Hui, F.; Villena, M. A.; Fang, W.; Lu, A.-Y.; Kong, J.; Shi, Y.; Jing, X.; Zhu, K.; Lanza, M., Synthesis of large-area multilayer hexagonal boron nitride sheets on iron substrates and its use in resistive switching devices. 2D Mater. 2018, 5, 031011.

[8]Caneva, S.; Weatherup, R. S.; Bayer, B. C.; Brennan, B.; Spencer, S. J.; Mingard, K.; Cabrero-Vilatela, A.; Baehtz, C.; Pollard, A. J.; Hofmann, S., Nucleation control for large, single crystalline domains of monolayer hexagonal boron nitride via Si-doped Fe catalysts. Nano Lett. 2015, 15, 1867-1875.

[9]Kim, G.; Jang, A.-R.; Jeong, H. Y.; Lee, Z.; Kang, D. J.; Shin, H. S., Growth of high-crystalline, single-layer hexagonal boron nitride on recyclable platinum foil. Nano Lett. 2013, 13, 1834-1839.

[10]Kim, K. K.; Hsu, A.; Jia, X.; Kim, S. M.; Shi, Y.; Hofmann, M.; Nezich, D.; Rodriguez-Nieva, J. F.; Dresselhaus, M.; Palacios, T., Synthesis of monolayer hexagonal boron nitride on Cu foil using chemical vapor deposition. Nano letters 2011, 12, 161-166.

[11]Meng, J.; Zhang, X.; Wang, Y.; Yin, Z.; Liu, H.; Xia, J.; Wang, H.; You, J.; Jin, P.; Wang, D., Aligned Growth of Millimeter-Size Hexagonal Boron Nitride Single-Crystal Domains on Epitaxial Nickel Thin Film. Small 2017, 13, 1604179.

[12]Ying, H.; Li, X.; Li, D.; Huang, M.; Wan, W.; Yao, Q.; Chen, X.; Wang, Z.; Wu, Y.; Wang, L., Ni foam assisted synthesis of high quality hexagonal boron nitride with large domain size and controllable thickness. 2D Mater. 2018, 5, 025020.

[13]Petrović, M.; Hagemann, U.; Horn-von Hoegen, M.; zu Heringdorf, F.-J. M., Microanalysis of single-layer hexagonal boron nitride islands on Ir (111). Appl. Surf. Sci. 2017, 420, 504-510.

[14]Khan, M. H.; Huang, Z.; Xiao, F.; Casillas, G.; Chen, Z.; Molino, P. J.; Liu, H. K., Synthesis of large and few atomic layers of hexagonal boron nitride on melted copper. Sci. Rep. 2015, 5, 7743.

[15]Kidambi, P. R.; Blume, R.; Kling, J.; Wagner, J. B.; Baehtz, C.; Weatherup, R. S.; Schloegl, R.; Bayer, B. C.; Hofmann, S., In situ observations during chemical vapor deposition of hexagonal boron nitride on polycrystalline copper. Chemistry of Materials 2014, 26, 6380-6392.

[16]Caneva, S.; Weatherup, R. S.; Bayer, B. C.; Blume, R.; Cabrero-Vilatela, A.; Braeuninger-Weimer, P.; Martin, M.-B.; Wang, R.; Baehtz, C.; Schloegl, R., Controlling catalyst bulk reservoir effects for monolayer hexagonal boron nitride CVD. Nano Lett. 2016, 16, 1250-1261.

[17]Robertson, A. W.; Warner, J. H., Hexagonal single crystal domains of few-layer graphene on copper foils. Nano Lett. 2011, 11, 1182-1189.

[18]Li, Q.; Chou, H.; Zhong, J.-H.; Liu, J.-Y.; Dolocan, A.; Zhang, J.; Zhou, Y.; Ruoff, R. S.; Chen, S.; Cai, W., Growth of adlayer graphene on Cu studied by carbon isotope labeling. Nano Lett. 2013, 13, 486-490.

[19]Yang, Y.; Fu, Q.; Li, H.; Wei, M.; Xiao, J.; Wei, W.; Bao, X., Creating a Nanospace under an h-BN Cover for Adlayer Growth on Nickel (111). ACS Nano 2015, 9, 11589-11598.

[20]Summerfield, A.; Davies, A.; Cheng, T. S.; Korolkov, V. V.; Cho, Y.; Mellor, C. J.; Foxon, C. T.; Khlobystov, A. N.; Watanabe, K.; Taniguchi, T., Strain-engineered graphene grown on hexagonal boron nitride by molecular beam epitaxy. Sci. Rep. 2016, 6, 22440.

[21]Ferguson, J.; Weimer, A.; George, S., Atomic layer deposition of boron nitride using sequential exposures of BCl3 and NH3. Thin Solid Films 2002, 413, 16-25.

[22]Driver, M. S.; Beatty, J. D.; Olanipekun, O.; Reid, K.; Rath, A.; Voyles, P. M.; Kelber, J. A., Atomic layer epitaxy of h-BN (0001) multilayers on Co (0001) and molecular beam epitaxy growth of graphene on h-BN (0001)/Co (0001). Langmuir 2016, 32, 2601-2607.

[23]Jones, J.; Beauclair, B.; Olanipekun, O.; Lightbourne, S.; Zhang, M.; Pollok, B.; Pilli, A.; Kelber, J., Atomic layer deposition of h-BN (0001) on RuO2 (110)/Ru (0001). Journal of Vacuum Science & Technology A: Vacuum, Surfaces, and Films 2017, 35, 01B139.

[24]Shi, Y.; Hamsen, C.; Jia, X.; Kim, K. K.; Reina, A.; Hofmann, M.; Hsu, A. L.; Zhang, K.; Li, H.; Juang, Z.-Y., Synthesis of few-layer hexagonal boron nitride thin film by chemical vapor deposition. Nano Lett. 2010, 10, 4134-4139.

[25]Song, L.; Ci, L.; Lu, H.; Sorokin, P. B.; Jin, C.; Ni, J.; Kvashnin, A. G.; Kvashnin, D. G.; Lou, J.; Yakobson, B. I., Large scale growth and characterization of atomic hexagonal boron nitride layers. Nano Lett. 2010, 10, 3209-3215.

[26]Ismach, A.; Mende, P.; Dolocan, A.; Addou, R.; Aloni, S.; Wallace, R.; Feenstra, R.; Ruoff, R.; Colombo, L., Carbon-Assisted Chemical Vapor Deposition of Hexagonal Boron Nitride. 2D Mater. 2017.

[27]Petrović, M.; Horn-von Hoegen, M.; zu Heringdorf, F.-J. M., Lateral heterostructures of hexagonal boron nitride and graphene: BCN alloy formation and microstructuring mechanism. Appl. Surf. Sci. 2018, 455, 1086-1094.

[28]Song, Y.; Zhang, C.; Li, B.; Jiang, D.; Ding, G.; Wang, H.; Xie, X., Triggering the atomic layers control of hexagonal boron nitride films. Appl. Surf. Sci. 2014, 313, 647-653.

[29]Nakhaie, S.; Wofford, J.; Schumann, T.; Jahn, U.; Ramsteiner, M.; Hanke, M.; Lopes, J.; Riechert, H., Synthesis of atomically thin hexagonal boron nitride films on nickel foils by molecular beam epitaxy. Appl. Phys. Lett. 2015, 106, 213108.

[30]Tsai, C.; Kobayashi, Y.; Akasaka, T.; Kasu, M., Molecular beam epitaxial growth of hexagonal boron nitride on Ni (1 1 1) substrate. Journal of Crystal Growth 2009, 311, 3054-3057.

[31]Zuo, Z.; Xu, Z.; Zheng, R.; Khanaki, A.; Zheng, J.-G.; Liu, J., In-situ epitaxial growth of graphene/h-BN van der Waals heterostructures by molecular beam epitaxy. Sci. Rep. 2015, 5, 14760.

[32]Vuong, T.; Cassabois, G.; Valvin, P.; Rousseau, E.; Summerfield, A.; Mellor, C.; Cho, Y.; Cheng, T.; Albar, J. D.; Eaves, L., Deep ultraviolet emission in hexagonal boron nitride grown by high-temperature molecular beam epitaxy. 2D Mater. 2017, 4, 021023.

[33]Heilmann, M.; Bashouti, M.; Riechert, H.; Lopes, J., Defect mediated van der Waals epitaxy of hexagonal boron nitride on graphene. 2D Mater. 2018, 5, 025004.

[34]Khanaki, A.; Tian, H.; Xu, Z.; Zheng, R.; He, Y.; Cui, Z.; Yang, J.; Liu, J., Effect of high carbon incorporation in Co substrates on the epitaxy of hexagonal boron nitride/graphene heterostructures. Nanotechnology 2017, 29, 035602.

[35]Summerfield, A.; Kozikov, A.; Cheng, T. S.; Davies, A.; Cho, Y.-J.; Khlobystov, A. N.; Mellor, C. J.; Foxon, C. T.; Watanabe, K.; Taniguchi, T., Moiré-modulated conductance of hexagonal boron nitride tunnel barriers. Nano Lett. 2018, 18, 4241-4246.

[36]Cho, Y.-J.; Summerfield, A.; Davies, A.; Cheng, T. S.; Smith, E. F.; Mellor, C. J.; Khlobystov, A. N.; Foxon, C. T.; Eaves, L.; Beton, P. H., Hexagonal boron nitride tunnel

barriers grown on graphite by high temperature molecular beam epitaxy. Sci. Rep. 2016, 6, 34474.

[37]Tian, H.; Khanaki, A.; Das, P.; Zheng, R.; Cui, Z.; He, Y.; Shi, W.; Xu, Z.; Lake, R.; Liu, J., Role of Carbon Interstitials in Transition Metal Substrates on Controllable Synthesis of High-Quality Large-Area Two-Dimensional Hexagonal Boron Nitride Layers. Nano Lett. 2018, 18, 3352-3361.

[38]Sutter, P.; Sutter, E., Thickness determination of few-layer hexagonal boron nitride films by scanning electron microscopy and Auger electron spectroscopy. APL Materials 2014, 2, 092502.

[39]Tai, L.; Zhu, D.; Liu, X.; Yang, T.; Wang, L.; Wang, R.; Jiang, S.; Chen, Z.; Xu, Z.; Li, X., Direct Growth of Graphene on Silicon by Metal-Free Chemical Vapor Deposition. Nano-Micro Letters 2018, 10, 20.

[40]Chugh, D.; Wong-Leung, J.; Li, L.; Lysevych, M.; Tan, H.; Jagadish, C., Flow modulation epitaxy of hexagonal boron nitride. 2D Mater. 2018, 5, 045018.

[41]Entani, S.; Takizawa, M.; Li, S.; Naramoto, H.; Sakai, S., Growth of graphene on SiO2 with hexagonal boron nitride buffer layer. Appl. Surf. Sci. 2019, 475, 6-11.

[42]Wang, Z.; Xue, Z.; Zhang, M.; Wang, Y.; Xie, X.; Chu, P. K.; Zhou, P.; Di, Z.; Wang, X., Germanium-Assisted Direct Growth of Graphene on Arbitrary Dielectric Substrates for Heating Devices. small 2017, 13.

[43]Chen, X.; Wu, B.; Liu, Y., Direct preparation of high quality graphene on dielectric substrates. Chem. Soc. Rev. 2016, 45, 2057-2074.

[44]Sutter, P. W.; Flege, J.-I.; Sutter, E. A., Epitaxial graphene on ruthenium. Nat. Mater. 2008, 7, 406.

[45]Reina, A.; Jia, X.; Ho, J.; Nezich, D.; Son, H.; Bulovic, V.; Dresselhaus, M. S.; Kong, J., Large area, few-layer graphene films on arbitrary substrates by chemical vapor deposition. Nano Lett. 2008, 9, 30-35.

[46]Reina, A.; Thiele, S.; Jia, X.; Bhaviripudi, S.; Dresselhaus, M. S.; Schaefer, J. A.; Kong, J., Growth of large-area single-and bi-layer graphene by controlled carbon precipitation on polycrystalline Ni surfaces. Nano Research 2009, 2, 509-516.

[47]Lahiri, J.; Miller, T. S.; Ross, A. J.; Adamska, L.; Oleynik, I. I.; Batzill, M., Graphene growth and stability at nickel surfaces. New Journal of Physics 2011, 13, 025001.

[48]Zou, Z.; Fu, L.; Song, X.; Zhang, Y.; Liu, Z., Carbide-forming groups IVB-VIB metals: a new territory in the periodic table for CVD growth of graphene. Nano Lett. 2014, 14, 3832-3839.

[49]Fang, W.; Hsu, A. L.; Song, Y.; Kong, J., A review of large-area bilayer graphene synthesis by chemical vapor deposition. Nanoscale 2015, 7, 20335-20351.

[50]Zhang, X. Y.; Wang, L.; Xin, J.; Yakobson, B. I.; Ding, F., Role of Hydrogen in Graphene Chemical Vapor Deposition Growth on a Copper Surface. J. Am. Chem. Soc. 2014, 136, 3040-3047.

[51]Li, Y.; Wu, B.; Guo, W.; Wang, L.; Li, J.; Liu, Y., Tailoring graphene layer-to-layer growth. Nanotechnology 2017, 28, 265101.

[52]Yang, P.; Prater, J.; Liu, W.; Glass, J.; Davis, R., The formation of epitaxial hexagonal boron nitride on nickel substrates. J. Electron. Mater. 2005, 34, 1558-1564.

[53]Massalski, T. B., Binally Alloy Phase Diagrams. American society for metals 1986.

[54]Abdulrahman, R.; Hendry, A., Solubility of nitrogen in liquid nickel-based alloys. Metallurgical and Materials Transactions B 2001, 32, 1103-1112.

[55]KOJIMA, Y.; YAMADA, Y.; INOUYE, M., The Solubilities and Diffusion Coefficients of Nitrogen in the Liquid Iron-Nickel and Iron-Cobalt Alloys at 1600° C. Tetsu-to-Hagane 1975, 61, 195-201.

[56]Loginova, E.; Bartelt, N. C.; Feibelman, P. J.; McCarty, K. F., Evidence for graphene growth by C cluster attachment. New Journal of Physics 2008, 10, 093026.

[57]Ganley, J. C.; Thomas, F.; Seebauer, E.; Masel, R. I., A priori catalytic activity correlations: the difficult case of hydrogen production from ammonia. Catal. Lett. 2004, 96, 117-122.

[58]Xie, Z.; Ni, S.; Song, M., Effect of Y2O3 doping on FCC to HCP phase transformation in cobalt produced by ball milling and spark plasma sintering. Powder Technol. 2018, 324, 1-4.

[59]Rasim, K.; Bobeth, M.; Pompe, W.; Seriani, N., A microkinetic model of ammonia decomposition on a Pt overlayer on Au (1 1 1). J. Mol. Catal. A: Chem. 2010, 325, 15-24.

[60]Wu, B.; Geng, D.; Xu, Z.; Guo, Y.; Huang, L.; Xue, Y.; Chen, J.; Yu, G.; Liu, Y., Self-organized graphene crystal patterns. NPG Asia Materials 2012, 4, e36.

[61]Fan, Z.; Newman, N., Kinetic energy distribution of nitrogen ions in an electron cyclotron resonance plasma. Journal of Vacuum Science & Technology A: Vacuum, Surfaces, and Films 1998, 16, 2132-2139.

[62]Fu, T.; Newman, N.; Jones, E.; Chan, J.; Liu, X.; Rubin, M.; Cheung, N.; Weber, E., The influence of nitrogen ion energy on the quality of GaN films grown with molecular beam epitaxy. J. Electron. Mater. 1995, 24, 249-255.

[63]Hao, Y.; Bharathi, M.; Wang, L.; Liu, Y.; Chen, H.; Nie, S.; Wang, X.; Chou, H.; Tan, C.; Fallahazad, B., The role of surface oxygen in the growth of large single-crystal graphene on copper. Science 2013, 1243879.

[64]Stehle, Y. Y.; Sang, X.; Unocic, R. R.; Voylov, D.; Jackson, R. K.; Smirnov, S.; Vlassiouk, I., Anisotropic Etching of Hexagonal Boron Nitride and Graphene: Question of Edge Terminations. Nano Lett. 2017, 17, 7306-7314.

[65]McDougall, N. L.; Partridge, J. G.; Nicholls, R. J.; Russo, S. P.; McCulloch, D. G., Influence of point defects on the near edge structure of hexagonal boron nitride. Phys. Rev. B 2017, 96, 144106.

[66]Saito, Y., Statistical physics of crystal growth. World Scientific: 1996.

[67]Zhang, Z.; Lagally, M. G., Atomistic processes in the early stages of thin-film growth. Science 1997, 276, 377-383.

[68]Weatherup, R. S.; Bayer, B. C.; Blume, R.; Ducati, C.; Baehtz, C.; Schlogl, R.; Hofmann, S., In situ characterization of alloy catalysts for low-temperature graphene growth. Nano Lett. 2011, 11, 4154-4160.

[69]Bayer, B. C.; Bosworth, D. A.; Michaelis, F. B.; Blume, R.; Habler, G.; Abart, R.; Weatherup, R. S.; Kidambi, P. R.; Baumberg, J. J.; Knop-Gericke, A., In situ observations of phase transitions in metastable nickel (carbide)/carbon nanocomposites. The Journal of Physical Chemistry C 2016, 120, 22571-22584.

[70]Xu, J.; Saeys, M., First principles study of the stability and the formation kinetics of subsurface and bulk carbon on a Ni catalyst. The Journal of Physical Chemistry C 2008, 112, 9679-9685.

[71]Liang, X.; Sperling, B. A.; Calizo, I.; Cheng, G.; Hacker, C. A.; Zhang, Q.; Obeng, Y.; Yan, K.; Peng, H.; Li, Q., Toward clean and crackless transfer of graphene. ACS Nano 2011, 5, 9144-9153.

[72]Li, L. H.; Cervenka, J.; Watanabe, K.; Taniguchi, T.; Chen, Y., Strong oxidation resistance of atomically thin boron nitride nanosheets. ACS Nano 2014, 8, 1457-1462.

[73]Gong, C.; Floresca, H. C.; Hinojos, D.; McDonnell, S.; Qin, X.; Hao, Y.; Jandhyala, S.; Mordi, G.; Kim, J.; Colombo, L., Rapid selective etching of PMMA residues from transferred graphene by carbon dioxide. The Journal of Physical Chemistry C 2013, 117, 23000-23008.

[74]Arenal, R.; Ferrari, A.; Reich, S.; Wirtz, L.; Mevellec, J.-Y.; Lefrant, S.; Rubio, A.; Loiseau, A., Raman spectroscopy of single-wall boron nitride nanotubes. Nano Lett. 2006, 6, 1812-1816.

[75]Deng, J.; Chen, G.; Song, X., Characterization of cubic boron nitride thin films deposited by RF sputter. Int. J. Mod Phys B 2002, 16, 4339-4342.

[76]Mirkarimi, P.; McCarty, K.; Medlin, D., Review of advances in cubic boron nitride film synthesis. Materials Science and Engineering: R: Reports 1997, 21, 47-100.

[77]Sediri, H.; Pierucci, D.; Hajlaoui, M.; Henck, H.; Patriarche, G.; Dappe, Y. J.; Yuan, S.; Toury, B.; Belkhou, R.; Silly, M. G., Atomically Sharp Interface in an h-BN-epitaxial graphene van der Waals Heterostructure. Sci. Rep. 2015, 5, 16465.

Chapter 6 Summary

In summary, we discussed the carbon interstitial assisted growth of hexagonal boron nitride by molecular beam epitaxy. Firstly, we studied the synthesis of h-BN/G heterostructure with high carbon introduction in Chapter 2. We rationalized the growth in four different regions based on the amount of carbon in Co substrate and graphene growth mode/morphology. In region (1), the graphene network is formed under the h-BN layers only by precipitation during cooling down process. In region (2), isothermal graphene growth occurs to form graphene island partially covering the substrate, followed by further precipitation graphene growth. As a result, non-uniform h-BN/G heterostructure is formed. In regions (3), a uniform h-BN/G heterostructure with a thin continuous h-BN and a thick continuous multilayer graphene are formed from both isothermal graphene growth and precipitation. We found that the top h-BN film significantly influences the morphology, thickness and quality of the underneath G layer for region 1 growth.

In Chapter 3, we showed that interstitial carbon atoms in Co trigger and enhance the growth of h-BN at the given condition. Further increase of the carbon concentration

promotes lateral growth of h-BN few-layers and eliminates the prism-shape island formation. The lateral h-BN growth is fitted with JMAK model. Characterizations were carried out on a few-layer h-BN sample grown on a 240-s C_2H_2 treated Co substrate, revealing that a tri-layer h-BN film with good uniformity in thickness and a breakdown electric field of 9 MV/cm is formed. single-crystalline h-BN flakes of ~600 μm, and large-area uniform h-BN monolayer were achieved on carburized Ni substrates. The growth mechanism is further studied by DFT calculations. The adsorption and diffusion of both B and N atoms are enhanced by the existence of interstitial carbon atoms in the substrate, resulting in a reliable and controllable growth of 2D h-BN in contrast to no growth on pristine Co.

In Chapter 4, we further demonstrated controllable synthesis of millimeter-size single-crystal h-BN domains through an interstitial carbon assisted approach. Interstitial C atoms in Ni (100) substrates promote B and N adsorption and push the growth into fast diffusion regions, which essentially reduces nucleation activation energy. With proper preparation of high-quality substrates, which yields large Ni (100) grains, Single-crystal h-BN monolayer domains over 1 mm were routinely obtained and a large single-crystal h-BN domain of 1.4 mm was achieved. Continuous large-area single-layer h-BN film with a high breakdown electric field of 9.75 MV/cm was also demonstrated. The growth dynamics were studied by tuning different growth parameters including substrate temperature, and B and N source fluxes. The epitaxial relationship between h-BN and substrate was studied with the assistance of EBSD mapping. The in-depth experimental analysis combined with

the support of DFT simulations paves the way towards full understanding of the growth mechanism of 2D h-BN on transition metal substrates.

In Chapter 5, we have carried out a study of intercalation growth of h-BN adlayers. By comparing the growth on different catalyst substrates, we showed that crystallographic defects on catalyst substrates play an important role in adlayer nucleation process. By using N plasma, ammonia, and their mixtures as nitrogen sources, we found that hydrogen played multiple roles in h-BN growth. On one hand, hydrogen terminating growing edges can provide protection against plasma's bombardment effect, making 2D h-BN flakes easier to merge. On the other hand, it passivates h-BN edges, which results in slower lateral growth rate and more intercalation growth of 3D adlayers. We also further revealed an important role played by interstitial carbon in the transition metal substrates, which enhances the substrate catalytic effect. The enhanced catalytic effect not only promotes the adsorption of B and N atoms, but also makes h-BN edges active in catching upcoming B and N atoms, which results in larger growth speed and less intercalation growth of adlayers. By controlling the mixture of atomic N and molecular N sources, we achieved large-area growth of adlayer-free single-layer h-BN film on a carburized single-crystalline Ni substrate.

The concept proposed and demonstrated here, namely interstitial-assisted growth of h-BN 2D films not only paves the way of reliable synthesis of high-quality, large-area, uniform 2D h-BN for various applications but also can be applied to advance the synthesis of other 2D crystal materials.